REPORT DOCUMENTATION PAGE

AFRL-SR-BL-TR-01-

0226

1. AGENCY USE ONLY *(Leave blank)*	2. REPORT DATE	3. RE
	MARCH 2001	FIN. ... REPORT 1 AUG 97 - 30 JUN 00

4. TITLE AND SUBTITLE
TURBINE ENGINE CONTROL USING MEMS FOR REDUCTION OF HIGH CYCLE FATIGUE

5. FUNDING NUMBERS
F49620-97-1-0521

F118/19
63739E

6. AUTHOR(S)
JINWEI FENG, RICARD BURDISSO, WING NG, AND TED RAPPAPORT

7. PERFORMING ORGANIZATION NAME(S) AND ADDRESS(ES)
VIRGINIA TECH
DEPT OF MECHANICAL ENGINEEIRNG
DEPT OF ELECTRICAL ENGINEERING
BLACKSBURG, VA 24061-0238

8. PERFORMING ORGANIZATION REPORT NUMBER

9. SPONSORING/MONITORING AGENCY NAME(S) AND ADDRESS(ES)
AIR FORCE OFFICE OF SCIENTIFIC RESEARCH
801 N. RANDOLPH STREET, ROOM 732
ARLINGTON, VA 22203-1977

10. SPONSORING/MONITORING AGENCY REPORT NUMBER

11. SUPPLEMENTARY NOTES

12a. DISTRIBUTION AVAILABILITY STATEMENT
APPROVED FOR PUBLIC RELEASE, DISTRIBUTION IS UNLIMITED

13. ABSTRACT *(Maximum 200 words)*
The research effort presented in this dissertation consists of employing active trailing edge blowing control to reduce the unsteady stator-rotor interaction in a turbofan simulator. Two active flow control systems with different wake sensing approaches are successfully implemented on the engine simulator. The first flow control system utilizes Pitot probes as flow sensors. Use of Pitot probes as sensors is appropriate as a first step toward a more in depth investigation of active trailing edge blowing control. An upper performance limit in terms of wake-filing can be obtained and serves as the baseline in evaluating other control systems with indirect wake sensors. The ability of the system to achieve effective wake filing when subjected to a change in inlet flow conditions demonstrates the feasibility and advantage of active flow control. Significant tonal noise reductions in the far field are also obtained. The second control system involves using microphones as indirect wake sensors. The significance of these acoustic sensing approaches is to provide a practical TEB approach for realistic engines implementations. Microphones are flush mounted on the inlet case to sense the tonal noise at the blade passing frequency. The first sensing approach only uses the tone magnitude while the second novel sensing approach utilizes both the tone magnitude and phase as error information. The convergence rate of the second sensing approach is comparable with that of the Pitot-prove based experiments. The acoustic results obtained from both sensing approaches agree well with those obtained using Pitot probes as sensors.

14. SUBJECT TERMS

15. NUMBER OF PAGES
215

16. PRICE CODE

17. SECURITY CLASSIFICATION OF REPORT	18. SECURITY CLASSIFICATION OF THIS PAGE	19. SECURITY CLASSIFICATION OF ABSTRACT	20. LIMITATION OF ABSTRACT
U	U	U	

Final Report

for

AFOSR grant F49620-97-1-0521

Turbine Engine Control Using MEMS for
Reduction of High-Cycle-Fatigue

Prepared by

Jinwei Feng
Ricardo Burdisso
Wing Ng
Department of Mechanical Engineering
Virginia Tech

Ted Rappaport
Department of Electrical Engineering
Virginia Tech
Blacksburg, VA 24061-0238

20010404 105

March 2001

Turbine Engine Control Using MEMS for

Reduction of High-Cycle-Fatigue

(ABSTRACT)

The research effort presented in this dissertation consists of employing active trailing edge blowing control to reduce the unsteady stator-rotor interaction in a turbofan simulator. Two active flow control systems with different wake sensing approaches are successfully implemented on the engine simulator.

The first flow control system utilizes Pitot probes as flow sensors. Use of Pitot probes as sensors is appropriate as a first step toward a more in depth investigation of active trailing edge blowing control. An upper performance limit in terms of wake-filling can be obtained and serves as the baseline in evaluating other control systems with indirect wake sensors. The ability of the system to achieve effective wake filling when subjected to a change in inlet flow conditions demonstrates the feasibility and advantage of active flow control. Significant tonal noise reductions in the far field are also obtained.

The second control system involves using microphones as indirect wake sensors. The significance of these acoustic sensing approaches is to provide a practical TEB approach for realistic engines implementations. Microphones are flush mounted on the inlet case to sense the tonal noise at the blade passing frequency. The first sensing approach only uses the tone magnitude while the second novel sensing approach utilizes both the tone magnitude and phase as error information. The convergence rate of the second sensing approach is comparable with that of the Pitot-prove based experiments. The acoustic results obtained from both sensing approaches agree well with those obtained using Pitot probes as sensors.

In addition to the experimental part of this research, analytical studies are also conducted on the trailing edge blowing modeling using an aeroacoustic code. An analytical model for trailing edge blowing is first proposed. This model is then introduced into the two-dimensional aeroacoustic code to investigate effect of various trailing edge blowing managements in the tonal sound generation.

Contents

List of Figures

List of Tables

Nomenclature

A_{mu}	Mode amplitude of mode (m, μ)
a	Radius of inlet duct
a_0	Scaling facotr for TEB jet width
ADC	Analog to Digital Converter
b	Radius of hub or RMS value of BPF tone
b_0	Scaling factor for TEB jet depth
BPF	Blade Passing Frequency
c	Sound speed in the air
C_D	Drag coefficient
C_I	IGV chord
D	Direction signal
DAC	Digital to Analog Converter
DC	Direct Current
DSP	Digital Signal Processing
e	Error signal
EGV	Exit Guide Vane
f_{BPF}	Frequency of BPF tone
$f_{m\mu}^{cut-on}$	The cut-on frequency of mode (m, μ)
F_n	FFT coefficient of nth harmonics of wake profile

FFT	Fast Fourier Transform
HCF	High Cycle Fatigue
ICD	Inlet Control Device
IGV	Inlet Guide Vane
k	Integer index
k_0	Free-space wavenumber
k_{mu}	Circumferential wavenumber associated with (m, μ) mode
$k_{z,mu}$	Axial wavenumber associated with (m, μ) mode
LR	Rotor loading
LS	Stator loading
LCF	Low Cycle Fatigue
LMS	Least Mean Square
LPF	Low Pass Filter
m	Circumferential order of acoustic mode in cylindrical coordinate
$\dot{m}_d$	Normalized mass flow rate deficit
M	Mach number of flow velocity
M_d	Normalized momentum flux deficit
MEMS	Mechanical-Electro-Machine System
N_B	Number of rotor blades
N_c	Number of a circular array of microphones
p	Sound pressure or Phase signal of BPF tone
P	Static pressure
P_0	Total pressure
PID	Proportional Integral Derivative
PLL	Phase Locked Loop
PVC	Phase to Voltage Converter

r	Radial direction in cylindrical coordinate
$r(n)$	n^{th} microphone output signal
RMS	Root Mean Square
RPM	Revolution Per Minute
s	Streamwise distance from the IGV trailing edge
S	Step size or number of IGV or sampling period
SCF	Switch Capacitor Filter
SISO	Single Input Single Output
SPL	Sound Pressure Level
TEB	Trailing Edge Blowing
TTL	Transistor to Transistor Logic
TPS	Turbofan Propulsion Simulator
U	Control signal
V	Flow velocity
VCO	Voltage Controlled Oscillator
W_0	Free stream velocity
W_{dc}	Depth of wake deficit
WR	Wash velocity on rotor
WS	Wash velocity on stator
XOR	Exclusive OR
z	Axial direction of cylindrical coordinate
μ	Radial order of acoustic mode in cylindrical coordinate
$\bar{\mu}$	Mean value
τ	Standard deviation
θ	Circumferential direction in cylindrical coordinate

ρ	Density of the air
δ	Parameter to characterize wake width
Ω	Rotating speed
Ψ_p	Angle of principal lobe
Φ	Mode shape function
ϕ	Initial phase of stationary acoustic mode
$\Delta\phi$	Phase delay
Θ	Circumferential function of mode shape
$\dot{\phi}$	Initial phase
$J_m(\cdot)$	First kind Bessel function of mth order
$J'_m(\cdot)$	Derivative of $J_m(\cdot)$
$Y_m(\cdot)$	Second kind Bessel function of mth order
$Y'_m(\cdot)$	Derivative of $Y_m(\cdot)$

Chapter 1

Introduction

This chapter presents the background information of the research performed in this dissertation. First, high cycle fatigue (HCF) problem in gas turbine engines is addressed in section 1.1. It consists of the description of the HCF impact on aircraft engines, the HCF causes, and the current HCF reduction methods. Trailing edge blowing (TEB), known as a wake management technique to reduce HCF, is discussed at great length. It is followed by the motivations and objectives of this research. Finally, the organization of this dissertation is outlined.

1.1   High Cycle Fatigue

Fatigue is a type of failure that results in cracking or fracture when metal components are subjected to repeated or fluctuating loads. A fatigue failure starts when a crack forms at an initiation site. The crack leads to a localized stress concentration, which, if high enough, will cause the crack to propagate with each load cycle. As the crack propagates, the stress in the component will continue to rise until the remaining material fails abruptly. High cycle fatigue refers to fatigue failures which occur after the first 1000 load cycles, while low cycle fatigue failures (LCF) are regarded as those which occur within that number of cycles.

High cycle fatigue is the main cause of failure in aircraft engines, especially military engines. After thousands of hours of flying, the engine blades may disintegrate due to HCF which may cause an aircraft loss with absolutely no warning. In the past decades, high cycle fatigue has accounted for 55% of the US Air Force's engine-related mishaps and 30% of the total maintenance bill. About 66% of US Air Force's maintenance actions are spent to ensure HCF does not impact mission readiness. The U.S. Air Force estimates an expenditure of about $100 million each year to inspect and fix HCF related problems [1]. In addition, HCF is also a primary concern for future engines.

Figure 1.1 shows a typical turbofan engine. The compressor of turbofan engines is usually composed of multiple stator-rotor stages. The rotor blades, especially for the first stage fan blades, are the components which are most vulnerable to the HCF failure. As will be discussed later in detail in this chapter, one of the causes of HCF failure in the first stage rotor blades is from the upstream stator wakes, i.e., inlet guide vane (IGV) wakes. Inlet guide vane wake is a flow velocity loss whose typical velocity profile is shown in Figure 1.2. To reduce the HCF failure in the rotor blades by filling the wake through injection of air from the trailing edge of the IGV is the primary purpose of this research.

1.1.1 Causes of high cycle fatigue failure

In gas turbine engines, the LCF failures occurring on the rotor blades are usually caused by large cyclic excursions between zero stress and operating stress. For example, a rotor disk would experience one LCF cycle as it accelerates from rest to operating speed, then decelerates to shutdown. On the other hand, HCF failures generally occur due to numerous, smaller cyclic excursions between two or more stress states. These excursions could result from vibrations, thermal cycling, or other fluctuating loads [2].
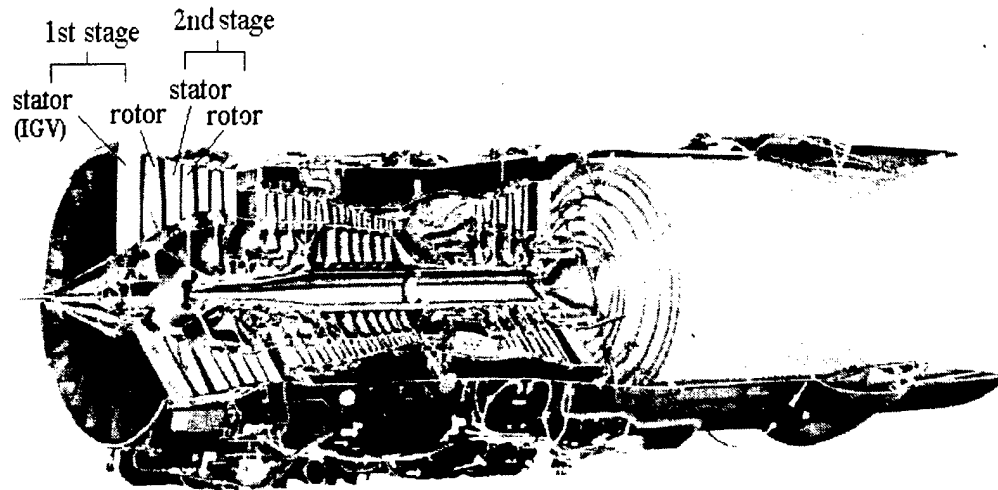
Figure 1.1: High cycle fatigue failure on the rotor blades of aircraft engines.
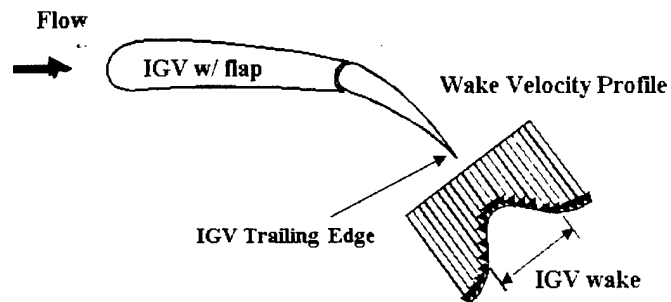
Figure 1.2: IGV wake velocity profile.

Rotor blades are subject to all of these types of loads and particularly vulnerable to HCF failures.

There are two types of rotor blade vibrations which cause HCF failure: flutter and forced vibrations. The former is a self-excited oscillation or instability at or close to the natural frequency of the mechanical system which does not require any external disturbance to excite it [3, 4]. Since flutter is an aeroelastic instability, it cannot be stopped in most cases once it is initiated. Flutter measurements made about a quarter century ago showed vibration amplitudes of about 1/8 inch (0.32 cm) for a blade thickness of 0.15 inch (0.38 cm). This is precisely the reason why it receives significant attention from industry. Forced vibrations primarily arise from the movement of the rotor through flow defects or flow nonuniformities [3, 5, 6]. The three primary types of flow nonuniformities or flow defects are *inlet distortion, wake disturbances* introduced by the upstream IGVs and *potential disturbances* from adjacent blade rows. It can also arise from the excitation produced by rotor blades passing through the rotating stall and surge, and from the separated flow on the rotor blades. Large unsteady aerodynamic loads can be experienced by the blades when they pass through these flow defects, especially when the frequency of the unsteady loading is near one of the blade natural frequencies. In addition to the aerodynamic sources described above, forced vibration may also result from mechanical aspects such as blade unbalance,

mistuning and so forth [3]. The lower modes of the blade forced response, such as first bending or torsion, may result in fracture of an entire blade and its attachment. Such a failure may cause large unbalance and severe secondary damage. The damage could even be greater if the blade is not contained. At higher modes, such as second torsion or second or third bending, only outer portion of a blade may fracture, causing some unbalance and significant damage. At even higher modes, only a portion of the tip may break off, causing minimal damage.

Inlet distortion is the physical distortion of inlet which results in the nonuniformity of the inlet core flow. Usually *IGV wake disturbances* and *potential disturbances* are called aerodynamic gust forcing functions [7, 8, 9]. The IGV wake disturbance (or vortices disturbance), a result of viscous action at the upstream IGV surface, is generated by velocity losses in the flow over the downstream rotor blades (see Figure 1.1). A typical wake velocity profile of an IGV is shown in Figure 1.2. The figure indicates that a velocity deficit as compared to the free stream occurs behind the upstream IGV. The IGV wakes decay slowly with distance travelled [10, 11]. On the other hand, potential disturbances (sometimes also named as static pressure or acoustic disturbance) are an inviscid effect which is resulted from finite blade thickness and lifting properties [10, 11]. They extend both upstream and downstream, decaying exponentially in a subsonic flow (but do not decay in a supersonic flow). Therefore, potential disturbance
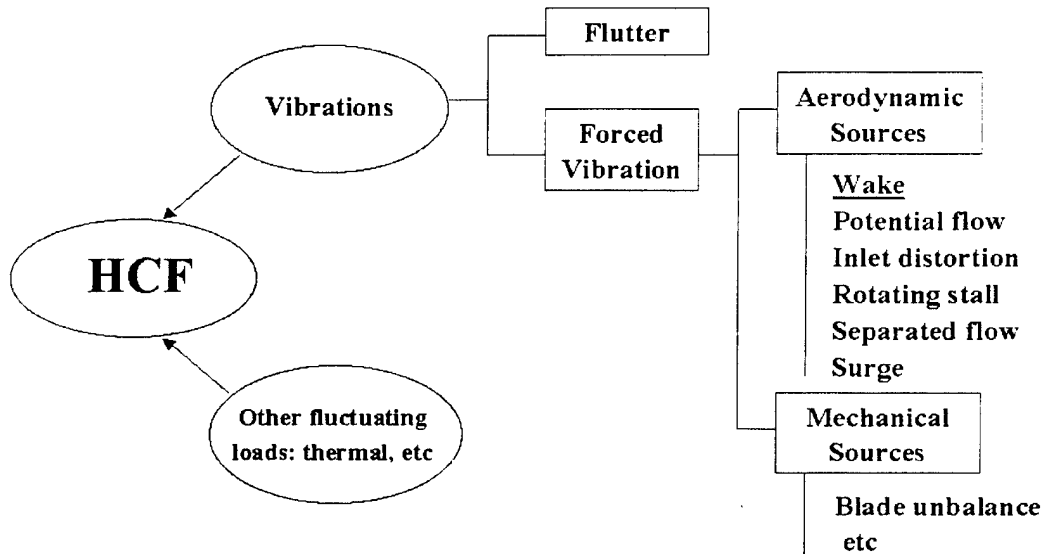
Figure 1.3: Causes of HCF in the rotor blades of gas turbine engines.

is significant for closely spaced blade rows while the wake disturbance is dominant for not-so-closely spaced rows.

A summary diagram for the various causes of HCF is shown in Figure 1.3. In this dissertation, the focus is on the investigations of reducing the IGV wakes, to mitigate blade forced vibrations, and thus HCF.

1.1.2   Current Research to reduce HCF

In the past, a primary blade design consideration for bladed-disk assemblies was LCF. The data base developed over the past decades has served well in bringing LCF related failures under control. However, the changes that have occurred during this period in the design and development of blades and disks has led to failures due to HCF. The problem looms large at the present time and the attempted fixes have been very expensive. However, the current theoretical understanding of HCF is limited and design for HCF tends to be based on experience. Therefore, there is an overwhelming demand within the engine community that a rational basis needs to be developed to address this serious problem.

Preventing HCF failure of engine blades requires a multi-displinary research work. Figure 1.4 shows the basic categories of HCF research [1, 2, 3]. It includes researches on *forced blade response, blade vibration damping, active control, test techniques, health monitoring, materials characterization, robust design,* etc. *Forced blade response* involves investigations of the external forcing functions and blade structural dynamics. The external forcing functions include blade-row wakes, potential field, and inlet distortion. It may also include engine rotating stall and surge when engine is working in

an off-design condition. *Blade passive damping* involves structural damping and aerodynamic damping [12]. Structural damping refers to the damping in the mechanical system while aerodynamic damping results from damping from the aero-mechanical coupling. *Active control* means some amount of external energy is employed to reduce the blade vibration as compared to the passive damping. *Test techniques* means the measurement approaches to the aerodynamic forces, pressure, velocity, blade vibrations when engine is in an operating condition. *Health monitoring* is HCF failure monitoring when aircraft is in service. The purpose of *materials characterization* research is to select and improve blade material life. *Robust Design* involves blade design research on blade flutter reduction, blade forced response, part-to-part and engine-to-engine variability, structural analysis, and so forth.

It is known that the forced vibratory response of a system can be reduced by three possible approaches. The most effective way is the alteration of the system resonant frequencies so that they do not match the external forcing frequencies. Clearly, such management strategy may include the changes in blade geometry (taper, shrouds, aspect ratio, hub tip ratio, etc) [13, 14]. The second approach is to increase system damping to reduce blade vibrations by means of designing dampers such as platform or blade-to-blade dampers. The reduction of forcing functions involves the investigation of the axial spacing of stator-rotor, blade and vane counts, inlet distortion, potential
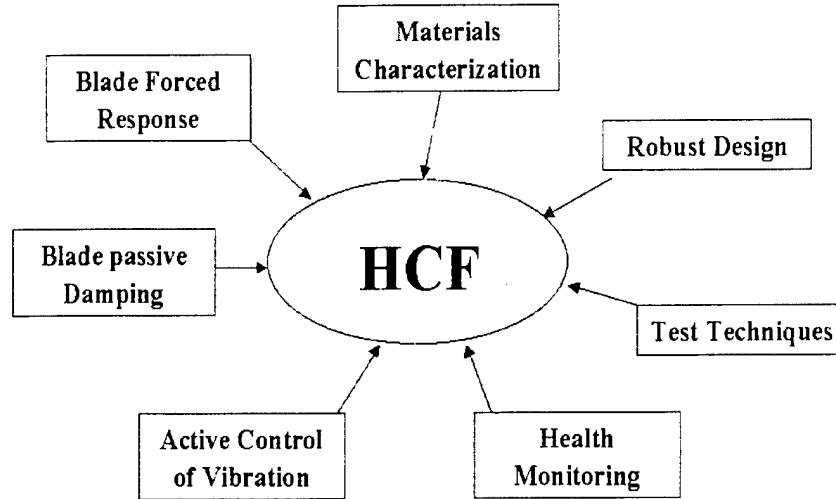
Figure 1.4: HCF research categories.

flows, and re-energizing the stator wakes [15, 16].

This dissertation attempts to attenuate the forcing function by re-energizing the upstream IGV wakes, shown in Figure 1.2, using TEB technique. More specifically, the research effort will be focused on the active optimization of TEB mass flow rate for best wake-filling using automatic control logic. The information obtained from wake sensors is input to a digital processor. According to some control algorithms, the digital processor generates control signals which are fed to the flow actuators to adjust the TEB mass flow rate. The topic involving the TEB technique will be elaborated in the next section.

1.1.3   TEB technique to reduce HCF

Supersonic aircraft inlets typically have IGVs which are placed directly in front of the fan face and normally turn the core flow into the fan rotor. As was stated above, the vortex wakes are created when the boundary layers, that are developed along the surface of the IGVs due to the viscous effect, meet at the trailing edge resulting in a low velocity region compared to the core flow. The TEB technique involves adding the external mass flow at the trailing edges to offset the velocity deficit. By optimizing the TEB rate, the flow into the rotor blades is made more uniform. Consequently, the interaction between rotor and IGV wakes is attenuated, which leads to the reduction of forced blade vibrations, and thus the reduction of HCF. The concept of TEB is shown in Figure 1.5 which is obtained on an F109 turbofan engine [17]. It is noted that the y-axis is the flow velocity normalized by the free flow velocity. As we can see, the wake velocity profile with TEB is almost the same as the core flow velocity, i.e., the wake is re-energized. It is also worth to mention that if we view this problem from the momentum perspective, the wake region constitutes a momentum deficit. Trailing edge blowing tries to remove this momentum deficit by injecting an additional momentum so that the wake region is rendered momentum-deficit-less, or briefly called "momentumless wake". Therefore, a fully re-energized wake is sometimes also called a momentumless wake.
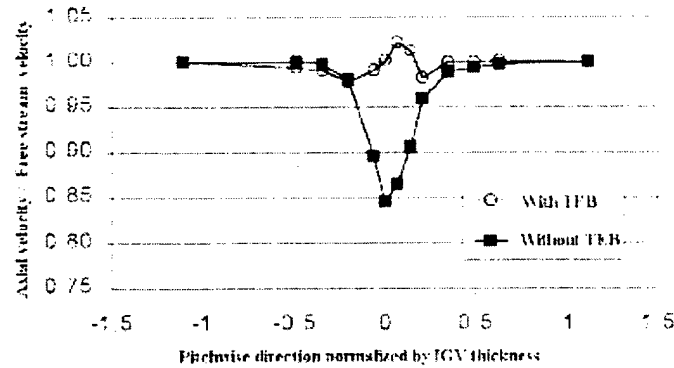
Figure 1.5: The wake profile before and after TEB.

The IGV wakes interacting with downstream rotors are known to contribute not only to forced vibrations in rotor blades, but they generate tonal noise as well. This noise source is generated as the rotor blades chop through the wakes of the upstream IGV's. Hence, TEB has an additional benefit of reducing tonal fan noise through re-energizing the IGV wakes.

Previous work on the wake management using TEB is somewhat limited. Probably the earliest work on momentum injection from a two-dimensional body was done by Wood [18]. His work was conducted using a standard airfoil which was equipped to bleed air from its trailing edge. He discovered that the drag of the airfoil decreased with an increased amount of air flow from the trailing edge. He realized that the drag reduction was caused by the blowing flow to offset the formation of the vorticity caused

by the shear layers. However. he did not address the concept of momentumless wake and the concept of adding momentum to the flow.

Several experiments were performed recently to examine the effectiveness of different wake management strategies. Potential for wake management using TEB to reduce unsteady blade loading has been reported by Waitz et. al [19]. They investigated the effect of rotor wake management by removing and/or adding fluid from the flow around the rotor blade. This study concluded that wake management is feasible and that TEB is more effective and easier to implement than boundary layer suction. Naumann [20], Corcoran [21], and Park and Cimbala [22, 23] had experimentally demonstrated that TEB reduces significantly both the time-mean wake deficit and unsteadiness in wakes shed by flat plates in a water channel. Naumann showed a reduction of about 90% in the time-mean wake deficit and a reduction of greater than 50% in the turbulent velocity fluctuations. Naumann and Corcoran experimented with various blowing configurations. In particular, Naumann compared a continuous slit and a set of discrete jets, with and without vortex generators. This work showed that the most effective method of TEB was to use a set of discrete jets, and that the presence of vortex generators enhanced the mixing of the wake with the jets. More recently. Brookfield and Waitz [24] demonstrated on a 1/6-scale high-bypass-ratio fan stage that the TEB was effective for reducing the rotor wakes and their mean harmonic amplitudes.

Previous experimental research at Virginia Tech by Leitch [25] and Saunders [26] has demonstrated the effectiveness of TEB in reducing the blade passing frequency (BPF) tone. In the work by Leitch, different diameters for the TEB holes were used to achieve uniform wake filling along the span of the strut. Hence, optimum wake filling could only be achieved at one particular engine operating condition. In addition, the TEB pressure was adjusted manually. Far-field sound pressure reading showed noise reduction at the BPF tone of up to 7 dB. His research differed from the current research in that blowing mass flow rate is optimized by wake control systems here.

In addition, few analytical studies on the reduction of tone noise using TEB can are found in the open literature. Waitz et al [19] performed some calculations using the computational codes to determine the sensitivity of the tone noise to specified modification of the wake. A two-dimensional Navier-Stokes cascade solver, UNSFLO was used to parameterize the effects of varying wake width and deficit on unsteady forces on the stator vane. The effects on the acoustic modes were determined using LINSUB (a two-dimensional linearized panel method, using flatplate airfoils). The modification of the wake in their calculation was made by varying the wake width and wake depth.

1.2 Motivations and Objectives of the Research

1.2.1 Motivations

As described above, TEB techniques have been successfully demonstrated to be effective in re-energizing the wakes in realistic rotating environments. In addition, it is also important to mention that the application of TEB for wake management is feasible in real engines, since the technology necessary to employ mass addition strategies is mature. State of the art high pressure turbines require blades with internal passages and small injection ports on the surface for film cooling. Turbine cooling also requires bleed air from the compressor, along with tubing to duct the compressor air to turbine stages. Therefore, the application of TEB to the realistic engine environments in the future is promising.

However, the realistic engine situation may require the use of active control. This research is motivated by the potential advantages of using an active control system. They are:

- Optimum wake-filling can be achieved along the span of IGV's when the flow rate of each TEB hole is adjusted individually by using flow actuators.

- Optimum wake-filling can be maintained as the engine working condition changes due to the tracking capabilities of active controllers.

- The amount of air for TEB can be minimized due to the blowing rate optimization, which is an important factor for TEB technology to be applied to actual engines.

To the author's knowledge, there is no research reported in the open literature on the active control of TEB either experimentally or analytically. The traditional active engine control techniques are employed to increase engine operating range, such as to increase the stall margin [27, 28]. Here, active TEB control is another novel application in the arena of active engine control. This research is devoted to the investigation of active TEB control for the optimization of the wake-filling in a realistic rotating turbomachinery environment to reduce HCF failure and fan noise. Basically, an active TEB control system will involves developing wake sensors, control algorithms and flow actuators. These three control elements will be the topics of the following chapters in this dissertation.

1.2.2 Objectives

Since this is the first research effort on active TEB control, one of the main objectives here is to investigate the feasibility of implementing active flow control systems in a realistic rotating environment. This includes the development of each element of a flow control system: error sensors, flow actuators and control algorithms. Another objective also includes the integration of these components with a digital processor and experimental demonstrations of the system validity on a small scale engine simulator.

The development of practical wake sensing techniques plays a key role for the implementation of TEB control system to realistic situations. Therefore, another objective in this research is to investigate and implement non-intrusive wake sensing approaches. Specifically, acoustic approaches are going to be pursued to sense indirectly the IGV wakes.

Mechanical-Electro-Machine System (MEMS) technology may have considerable potential to affect and manipulate flows and thus to be used in flow control systems. So it is also an objective of this dissertation to integrate MEMS based microvalves into TEB control systems and evaluate its performance as flow actuators.

In addition to the experimental studies, active TEB is also investigated analytically. The effects of mass flow rate, wake-filling shape and axial spacings of IGV-rotor on TEB and inlet noise are investigated. The results could help to develop more advanced acoustic wake sensing strategies.

1.3   Dissertation Outline

The rest of the dissertation is organized in the following manner.

Chapter 2 describes the experimental setup and research facilities used in the TEB control experiments. A general experimental setup is presented to introduce the basic idea of this TEB control research. Research facilities include a small scale turbofan propulsion simulator, IGVs, MEMS based microvalves, digital controllers and so forth.

Chapter 3 reviews the fan noise theory. Basic knowledge of fan noise theory is required for the acoustic measurements in the experiments, and for the design of microphone-based TEB control systems developed in the latter part of this dissertation.

Chapter 4 presents an active flow control system with Pitot probes as wake sensors. The probe-based control system with a PID control algorithm can serve as the baseline case in evaluation of other possible control systems with indirect wake sensors.

Chapter 5 presents active control systems using microphones flush-mounted on the inlet wall as the indirect wake sensors. This non-intrusive sensing technique provides a more feasible approach to control TEB in the realistic engine environments.

In *Chapter 6*, analytical studies are conducted on the active TEB control. The novelty of the investigation is that TEB is taken into account in the noise prediction in the inlet. The results from this chapter are expected to provide theoretical guidance to design advanced acoustic sensing approaches.

Chapter 7 draws up the overall conclusions and outlines possible future work.

Chapter 2

Research Facilities

This chapter describes the experimental setup and research facilities used in the TEB control experiments. Firstly, the general experimental setup is described to introduce the basic idea of this TEB control research. Then, each component of the setup is elaborated one by one in the following sections. A small scale turbofan propulsion simulator is introduced in section 2.2. This simulator is used to simulate the aerodynamic and acoustic signature of the bypass fan in a jet engine. Section 2.3 describes an inlet used with the simulator. Section 2.4 illustrates IGV's which serve as the wake gener-

ators. It is followed by the description of MEMS based microvalves and the digital control hardware. Finally, a complete setup in the Virginia Tech anechoic chamber is depicted.

2.1 The experimental setup

As stated in the previous chapter and shown in Figure 1.1. the first stage fan blades in turbofan engines are most vulnerable to the HCF failure due to the unsteady IGV-rotor interaction. In this study, this first stage rotating environment is simulated by employing a small scale turbofan engine simulator. Since this research is a preliminary step toward a more in-depth investigation of using TEB control to reduce unsteady IGV-rotor interaction, a reduced number of non-turning IGVs (four) is used in the inlet to serve as the wake generator. Non-turning IGVs are used because the simulator is designed to ingest an axial flow only. In addition. the non-turning wakes generated from the straight IGVs provide a simple bench for the preliminary TEB control study as compared to the use of turning IGVs. The first stage is formed by the four IGVs upstream and simulator fan blades downstream.

Figure 2.1 shows a general schematic of the experimental setup used in this research. The main components of the experiments are the inlet, fan rotor, IGV's with TEB, MEMS-based microvalve actuators, error sensors, and the digital controller. As the fan rotates, it draws the air into the inlet. The flow velocity deficit occurs behind the four IGV's when the flow travels through them. When the rotor chops the four wakes, it experiences the unsteady loading which causes blade vibration and fan noise. The MEMS-based microvalves are selected to serve as the flow actuators. A tube providing each TEB hole with the blowing air is connected to a microvalve. The goal of these microvalves is to adjust the TEB rate to achieve the best wake-filling for each IGV.

This figure also depicts the general idea of TEB control approach. The feedback control loop begins with the sensing of the wakes. The kernel part is the digital signal processor (DSP) which implements the control algorithms. The controller takes the input from the wake sensors and generates the output according to the control algorithms. The output provides the control signal for the microvalves to adjust blowing rate to re-energizing the wakes. Hence, a feedback loop is formed. This research is focused on investigating different wake sensing approaches, developing of control algorithms, and the implementation and validation of these control concepts. These control approaches will be described in detail in the following chapters. The various components of the experimental setup are now described in the following sections.
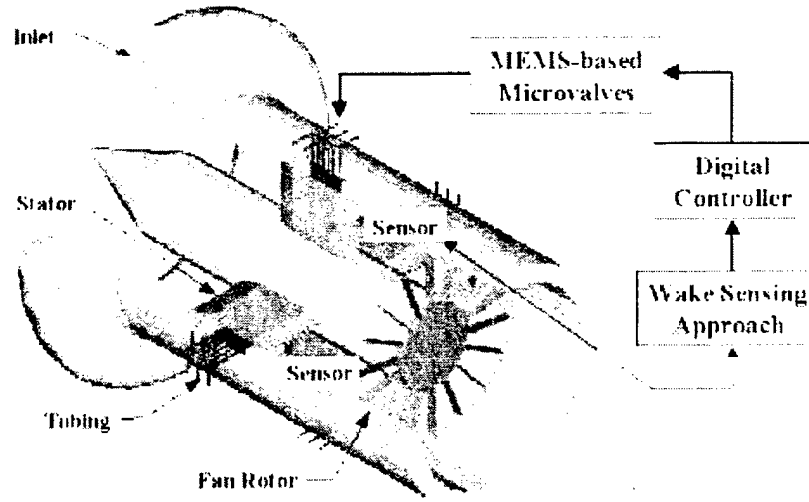
Figure 2.1: The experimental setup for TEB control.

2.2 Turbofan propulsion simulator

The turbofan propulsion simulator (TPS) (Model 460) from Tech Development Inc., provides the rotor for investigating IGV-rotor unsteady interaction effects. It is represented by the *Fan Rotor* in Figure 2.1. The TPS simulates the acoustics and aerodynamics of a high bypass fan in an aircraft gas turbine engine. Figure 2.2 is a photograph of the simulator and its rotating components. The TPS works in a fashion similar to an ordinary gas turbine, except without a combustor. The power turbine is a single stage with 29 blades and driven by high-pressure air. The single stage turbine can
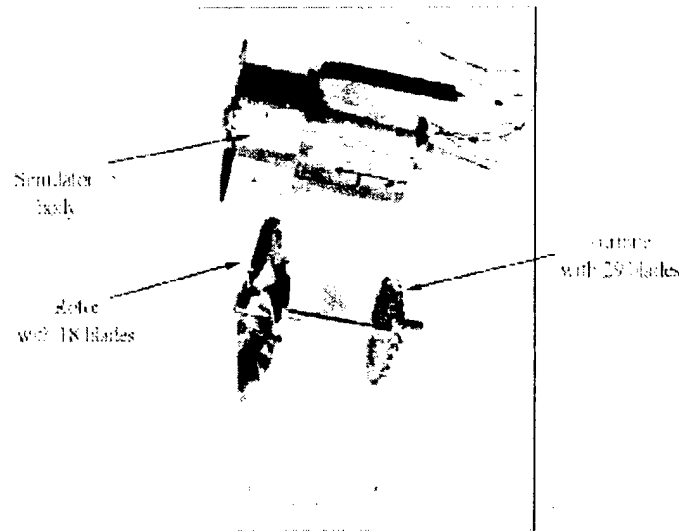
Figure 2.2: Turbofan propulsion simulator (TPS).

handle a maximum mass flow rate of 1.50 lbm/sec (0.68kg/sec.) and is connected on a

shaft to a single stage rotor. The 18-blade rotor has a diameter of 4.1 inches (10.4 cm)

with a hub to tip ratio of 0.44 at the fan inlet. It is capable of developing a maximum

pressure ratio of 1.6 at a mass flow rate of 2.72 lbm/sec (1.23kg/sec.). and maximum

speed of 80.000 rpm. A row of 26 Exit Guide Vanes (EGV) is present one rotor chord

length downstream of the fan. These guide vanes also cause far-field noise radiation

due to the unsteady lift generated by the passage of rotor wakes. Instrumentation on

the TPS turbine includes thermocouples to measure the turbine bearing temperatures

and a magnetic speed pickup to measure the rotational speed. The fan blade tip speed

becomes supersonic at the speed of 65,000 RPM.

2.3   Inlet

Many different inlet configurations can be mounted on the TPS body. This research requires an inlet to be designed such that it focuses on the rotor-IGV interaction effects. In this study. the symmetric inlet design used in previous research by T. Leitch [29] is used as shown in Figure 2.3.

Figure 2.3 compares the inlet used in this study and representative supersonic and subsonic inlets. The inlet is longer than a conventional subsonic inlet and equipped with a centerbody supported by the IGV's. On the other hand. the inlet is shorter than a typical supersonic inlet. The centerbody is greatly simplified. and the outer profile does not accelerate the flow through the inlet.

Figure 2.4 shows a three dimensional view of the inlet alone. The inlet is a constant area with a diameter of 4.1 inches (10.4 cm). A larger diameter step at the discharge end allows the inlet to be mounted on the simulator. The mouth of the inlet is provided with a bellmouth to avoid inlet flow separation. Five tapped holes are provided circumferentially. The centers of four of these holes line up with the trailing edge of each IGV, and the remaining one is positioned in the free stream (not shown in Figure

(a) Subsonic inlet

(b) Inlet used in this research
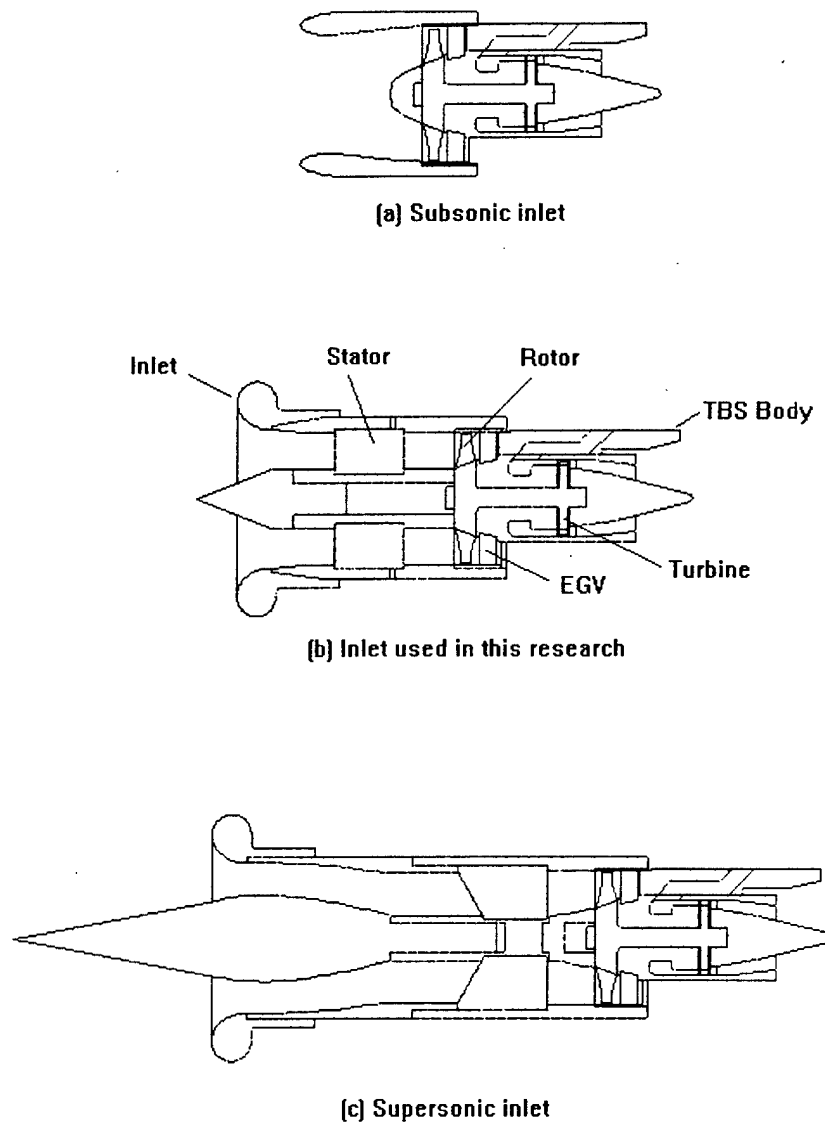
(c) Supersonic inlet

Figure 2.3: The inlet used in this research compared to supersonics and subsonic inlets.

Bellmouth

Centerbody

Inlet

IGV

**Holes for Pitot probes
or Microphones**
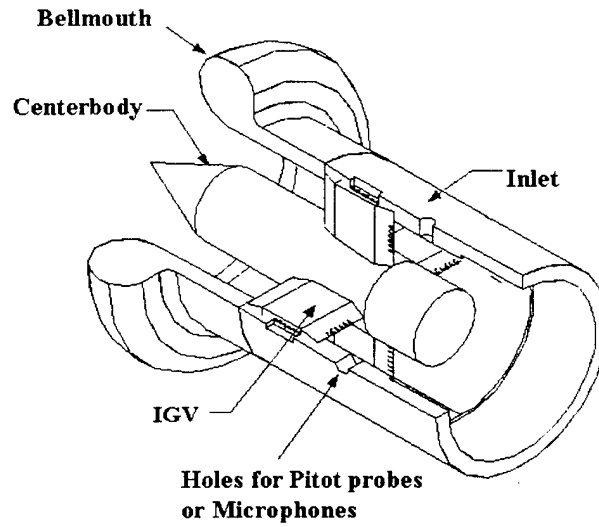
Figure 2.4: The cutaway view of the inlet.

2.4). These holes are used for mounting either Pitot probe flow sensors or microphone sensors. The centerbody is a cylinder with a conical section at the inlet. This allows for smooth turning of the flow entering the inlet. The annulus area between the centerbody and inside diameter of the inlet is of constant cross section. Four slots are cut on the surface of the centerbody, 90 degree apart. The IGV's are placed in these slots and hence a smooth geometric transition is obtained. Upon assembly, care must be taken to fill in all cavities, to avoid the interaction of the rotor with flow distortions generated by these cavities.

2.4 Blowing IGVs

The four IGVs (also referred as stators in the text where appropriate), which support the centerbody, also serve as the wake generators. They introduce spatially periodic distortions, i.e. four wakes in the flow field ingested by the rotor. The IGVs are faceted, with sharp leading and trailing edges and provide no turning to the flow. The geometry of these struts is very similar to those used by T. Leitch [30], except for the trailing edge geometry. The trailing edge used here is sharp as compared to the blunt edge used by Leitch [30]. The sharp trailing edge has the effect of reducing the width. This also results in a reduction of the far-field sound levels generated for the baseline case with no trailing edge blowing.

The trailing edge of the IGVs is provided with six equally-spaced blowing holes. The size and spacing of the trailing edge blowing holes are critical to provide uniform span-wise re-energizing of the IGV's wakes. The goal in designing the trailing edge hole configuration is to produce a blowing profile from the tip to the hub that matches the wake profile. A secondary consideration is that the hole configuration be designed to use a minimal amount of blowing air. After a series of bench tests, Leitch [25] concluded that six equally-spaced holes along the span provided the best configuration.

In addition, Leitch used different hole diameters to achieve uniform wake filling along the span of the IGV. In this research, the trailing edge holes have the same diameters because the supply air is adjusted for each hole individually using MEMS based microvalves. The IGV used in the research is shown in Figure 2.5 while Figure 2.6 gives the detailed dimensions. The hole centers are spaced two hole diameters apart. The blowing holes are 1/16 inches (0.16 cm) in diameter. Each hole is 'L' shaped and opens out at the top of the IGV in a 1/8 inches (0.32 cm) diameter hole. Because of the sharp trailing edge, the blowing holes create a crenellation as they open out on the trailing edge. This is expected to aid in mixing of the discrete jets and the wake. Leitch [25] pointed out that reduction in tone was obtained in spite of lack of adequate wake filling at the hub. Hence the blowing holes are moved up so that in the bottom 25% of IGV height the wake is not completely re-energized.

The IGV's are positioned so that the fan face is an IGV chord length downstream of the trailing edges, i.e., 2.088 inches (5.303 cm). Bench tests showed that for uniform pitchwise mixing in the wake at least 0.5 IGV chord length is required as illustrated in Figure 2.7. This means that if a flow sensor is used, it has to be placed no less than 0.5 IGV chord length downstream of the IGV trailing edge to ensure that the sensor would measure the mixed out flow from the jet-wake system, rather than the jet issuing out of the blowing holes. This is an important consideration for the implementation of
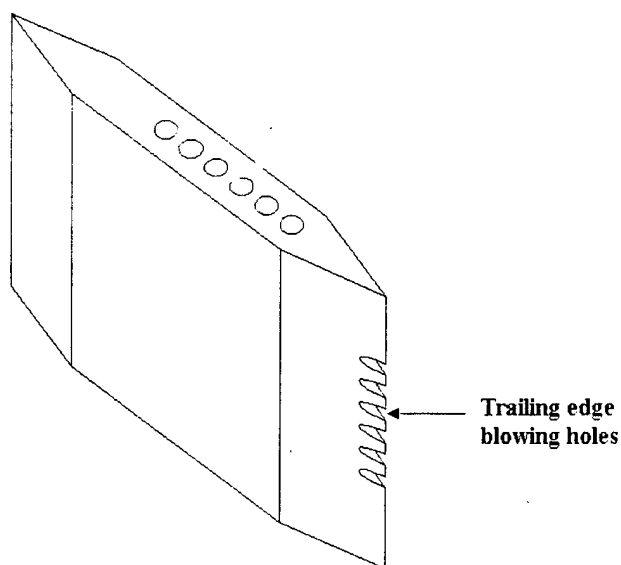
Figure 2.5: The IGV with six blowing holes.
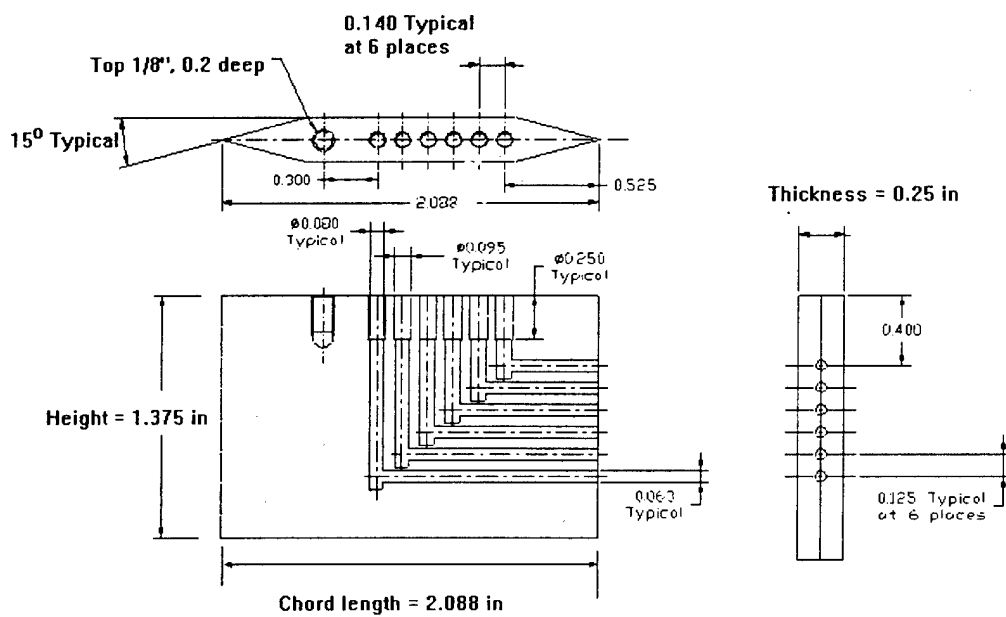
Figure 2.6: Geometry of the IGV.
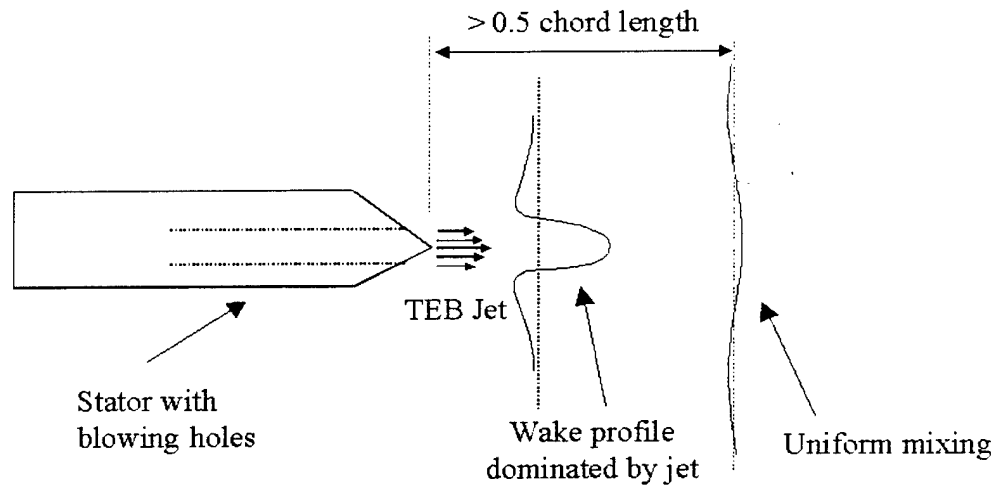
Figure 2.7: The jet mixing process.

active flow control using flow sensor as described in Chapter 4.

2.5 MEMS technology and MEMS based microvalve

Since one of the objectives in this research is to investigate the feasibility of integrating the MEMS technology into the TEB control systems, a basic background review of MEMS is introduced first in the following subsection. MEMS is a field which is rich in scientific challenges as well as an enabling technology for broad engineering

applications.

2.5.1 MEMS Technology

MEMS differ from IC's (integrated circuits) in that they consist of both mechanical and electrical devices. While the electronic devices provide the MEMS with the functionalities of IC's, the integration of the mechanical devices such as sensors and actuators enable MEMS to interact with the external environment. Although electrical devices were well established technically, the study of mechanical devices such as microactuators began only about two decades ago. In the past, almost all the mechanical parts had sizes much larger than the electronic elements because the traditional manufacturing technology lacked the capability to fabricate small mechanical parts. In 1983, a new manufacturing process, the surface micromachining technology [31] became available which could be used to manufacture the micron sized mechanical devices with sophisticated geometry. Since then, a remarkable progress has been made and some MEMS products have been marketed [32, 33]. MEMS technology is so attractive due to its three characteristic features or three "M"s [33]: *Miniaturization, Multiplicity* and *Microelectronics. Miniaturization* is clearly essential: *Multiplicity* is the key to suc-

cessful microsystems and *Microelectronics* is critical for mechanical parts to cooperate with each other and to perform a given task. The application areas of MEMS include optics, transportation and aerospace, robotics, biotechnologies, medical engineering, etc. It is widely believed that MEMS technology will have profound impact in the future society just like the invention of IC chips forty years ago.

There are numerous opportunities for applying MEMS to flow control. For example, Ho et al [34, 35] demonstrated the effectiveness using MEMS to modify the streamwise development for shear flow. MEMS based micro transducers for flow control can easily increase the temporal response to a large extent because of the low inertia of the transducer [36]. Some other good examples for MEMS used in the arena of flow control include MEMS based micro anemometer, micro shear stress sensor, micro pressure sensor, micro actuator, etc [37].

2.5.2 MEMS based microvalves

In this research, we aim to integrate MEMS technology, i.e., MEMS based microvalves, into the active TEB control systems as flow actuators. In the active TEB control
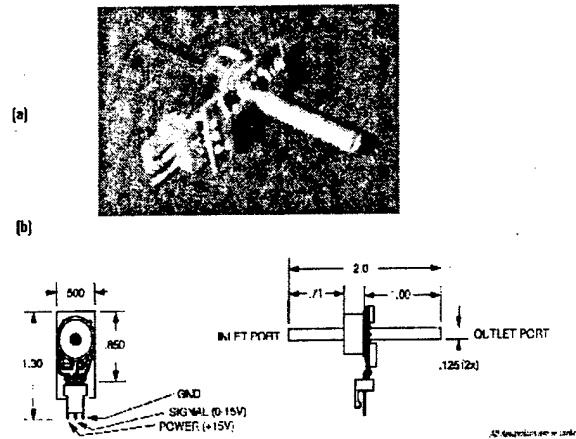
Figure 2.8: The MEMS-based microvalve used to control TEB rate (a) picture and (b) dimensions.

systems developed in Chapters 4 and 5, individual control of the blowing rate of each hole is obtain d by the use of MEMS based microvalves. The microvalves used for this research are NO-3000 Fluistor, supplied by Redwood Microsystems [38, 39]. The microvalves are Normally Open (NO), i.e. if no signal voltage is applied the microvalves are fully open and operate at maximum flow rate as governed by the source pressure. The design specifications are given in Table 2.1. Figure 2.8 shows the microvalve and the external dimensions and pin connections. Figure 2.9 depicts the principle of operation of the microvalves. The microvalve operates on the thermo-pneumatic principle. The actuator is a sealed cavity, which holds the control liquid inside it.

Table 2.1: MEMS-based microvalve specifications.

Fluid Media	Non-corrosive gases
Outlet Pressure Range	0 − 100 psig (0 − 6.89E5 pa)
Maximum Supply Pressure	100 psig (6.89E5 pa)
Proof / Burst Pressure	150 / 250 psig (1.03E6 / 1.72E6 pa)
Flow Rate Range	0.2 − 3000 sccm (4.1E-12− 6.15E-8 kg/sec)
Response Time	500 ms typical
Average Power Consumption	700 mWatts
Operating Temperature Range	0 − 40 C
Control Signal Voltage Range	0 − 15 Volts
Power Supply	15 Volts

One wall of the cavity is a diaphragm, which flexes when the cavity pressure increases due to evaporation of the liquid. A thin film resistor provides the heat required for vaporization. The flexing of the diaphragm wall is translated into valve movement. Thus, flow rate is governed by varying the signal voltage that for a Normally Open valve is from 0 to 15 volts. However, it is found that the microvalve performance depends on initial conditions such as fully open, fully close, or partially open. Figure 2.10, which shows the dynamic pressure measured at the exit of the microvalve as a function of the signal voltage, is obtained when the microvalve starts from the initial condition of fully-open [40]. It is also observed that the microvalve has a response time

of about 10 seconds if it starts from an initial condition of fully close. On the other hand, the time response is about 3-4 seconds if it starts from partially or fully open condition. This indicates that the microvales has a very slow response. Hence, the measurements for Figure 2.10 were conducted when the dynamic pressure has reached steady state condition. It can be seen from Figure 2.10 that the microvalve exhibits a nonlinear operation near the fully open and fully closed regions. The figure also shows that the effective voltage operating range is supposed to be from 3 to 9 volts.

Aerodynamic studies are first conducted to investigate the effectiveness of wake-filling obtained by controlling individual blowing holes, before the tests on the small scale engine simulator are carried out in the anechoic chamber. This initial step is important because the performance of MEMS-based microvalves as flow actuators needs to be evaluated. As mentioned in Chapter 1, this is one of the research objectives because flow actuators play an important role in TEB control systems.

The experiments are conducted on a test bench by Rao [41, 42]. The aerodynamic results are presented in the form of 2-D contour plots, in Figure 2.11. The X-axis is the pitchwise direction, nondimensionalized by the IGV thickness. The Y-axis is the spanwise direction, nondimensionalized by the IGV height. The contours display the ratio of the axial velocity to the maximum free stream velocity. The choice of
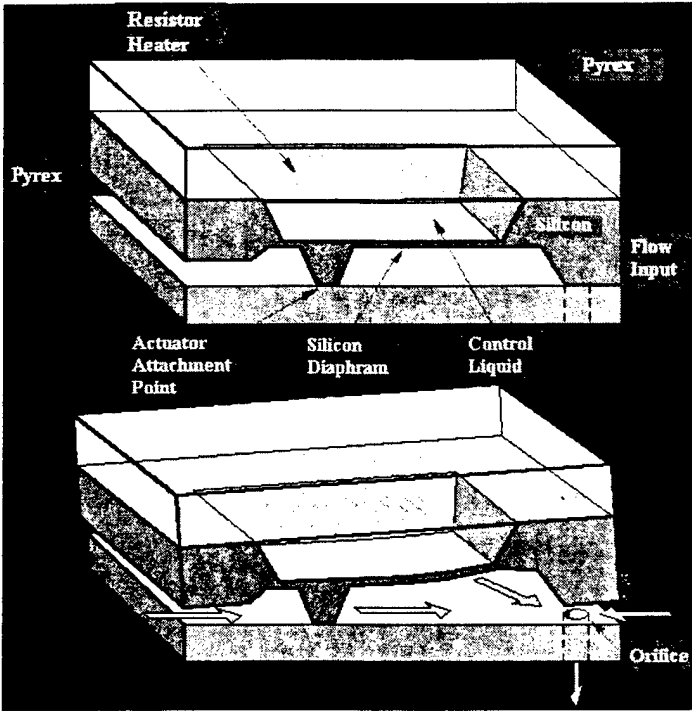
Figure 2.9: The MEMS-based microvalve working principle.
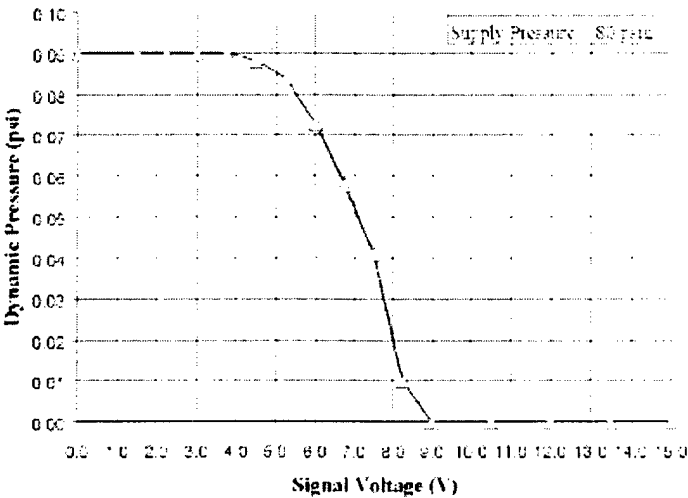
Figure 2.10: The performance curve of MEMS based microvalve.

maximum free stream velocity is made to assign a common base for all ratios. and also to bring out the variations that exist in the flow field. Also seen in these plots are two vertical lines at 0.5, representing the maximum thickness of the IGV. The circles with crosshairs represent the location of the trailing edge blowing holes. Data is acquired 0.5 IGV chord lengths downstream of the IGV, with and without blowing.

Figure 2.11(a) is a velocity contour plot of the baseline case, i.e. without trailing edge blowing. The wake is centered about the trailing edge of the strut, as seen by the maximum velocity defect occurring at the X-axis origin. Also noted from this figure is that the free stream axial velocity is not uniform in the spanwise direction. Figure 2.11(b) shows the velocity ratio contours with the application of trailing edge blowing. The data is acquired after the blowing rate of each blowing hole is optimized by adjusting the control voltage to the MEMS based microvalve. The blowing rate is optimized when the total pressure in the wake equals the free stream total pressure. Figure 2.11(b) indicates that at most spanwise locations, the wake velocity is equal to or varies in small amount with the axial velocity in the free stream at the same span. In addition, the spanwise variation of axial velocity in the wake is very similar to that in the free stream. These results have demonstrated the advantage of individual hole control by using MEMS based microvalves in the presence of spanwise variations in free stream axial velocity.
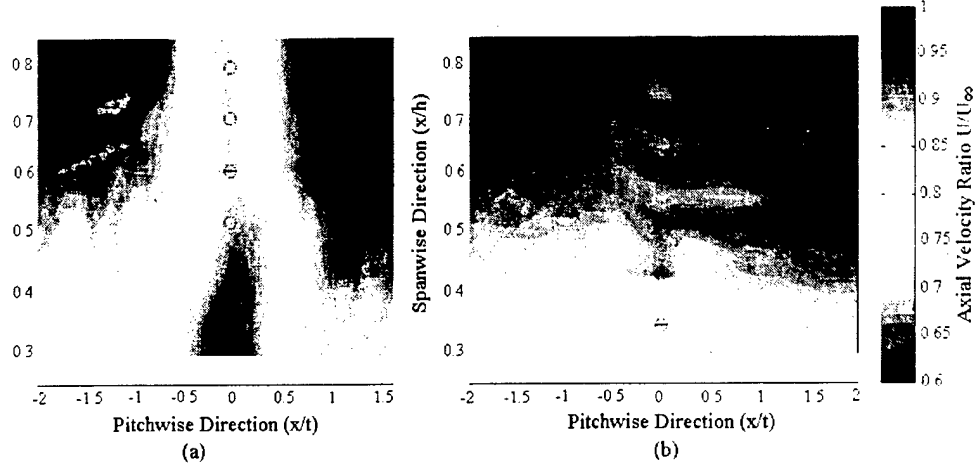
Figure 2.11: Comparison of axial velocity ratio (a) without TEB, (b) with TEB.

2.6   Digital Signal Processing Board

The control algorithms in this research are implemented in software on a digital sig-

nal processing board from *Spectrum Signal Processing Inc.* The kernel part of the

board is the processor TMSC320C30 manufactured by Texas Instrument [43]. The

TMSC320C30 DSP contains integer and floating-point arithmetic units. 2048 × 32 bit

words of on-chip RAM, 4096 × 32 bit words of on-chip ROM, control unit with parallel

and serial interfaces. Operating from a 33.3MHz clock, a performance of 16.7 million

instruction per second is achieved. The peak arithmetic performance of 33.3 million

floating-point computations per second is attained when the floating-point multiplier

and adder are used in parallel. This board is also equipped with dual channel 16 bit A/D and D/A systems, a parallel expansion system referred to DSPLINK and a serial expansion interface. The board is mounted in a personal computer when it is in use. Access to memory passes through the dual porting hardware on the board.

In our application case, an external 16-channel D/A board and an external 32-channel A/D board are utilized to work with the DSP card through DSPLINK, since the number of on-board input/ouput A/D and D/A channels is not sufficient. Each channel in the A/D board consists of a double buffered 12 bit DAC, 2nd order programmable analog output filter and buffer amplifier. The output from the card ranges from - 8.192 volts to 8.192 volts. The 32 analog input channels in the A/D card are multiplexed to a fast (3 $\mu sec.$) 12 bit ADC. All 32 channels have input buffering and a first order low pass to reduce unwanted high frequency noise. The channels are arranged in groups of 4, the channels in each group being sampled simultaneously allowing differential signal acquisition.

2.7 Schematic setup in anechoic chamber

Figure 2.12 describes a schematic of the entire active flow control setup for testing in the Virginia Tech anechoic chamber. An air tank with compressed air is used to power the simulator as well as it is connected to a plenum that provides the air source for TEB. The simulator and the active flow control components are placed in the anechoic chamber. The anechoic environment is required since the acoustic effect of the TEB is monitored. The Virginia Tech anechoic chamber with a dimension of $13.1 \times 8.9 \times 6.6$ ft ($3.99 \times 2.71 \times 2.01$ meter), is constructed with Owens Corning Type 705 industrial fiberglass wedges. It can be considered anechoic for frequency above 200 Hz, which is far below the blade passing frequency in the tests. The ambient noise pressure level is about 30 dB (Ref. 20×10^{-6} Pa). This ambient noise level does not affect the measured noise level during testing since minimum in-test noise level is above 70 dB.

The simulator is mounted onto the top of a test stand which is placed at the center of the chamber. The test stand is 1.2 meters (47.2 inches) in height above the elevated chamber floor to minimizing the potential of ingestion of ground vortices, which would add to inlet distortions. A 2-inch (5.08 cm) diameter air line is flange mounted to the top plate to provide the high pressure air to power the simulator. The inlet slides onto
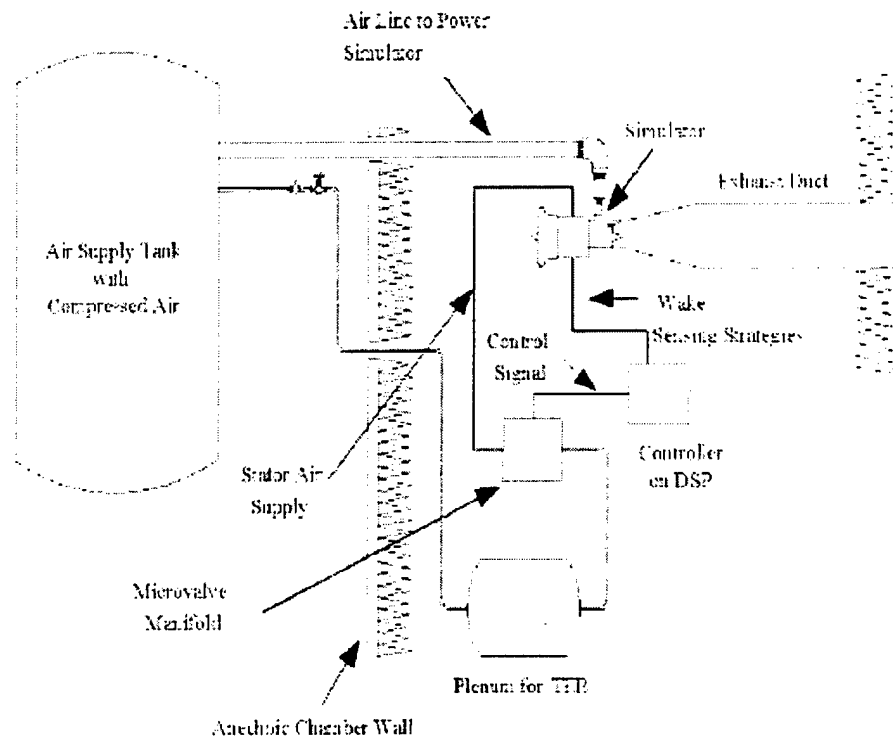
Figure 2.12: The schematic setup in Virginia Tech anechoic chamber.

the simulator fan shroud and is held in place by a cowl. The cowl runs the length

of the simulator and forms an exhaust duct for the turbofan discharge. An orifice

plate is placed inside the cowl and located using set screws. Loading of the turbofan

is controlled by the area of the annulus formed by the orifice plate with the turbine

exhaust duct. The turbine exhaust is ducted separately from the fan exhaust so as not

to affect the fan loading. Well downstream of the simulator exit, the exhausts from the

turbine and fan are mixed in the exhaust pipe. The exhaust pipe is 12 inches (30.48 cm) in diameter, made from sheet metal, and exhausts turbine and fan air into the atmosphere.

Compressed air is required not only to power the simulator but also to supply blowing air. An Ingersoll-Rand four-stage reciprocating compressor meets the compressed air requirements. The compressed air facility is equipped with an activated-alumina drying unit and a heat exchanger. This ensures that the compressed air that drives the turbine is free of water vapor and also at room temperature. The compressed air is carried by a main line that is 2 inches (5.08 cm) in diameter. It is fitted with a solenoid valve that serves as an emergency shut-off. An 1-inch (2.54 cm) line from the main supply line taps off air required for blowing. The air is routed to a supply plenum placed in the chamber. An air regulator mounted on the feed line maintains plenum pressure. Four pipes connect the supply plenum to a manifold. The manifold is a block of aluminum with four 1/4-inches (0.635 cm) holes drilled into it. Each hole has six tapped holes. Microvalves are mounted in these holes using Swagelok fittings. Each microvalve is connected to a single blowing hole on an IGV through Tygon tubing. Care is taken to ensure that each joint is leak proof.

A Toshiba process loop controller Model EC321 [44] in conjunction with Peek Mea-
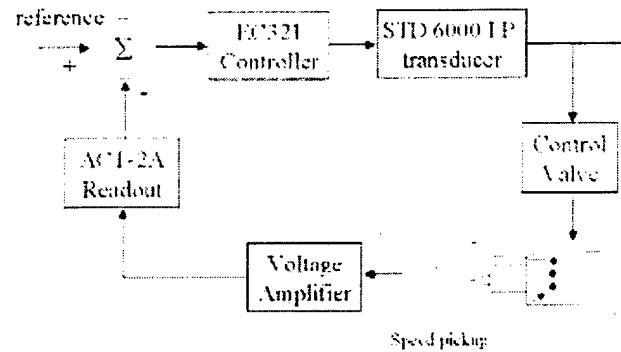
Figure 2.13: The simulator speed control system.

surement STD 6000 I/P (current to pressure) transducer [45] and ACT-2A simulator

speed readout is used for simulator speed control. The control configuration is shown

in Figure 2.13. Basically the process controller EC321 is a PID (proportional-integral-

derivative) feedback controller with programmable functions. The STD 6000 I/P trans-

ducer serves as the actuator for EC321 controller while the simulator speed readout

ACT-2A can be viewed as the control system sensor. This readout uses the pulses

from the 6 magnetic speed pickups that are built in the simulator as its input after

they are amplified by a gain of 10. Reference speed is set by the user using internal

programmable functions.

Chapter 3

Turbofan Noise Theory

A review of fan noise theory is required for the design and implementation of TEB control systems using the acoustic sensing approaches in the latter part of this dissertation. In section 3.1, the relationship between fan noise and blade vibration in terms of the common generation mechanism is introduced. The basics of fan noise theory includes the generation of tone frequencies, excited acoustic duct modes and propagation behavior in a circular duct.

3.1 Introduction

Noise from turbofan and jet engines is one of the most significant noise sources of military and commercial aircraft. The acoustic signature of the aircraft engines is characterized by a broadband noise level with dominant discrete tones at blade passing frequency (BPF) and its harmonics. Among the discrete tones, the noise level at BPF tone is usually the loudest. For subsonic fans, these discrete tones are usually 10-20 dB above the broadband level. For transonic fans, additional tones also appear in the inlet at frequencies submultiples of the BPF due to the shock waves at the tip of the fan blades. These tones are commonly referred as" multiple tones", or "combination tones". However, these tones will not be present in this research because the turbofan simulator is always operated at subsonic conditions. Broadband noise is generated by the interaction of random disturbance, e.g., those associated with turbulence boundary-layer flows over rotor blades, stators, shroud, ingested atmospheric, and blade tip vortex shedding. Broadband noise tends to dominate the spectrum at low flow coefficients when the stage is heavily loaded and is very near to or in stall [46]. The BPF and harmonic tones are generated by the aerodynamic interaction of wakes from either blades or vanes with downstream vanes or blades, respectively. Studies have shown that one of the most significant noise source interactions is due to the upstream IGV

wakes and rotor blades, i.e., IGV-rotor interaction. Other tonal noise sources may include the rotor-EGV interaction and rotor-rotor interaction as well [47, 48].

The noise generation mechanism associated with IGV-rotor interaction is the unsteady lift experienced by the blades when they pass through the upstream IGV wakes. Therefore, blade vibrations and tonal fan noise shares as a common forcing function the upstream IGV wakes. In other words, the IGV wakes cause both blade vibrations and tonal fan noise as shown in Figure 3.1. Therefore, when the wake is fully re-energized by TEB, both blade vibration and fan noise will be minimized. This implies that acoustic sensing approaches can be employed in active TEB control systems to re-energize the IGV wakes for the reduction of blade vibrations and HCF. From this point of view, microphones used for acoustic sensing can be viewed as the indirect "wake sensor" and thus offers the potential for the implementation of active TEB. As shown in the latter chapters, the acoustic sensing strategy will be successfully implemented on the small scale engine simulator which becomes a significant contribution of this research endeavor.

It is also worth to point out that TEB technique brings us an additional benefit which is the attenuation of engine fan noise. In effect, trailing edge blowing from stator vanes or rotor blades has been successfully demonstrated as a new method to reduce engine
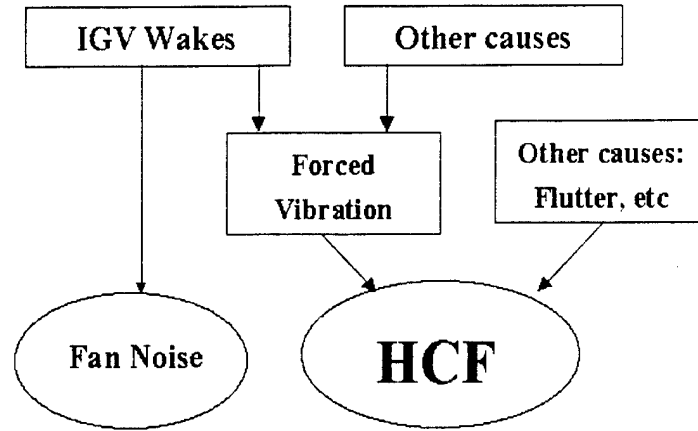
Figure 3.1: The relationship between wake, tone noise and blade vibration(HCF).

fan noise in a realistic rotating environment [19, 24, 25].

3.2 Turbofan Noise Theory

Turbofan tonal noise theory includes the generation and propagation of acoustic modes. The first aspect is the understanding of how the acoustic modes are generated while the second is how the acoustic modes propagate along the inlet duct.

As mentioned above, the acoustic spectra of the fan noise is dominated by tones at

BPF and its harmonics. The BPF is computed as:

$$f_{BPF} = \Omega \cdot N_B / 60 \quad [\text{Hz}] \tag{3.1}$$

where Ω is the speed of the rotor in revolution-per-minute and N_B is the number of rotor blades.

3.2.1   Duct Acoustic Modes

The homogeneous wave equation for sound pressure in a moving media is given as [49]:

$$\nabla^2 p - \frac{1}{c^2} \left(\frac{\partial}{\partial t} + \vec{V} \cdot \nabla \right)^2 p = 0 \tag{3.2}$$

where ∇^2 is the Laplacian operator; $p(r, \theta, z, t)$ is the sound pressure in cylindrical coordinate r, z and θ are the radial, axial, and circumferential coordinates, respectively, as shown in Figure 3.2; c is the sound speed in the media; and $\vec{V} = cM\vec{k}$ is the flow velocity field vector in the z-direction where M is the flow Mach number.

By solving the homogeneous Eqn. (3.2), the general solution for the sound field in the duct can be expressed as a linear combination of eigenfunctions [50]:

$$p(z, r, \theta, t) = \sum_{m=0}^{M_c} \sum_{\mu=0}^{M_r} A_{m\mu} \Phi_{m\mu}(r, \theta) e^{-ik_{z,m\mu} z} e^{i2\pi n f_{BPF} t} \tag{3.3}$$
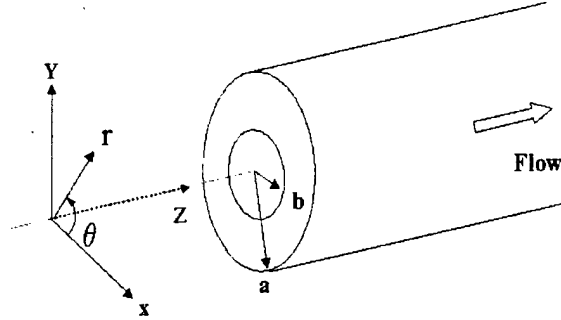
Figure 3.2: Sound field in cylindrical coordinates.

where $p(z, r, \theta, t)$ denotes the tonal acoustic pressure generated at the frequency of

$n \cdot f_{BPF}$, where $n = 1, 2, 3 \cdots$ indicates the harmonics of the BPF; and $\Phi_{m\mu}(r, \theta)$ is

the acoustic mode with a complex amplitude $A_{m\mu}$. The acoustic mode is defined by

two indices m and μ representing circumferential and radial variation, respectively;

M_c is the number of circumferential modes while M_r is the number of radial modes

included. The axial propagation characteristic of the (m, μ) mode is defined by the

axial wavenumber $k_{z,m\mu}$, which will be described in Section 3.2.2.

The acoustic mode shape $\Phi_{m\mu}(r, \theta)$ can be found by solving the wave equation (3.2)

together with the boundary conditions. For example, in a concentrical duct with rigid

walls, the following boundary conditions should be satisfied:

$$\left[\frac{\partial p}{\partial r}\right]_{r=a} = 0 \tag{3.4}$$

$$\left[\frac{\partial p}{\partial r}\right]_{r=b} = 0 \tag{3.5}$$

where a is the outer radius and b is the inner radius of the annular duct as shown in Figure 3.2. Equation (3.4) and (3.5) basically state that the radial particle velocity vanishes at $r = a$ and $r = b$ since rigid wall is assumed. From the boundary conditions, the characteristic equation for the eigenvalue problem can be found[49, 50] as:

$$\frac{J'_m(k_{m\mu}a)}{J'_m(k_{m\mu}b)} = \frac{Y'_m(k_{m\mu}a)}{Y'_m(k_{m\mu}b)} \tag{3.6}$$

where $J_m(\cdot)$ is the first kind m-order Bessel function and $Y_m(\cdot)$ is the second kind m-order Bessel function; J'_m and Y'_m mean the derivative of J_m and Y_m, respectively; and $k_{m\mu}$ is the root of Eqn. (3.6). It is noted that for each m there is an infinite set of μ, i.e., $\mu = 0, 1, 2 \cdots$. Since m is associated with the circumferential coordinate θ as will be seen in Eqn. (3.8), m is usually referred as the circumferential order of the acoustic mode while μ is called the radial order for the similar reason. Hence, one circumferential mode is associated with a series of radial modes. To this end, the mode shape $\Phi_{m\mu}(r, \theta)$ can be expressed as [50]:

$$\Phi_{m\mu}(r, \theta) = \Theta(\theta) \left[J_m(k_{m\mu}r) - \frac{J'_m(k_{m\mu}a)}{Y'_m(k_{m\mu}a)} Y_m(k_{m\mu}r) \right], \qquad b \leq r \leq a \tag{3.7}$$

Because the sound field in the circumferential direction must be periodic, the function

$\Theta(\theta)$ takes the form

$$\Theta(\theta) = cos(m\theta + \phi_{m\mu}) \tag{3.8}$$

where the initial mode phase $\phi_{m\mu}$ is a constant. Substitution of Eqn. (3.8) and Eqn. (3.7) into Eqn. (3.3) leads to the complete sound field expression:

$$p(z, r, \theta, t) = \sum_{m=0}^{M_c} \sum_{\mu=0}^{M_r} A_{m\mu} cos(m\theta + \phi_{m\mu}) \cdot$$

$$\left[J_m(k_{m\mu}r) - \frac{J'_m(k_{m\mu}a)}{Y'_m(k_{m\mu}a)} Y_m(k_{m\mu}r) \right] e^{-ik_{z,m\mu}z} e^{i2\pi n f_{BPF}t} \tag{3.9}$$

It is convenient to illustrate the modal behavior by considering a simple case of the circular duct with $b = 0$. The mode shapes and the characteristic equation can be found from Eqn. (3.7) and Eqn. (3.6) by setting b to zero. They are

$$J'_m(k_{m\mu}a) = 0 \tag{3.10}$$

and

$$\Phi_{m\mu}(r, \theta) = cos(m\theta + \phi_{m\mu}) J_m(k_{m\mu}r) \tag{3.11}$$

Thus, equation 3.10 allows to solve for the roots, $k_{m\mu}$. As mentioned before, for each value of the circumferential order m there exists an infinite sequence of radial modes. Table 3.1 contains a few of the values for $k_{m\mu}a$. It should be noted that the first radial mode is $\mu = 0$ because the plane wave is usually referred as mode $(0, 0)$.

Table 3.1: The values for $k_{m\mu}a$ for a circular duct with a radius of a.

m\ μ	0	1	2	3
0	0	3.83	7.02	10.17
1	1.84	5.33	8.54	11.71
2	3.05	6.71	9.97	13.17
3	4.20	8.02	11.35	14.59

Figure 3.3 illustrates several acoustic modes where the initial phase $\phi_{m\mu}$ is assumed to be zero. The nodal lines, as denoted by dotted lines in the figure, occur at the zeros of the mode shape $\Phi_{m\mu}(r, \theta)$ in circumferential and radial directions. It is apparent that the integer m equals the number of radial nodal lines while the integer μ equals the number of azimuthal circles. The symbol "+" in the figure means that the sound pressure in the specified region is out of phase as compared to that in the region denoted by "-".

Tyler and Sofrin [47] used the above model to analyze the BPF and its harmonics generated in a compressor. The model considered a stator and a rotor with a rotating speed of Ω in the positive θ-direction in a circular duct. They came up with two important results in their work. First, they realized that the acoustic modes from the turbofan engine are not stationary as discussed above, instead they are the spinning
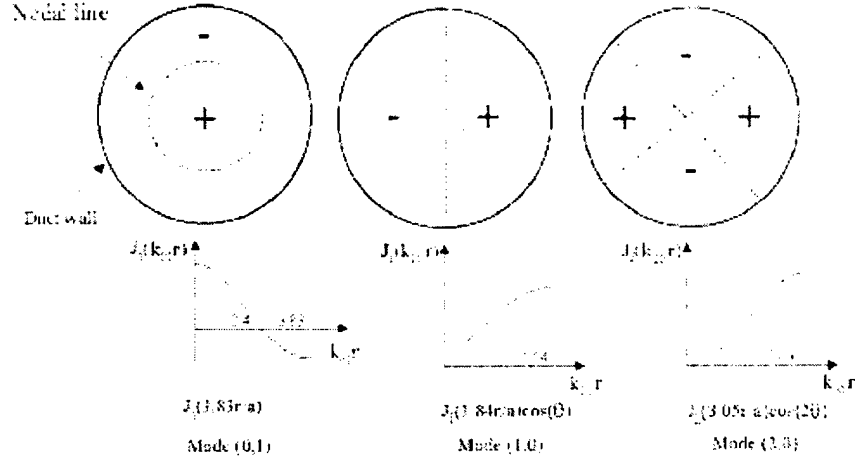
Figure 3.3: The mode shapes for the modes (0,1), (1,0), (2,0).

modes at the speeds related to the rotor speed, i.e, Eqn. (3.8) should be changed to:

$$\Theta(\theta) = cos(m\theta - 2\pi n N_B \Omega t/60 + \phi_{m\mu})$$ (3.12)

where $\phi_{,n\mu}$ is the constant initial phase of mode (m, μ). It is convenient here to calculate the mode angular velocity if the above equation is re-written as:

$$\Theta(\theta) = cos\left[m(\theta - \frac{2\pi n N_B \Omega}{60m}t) + \phi_{m\mu}\right]$$ (3.13)

The mode angular velocity is determined to be:

$$\Omega_{m\mu} = \frac{2\pi n N_B \Omega}{60m}$$ (3.14)

It indicates that the mode angular velocity depends on the circumferential order m, harmonic index n and rotating speed of rotor Ω, and it is independent of the radial

mode order μ. Hence, the acoustic modes with a same m but different harmonic order n spin at different velocities. It is also noted that the spinning modes usually rotate at a different velocity compared to the blade passing speed or its harmonic speed which is $2\pi n N_B \Omega / 60$ at the frequency of $n f_{BPF}$. In addition, positive value of m denotes the mode spins in the rotor rotating direction, i.e. positive θ-direction while a negative value of m means the mode spins in the rotor counter-rotating direction, i.e. negative θ-direction.

Based on Eqn. (3.12) and Eqn. (3.9), the complete description of the acoustic pressure at $n f_{BPF}$ in the hard-walled inlet of turbofan engines becomes:

$$p(z, r, \theta, t) = \sum_{m=0}^{M_c} \sum_{\mu=0}^{M_r} A_{m\mu} cos(m\theta - 2\pi n N_B \Omega t / 60 + \phi_{m\mu}) \cdot$$
$$\left[J_m(k_{m\mu} r) - \frac{J'_{n_c}(k_{m\mu} a)}{Y'_{i}(k_{m\mu} a)} Y_m(k_{m\mu} r) \right] e^{-ik_{z,m\mu} z} e^{i2\pi n f_{BPF} t} \tag{3.15}$$

The second discovery they made is that the circumferential mode number m in Eqn. (3.15) is governed by:

$$m = n N_B + qS \tag{3.16}$$

where, q is an integer index $\pm 1, \pm 2, \pm 3, \cdots$ and S is the number of upstream or downstream stator vanes. Thus, the number of rotor blades along with the number of stator

vanes determines the circumferential order of the modes present in the inlet.

3.2.2   Propagation

After the acoustic mode is generated, we need to address whether or not the mode can propagate down the inlet duct. As evident in Eqn. (3.15), the propagation of the modes depends on the axial wavenumber $k_{z,m\mu}$. If $k_{z,m\mu}$ is a real number, the term $e^{-ik_{z,m\mu}z}$ in Eqn. (3.15) is periodic with respective to z so that it represents a propagating mode, i.e., the mode is said to be cut-on. On the other hand, if $k_{z,mu}$ is imaginary and negative, the term $e^{-ik_{z,m\mu}z}$ results in an exponentially decaying mode, i.e., the mode is said to be cut-off. It is noted that the above criteria holds for both the stationary and spinning modes since $\Theta(\theta)$ (see Eqn. (3.8) for stationary modes, and Eqn. (3.12) for spinning modes) does not play a role in the exponential term in Eqn. (3.15).

To find the axial wavenumber $k_{z,m\mu}$, Eqn. (3.2) is written in cylindrical coordinate and assuming harmonic motion results in:

$$\frac{\partial^2 p}{\partial r^2} + \frac{1}{r}\frac{\partial p}{\partial r} + \frac{1}{r^2}\frac{\partial^2 p}{\partial \theta^2} + \frac{\partial^2 p}{\partial z^2} = -k_0^2 + 2ik_0 M \frac{\partial p}{\partial z} + M^2 \frac{\partial^2 p}{\partial z^2} \tag{3.17}$$

where k_0 is the free space wavenumber as given by $k_0 = 2\pi f_0/c$ and f_0 is the excitation frequency which is either BPF or its harmonics in this case.

Substituting Eqn. (3.9) or (3.15) into Eqn. (3.17) gives:

$$k_{m\mu}^2 = k_0^2 - k_{z,m\mu}^2(1 - M^2) - 2k_0 k_{z,m\mu} M \qquad (3.18)$$

Eqn. (3.18) allows to solve for the value of the wavenumber $k_{z,m\mu}$. The two roots are found to be:

$$k_{z,m\mu}^+ = \left[-M k_0 + \sqrt{k_0^2 - k_{m\mu}^2(1 - M^2)} \right] / (1 - M^2) \qquad (3.19)$$

$$k_{z,m\mu}^- = \left[-M k_0 - \sqrt{k_0^2 - k_{m\mu}^2(1 - M^2)} \right] / (1 - M^2) \qquad (3.20)$$

where $k_{z,m\mu}^+$ and $k_{z,m\mu}^-$ represent positive and negative traveling or decaying waves, respectively.

From equations (3.19) and (3.20), there are three conditions that define the propagation characteristic. Focusing only on the modes in the positive z-direction (i.e., Eqn. (3.19)), they are:

(a) If $k_0 > k_{m\mu}\sqrt{1 - M^2}$, $k_{z,m\mu}^-$ is a real number and the mode will propagate with a wavenumber of

$$k_{z,m\mu}^+ = \left[-M k_0 + \sqrt{k_0^2 - k_{m\mu}^2(1 - M^2)} \right] / (1 - M^2) \qquad (3.21)$$

(b) If $k_0 < k_{m\mu}\sqrt{1-M^2}$, $k_{z,m\mu}^+$ is complex with negative imaginary component and the mode will exponentially decay with a wavenumber of

$$k_{z,m\mu}^+ = \left[-Mk_0 - i\sqrt{k_{m\mu}^2(1-M^2) - k_0^2}\,\right]/(1-M^2) \qquad (3.22)$$

(c) $k_0 = k_{m\mu}\sqrt{1-M^2}$ defines the transition between the previous two cases. This condition is used to define the mode cut-on frequency $f_{m\mu}^{cut-on}$ as:

$$f_{m\mu}^{cut-on} = \frac{k_{m\mu}c}{2\pi}\sqrt{1-M^2} \qquad (3.23)$$

Therefore, an acoustic mode can propagate if its excited frequency is greater than $f_{m\mu}^{cut-on}$ while it decays otherwise.

In addition, it is also noted that the mode axial propagation velocity or mode phase velocity $c_{z,m\mu}$, and wavelength $\lambda_{z,m\mu}$ are greater than those, i.e. c and $\lambda = c/f_0$ in the free field. They are

$$c_{z,m\mu} = \frac{c}{\sqrt{1-(f_{m\mu}/f_0)^2}} \qquad (3.24)$$

$$\lambda_{z,m\mu} = \frac{\lambda}{\sqrt{1-(f_{m\mu}/f_0)^2}} \qquad (3.25)$$

respectively. Eqn. (3.24) and Eqn. (3.25) indicate that the mode axial phase velocity and mode axial wavelength vary from mode to mode.

3.2.3   Acoustic Mode Analysis of Simulator

Based on the physical configuration of the simulator, the excited acoustic modes in the inlet can be found. In addition, the cut-on mode frequencies can be calculated; and hence, the propagating characteristic of the modes in the inlet can be determined. Two simulator speeds of 30,000 and 40,000 rpm are considered (the simulator is operated from 20,000 rpm and 40,000 rpm in this research). The corresponding BPF and 2BPF at 30,000 rpm are 9 kHz and 18 kHz, respectively while they are 12 kHz and 24 kHz, respectively at 40,000 rpm according to Eqn. (3.1).

The simulator is equipped with 4 upstream IGVs, 18 rotor blades and 26 downstream EGVs. Both IGV-rotor and rotor-EGV interactions result in the generation of discrete tones. Using Eqn. (3.16), the circumferential modes excited by IGV-rotor interaction are listed in Table 3.2. The modes excited by by rotor-EGV interaction are presented in Table 3.3. Note in Eqn. (3.16), the integer index q can range from $-\infty$ to ∞. Only a limited range of q is used in both of the tables and thus only a few circumferential modes are computed. As indicated by Table 3.2, the mode order generated by IGV-rotor interaction increases by an interval of 4. On the other hand, the mode order generated by rotor-EGV interaction increases by an interval of 26. Note that these two

Table 3.2: The circumferential order of some acoustic modes excited by IGV-rotor interaction in the simulator inlet.

BPF (n=1)		2BPF (n=2)		3BPF (n=3)	
q	$m = 18 + 4q$	q	$m = 36 + 4q$	q	$m = 54 + 4q$
-7	-10	-12	-12	-16	-10
-6	-6	-11	-8	-15	-6
-5	-2	-10	-4	-14	-2
-4	2	-9	0	-13	2
-3	6	-8	4	-12	6
-2	10	-7	8	-11	10
-1	14	-6	12	-10	14

Table 3.3: The circumferential order of some acoustic modes excited by rotor-EGV interaction in the simulator inlet.

BPF (n=1)		2BPF (n=2)		3BPF (n=3)	
q	$m = 18 + 26q$	q	$m = 36 + 26q$	q	$m = 54 + 26q$
-2	-34	-2	-16	-3	-24
-1	-8	-1	10	-2	2
0	18	0	36	-1	28
1	44	1	62	0	54
2	70	2	88	1	80

tables only provide information on the circumferential order of the acoustic modes. As stated before, a specific m consists of a sequence of radial order, denoted by μ.

The calculation of the mode cut-on frequency, $f_{m\mu}^{cut-on}$ can be carried out according to Eqn. (3.23) where $k_{m\mu}$ can be found by solving Eqn. (3.6). The outer radius of $a = 2.05$ *inches*, the hub-to-tip ratio of $b/a = 0.439$, the sound speed at 25^oC of $c = 346.6$ *meter/second*, and the estimated Mach number of 0.3 at 30,000 rpm and 0.35 at 40,000 rpm are used in the calculation. The results are listed in the tables 3.4 and 3.5 for the two simulator speeds. As can be seen, the cut-on frequency increases with the circumferential order m of the acoustic modes with same radial order μ. Similarly for the acoustic modes with same circumferential order, the cut-on frequency increases with μ. Therefore, the relative smaller cut-on frequencies are positioned in the upperleft corner of the tables.

Based on Table 3.4 and Table 3.5 and the wave propagation criteria discussed in section 3.2.2 the propagating acoustic modes in the simulator inlet duct can be determined. Table 3.6 lists the propagating acoustic modes at BPF and 2BPF from both IGV-rotor and rotor-EGV interactions when the simulator runs at 30,000 rpm and 40,000 rpm. Note that in the table, $(2, 0 - 2)$ means the range of modes $(2,0)$ through $(2,2)$. For example, the modes (2,0) and (2,1) are present in the inlet at 30,000 rpm, i.e.,

Table 3.4: The mode cut-on frequencies at the speed of 30,000 rpm (M=0.3) [Hz].

$\mu \setminus m$	0	±2	±4	±6	±8	±10	±12
0	0	2,811	5,308	7, 570	9.748	11,896	14.026
1	5,796	6,673	8.874	11,552	14,157	16.594	18.938
2	11,394	11,818	13.046	14,984	17,461	20,147	22.756
3	17,029	17,307	18.126	19,450	21,244	23,480	26.054
4	22,676	22,883	23,498	24,501	25,868	27,582	29.639

Table 3.5: The mode cut-on frequencies at the speed of 40,000 rpm (M=0.35) [Hz].

$\mu \setminus m$	0	±2	±4	±6	±8	±10	±12
0	0	2,761	5,212	7,433	9,573	11,681	13,773
1	5,692	6,553	8,715	11,344	13,902	16,295	18,596
2	11,189	11,605	12,811	14,714	17,146	19,784	22,346
3	16,722	16,995	17,799	19,099	20,861	23,057	25,585
4	22,267	22,471	23,075	24,059	25,402	27,085	29,105

Table 3.6: The propagating modes at BPF and 2BPF.

Speed	IGV - rotor Interaction		rotor - EGV Interaction	
	BPF (9 kHz)	2BPF (18 kHz)	BPF (9 kHz)	2BPF (18 kHz)
30,000 rpm	$(\pm 2, 0 - 1)$	$(0, 0 - 3)$	none	$(10, 0 - 1)$
	$(\pm 6, 0)$	$(\pm 4, 0 - 2)$		
(M=0.3)		$(\pm 8, 0 - 2)$		
		$(\pm 12, 0)$		
	BPF (12 kHz)	2BPF (24 kHz)	BPF (12 kHz)	2BPF (24 kHz)
40,000 rpm	$(\pm 2, 0 - 2)$	$(0, 0 - 4)$	$(-8, 0)$	$(10, 0 - 3)$
	$(\pm 6, 0 - 1)$	$(\pm 4, 0 - 4)$		
(M=0.35)	$(\pm 10, 0)$	$(\pm 8, 0 - 3)$		
		$(\pm 12, 0 - 2)$		

they are cut-on, because the circumferential order $m = 2$ is excited by the IGV-rotor interaction according to Table 3.2. In addition, the BPF of 9,000 Hz at 30,000 rpm is greater than the cut-on frequencies of modes (2,0) and (2,1), (2,811 Hz and 6,673 Hz, respectively) as seen from Table 3.4. However, mode (2.2) cannot propagate since its cut-on frequency (i.e., 11,818 Hz) exceeds the BPF (i.e., 9,000 Hz).

It should be noted that the magnitude of the acoustic modes listed in the table depends on the distribution of loading on the blades. It implies that some of the modes will

dominate the inlet sound field while the other modes may contribute insignificantly.

As found from the table, the number of the propagating modes at BPF is limited although IGV-rotor and rotor-EGV interaction excite an infinite set of the circumferential order m. This is because most of the excited modes, especially the modes due to rotor-EGV interaction, are cut-off. In addition, more modes are cut-on at 40,000 rpm as compared to those at 30,000 rpm since the corresponding BPF at 40,000 rpm is higher than that at 30,000 rpm. For the same reason, the sound field at 2BPF contains much more modes than that at BPF.

Figure 3.4 shows several propagating mode shapes. The solid circle denotes the inlet centerbody which has a radius of 0.9 inches. As compared to Figure 3.3, the acoustic modes here are spinning. A positive value for m defines the mode spins in the same direction as the rotor while a negative value is for the opposite direction. Since mode (0,1) has no variation in θ-direction, there is no spinning direction shown in the figure.
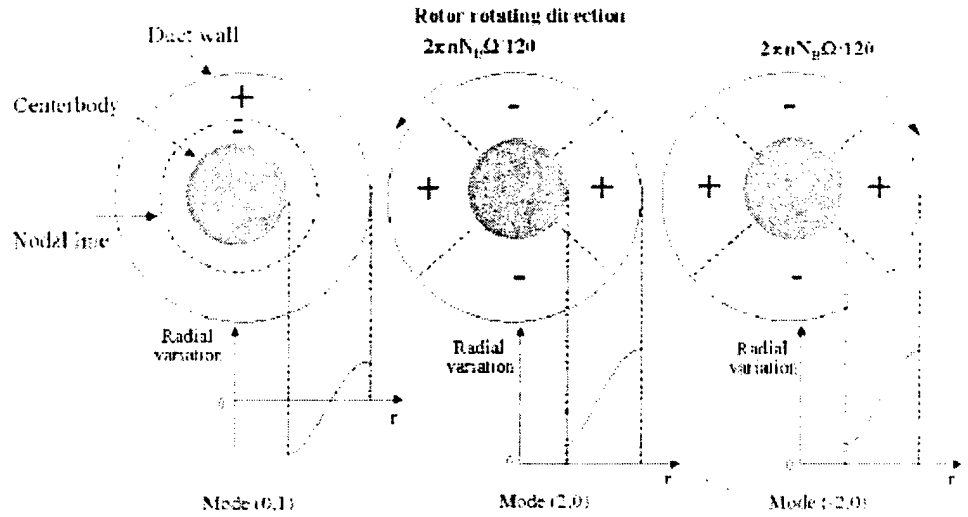
Figure 3.4: The mode shapes of the spinning modes (0,1), (-2,0) and (2,0).

3.2.4 Radiation

When the propagating acoustic modes reach the opening of the inlet, they will radiate into the far field. It is interesting to investigate the directional distribution of the propagating modes. However, the radiation process is complicated due to the diffraction effects and the acoustic impedance change at the inlet opening. The first work on the sound radiation from an unflanged cylindrical duct may be from Levine and Schwinger[51] and Weinstein[52] using Wiener-Hopf technique. Later work included Homicz and Lordi[53] and Lansing[54]. The earlier work of Levine and Schwinger fo-

cused on non-spinning modes. Later work by Homicz and Lordi included the directivity plot for spinning modes. According to their work, each mode will produce a radiation pattern in the far field. The sound pressure level directivity is then a composite of all the acoustic mode. The location of the principal lobe for the mode (m, μ) in a circular duct with a radius of a can be predicted as [53]:

$$\Psi_p = cos^{-1} \left(\sqrt{1 - M^2} \sqrt{\frac{1 - (\frac{k_{m\mu}\sqrt{1-M^2}}{k_0 a})^2}{1 - M^2[1 - (\frac{k_{m\mu}\sqrt{1-M^2}}{k_0 a})^2]}} \right) \tag{3.26}$$

where Ψ_p is the angle of the principal lobe of the radiation directivity of the acoustic mode measured from the inlet axis. Equation 3.26 is applicable for aircraft engine inlets with a hub to tip ratio of less than 0.5.

3.3 Summary

The basics of fan noise theory were reviewed in this Chapter. Some important concepts such as spinning acoustic mode, mode spinning speed, axial mode phase velocity and wavelength were introduced. Propagation criteria in the duct with flow was described. The cut-on frequencies for the small scale simulator using a concentrical duct model were calculated. The propagation modes at BPF and 2BPF for the simulator running at the speeds of 30,000 and 40,000 rpm were tabulated. These knowledge is neces-

sary when we design and implement TEB control systems using the acoustic sensing

approaches described in the Chapter 5.

Chapter 4

A Pitot-probe Based Flow Control

System

This chapter describes a TEB control system with Pitot probes as wake sensors on the small scale turbofan engine simulator. As mentioned early in Chapter 1, one of the research objectives in the dissertation is to investigate the feasibility of implementing active flow control systems in a realistic environment. Though the Pitot probe in this chapter is an intrusive flow sensor which are not probably practical in realistic

situations of turbofan engines, it is appropriate as a preliminary step toward a more

in depth investigation of advanced wake sensing approaches. In addition, an upper

performance limit in terms of wake-filling can be obtained since the Pitot probes provide

the direct measurement of the wake which is sought to be minimized. Consequently,

the probe-based control system developed in this chapter can serve as the baseline case

in evaluating the performance of other control systems with indirect wake sensors.

In this chapter, the working principle of Pitot static probes is first described. The

experimental setup in the anechoic chamber follows and the configuration of the con-

trol system is then presented. The wake-filling performance in terms of aerodynamic

and acoustic measurements are investigated. Finally, the main conclusions are then

discussed.

4.1   Experimental setup in the simulator

The sensing approach used in this part is simple Pitot-Static probes to measure the

total pressure in the wakes behind each IGV as illustrated in Figure 4.1. The probe

has a head diameter of 1/16" with a sensing hole of diameter 1/32" and length of 0.5".

These probes are insensitive to incidence angle variations of 5°. Four threaded holes are provided in the inlet for mounting the four flow sensors. The holes are positioned such that each probe measures the maximum total pressure defect in a wake. The inlet flow field is found to be radially uniform, and hence the use of a single flow sensor for each wake is adequate. This will be further described in the next section. These wake probes are placed $0.5 \, C_s$ downstream of the IGV where C_s represents the IGV chord. This spacing is determined based on a bench test result which shows that a distance of $0.5 \, Cs$ is required to allow the jet to mix into the wake. Measurements made closer to the IGV will sense the potential core of the jet issuing out of the blowing hole rather than the mixed out flow, and hence could generate an erroneous wake signal.
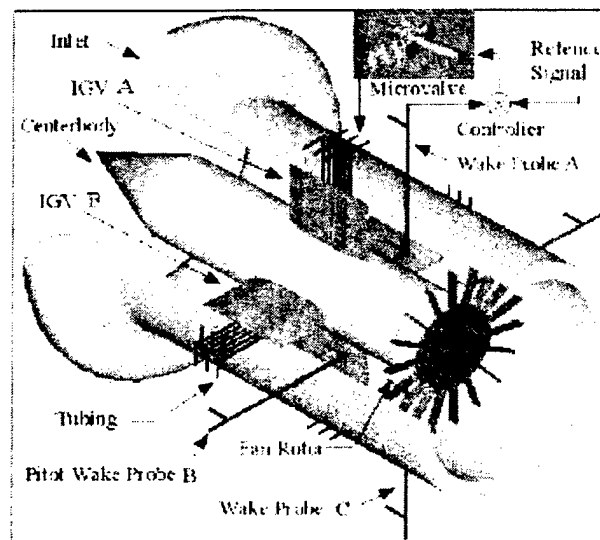
Figure 4.1: The Pitot-probe-based experimental setup.

Another probe is placed in the free stream to measure the free stream total pressure (not shown in Figure 4.1). The difference between the output of the wake and free stream probes forms the error signal for a traditional feedback PID controller (proportional-integral-derivative), which is to be introduced in a later section. Basically, this algorithm aims to minimizing the error signal. Therefore, the wake is going to be filled up to the free stream when the controller has converged. The blowing rate is adjusted by the MEMS-based microvalves according to the control signal from the controller.

4.2   Working principle of the Pitot-static probe

In order to employ Pitot-static probes as flow sensors, grasp of some basic fluid knowledge is needed. Therefore, it is appropriate to introduce a simple review of fluid dynamics. The famous Bernoulli's equation is to be first introduced. The working principle of the velocity measurement device, Pitot-static probe is then described.

Bernoulli's equation can be derived from the first law of thermodynamics (conservation

of energy) to give:

$$\frac{1}{2}\rho V^2 + P = P_0 \tag{4.1}$$

where P_0 is usually called total pressure which remains constant streamwise. ρ is the fluid density, P is pressure and V denotes flow velocity. The term $\frac{1}{2}\rho V^2$ is referred as dynamic pressure while P is called static pressure.

It is important to review the assumptions in Bernoulli's equation. First, the steady flow assumption means that the relationship cannot be applied to a flow which has time dependent properties or behavior. There will be some exceptions to this when flow changes are slow enough to consider the flow "quasi-steady". Secondly, incompressible flow was assumed meaning that density was assumed constant throughout the flow. For most problems encountered in aerodynamics, the incompressibility assumption can be used for flow velocity of up to about 0.65 Mach number. Thirdly, flow along a streamline was assumed. Thus, P_0 may be considered constant throughout the entire flow if it is known that all streamlines emanated from a common source such as a uniform flow. If the flow is known to have a velocity or pressure gradient, Bernoulli's equation must be used with care and only applied along streamlines. Finally, negligible buoyancy was assumed in the equation. The buoyancy term $\rho g z$ is always negligible when Eqn. (4.1) is used in air where z denotes the altitude from sea level and g is the

acceleration of gravity.

In the simulator setup for the speed range of 20,000 to 40,000 rpm. all the above assumptions are satisfied. The axial Mach number of steady flow in the inlet duct for this speed range is only around 0.3. The changes in simulator speed and thus flow conditions can also be considered "quasi-steady". Finally, the total pressure P_0 is constant and equal to the atmospheric pressure, i.e., 10,1000 Pa or 14.3 Psi. because the simulator is drawing ambient stationary air into the inlet. An schematic of stream lines for the simulator case is shown in Figure 4.2.
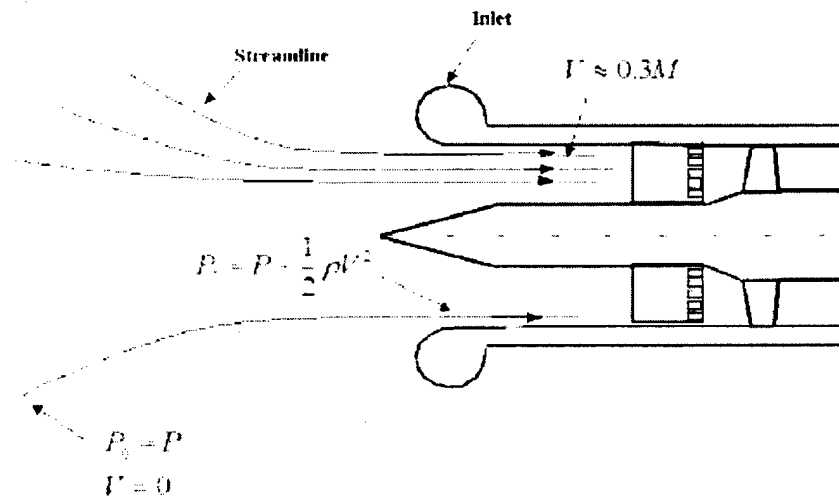
Figure 4.2: Example of streamline in the simulator when Bernoulli's equation is applied.

Bernoulli's equation provides an easy method for determining the speed of a fluid flow. Rearranging the equation, the flow velocity is given as:

$$V = \sqrt{\frac{2(P_0 - P)}{\rho}} \qquad (4.2)$$

The total pressure P_0 in a flow is easy to measure if the flow direction is known. One needs only place a simple, open ended tube in the flow such that the tube is aligned with the local flow direction and the open end of the tube is pointing upstream. The flow then stagnates or comes to rest at the tube's open end, giving a local pressure equal to the total pressure. The tube can then be connected to any pressure sensors to allow a determination of that pressure as shown in Figure 4.3(a). This type of tube is called a Pitot probe. The static pressure P is equally easy to measure using another type of tube with a closed end and pressure "taps" or openings around its circumference. This tube must also be aligned with the flow direction. When connected to a sensor, the flow's static pressure will be indicated. It should be noted that for a static probe to obtain good readings the upstream end should be properly shaped to avoid flow separation and pressure taps placed far enough from the end to avoid errors that might be produced by the local acceleration of the flow over the front of the probe. The static probe is shown in Figure 4.3(b). A Pitot-static probe, as shown in Figure 4.3(c), is simply a static tube wrapped around a Pitot probe.
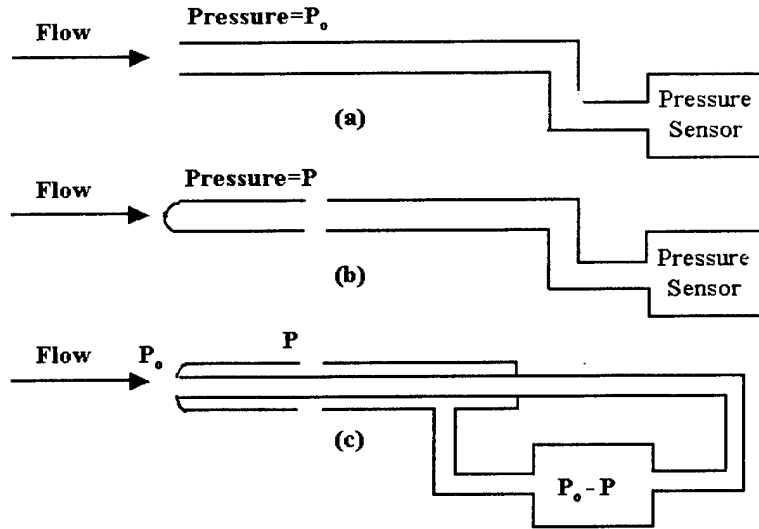
Figure 4.3: The operation of (a) Pitot probe, (b) Static probe, and (c) Pitot-static probe.

The Pitot probes are used in the experiments which are shown in Figure 4.4. One probe is placed in the free stream while another probe is in the wake. Therefore, the total pressure measured in the free stream probe is

$$P_{0,f} = P_f + \frac{1}{2}\rho V_f^2 \qquad (4.3)$$

where P_f is the free stream static pressure and V_f is the free stream velocity. On the other hand, the total pressure in the wake is measured as

$$P_{0,w} = P_w + \frac{1}{2}\rho V_w^2 \qquad (4.4)$$

where P_w is the wake static pressure and V_w is the wake flow velocity. As described in

Chapter 1, the velocity V_w is less than V_f due to the viscous effect as flow passes the surface of IGV. However, the static pressure in the wake is the same as that in the free stream, i.e., $P_w = P_f$ since streamline flow field is assumed in the inlet [55]. Therefore, The wake total pressure $P_{0,w}$ is less than the free stream total $P_{0,f}$ because of the losses in the flow velocity. The difference between these two total pressures is used as the error signal for the control system, which will be described in the following section.

IGV

Streamline

Pitot probe in the wake

$$P_{0,w} = P_w + \frac{1}{2}\rho V_w^2$$

Pitot probe in Free stream

$$P_{0,f} = P_f + \frac{1}{2}\rho V_f^2$$
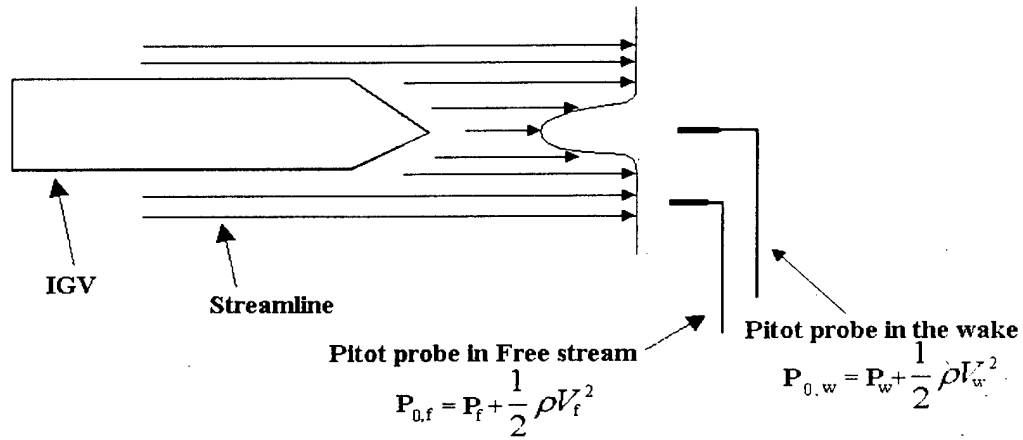
Figure 4.4: The use of Pitot probes in the experiments.

The error signal $P_{0,f} - P_{0,w}$ is minimized in the control system by using trailing edge blowing technique adding mass flow into the wake, thus augmenting the wake flow

velocity. Especially as the digital controller converges, the error signal will vanish. i.e., the total pressure of the wake with TEB, $P_{0,w}^{TEB}$ will be equal to $P_{0,f}$. That is

$$P_{0,w}^{TEB} = P_{0,f} \qquad (4.5)$$

Note that $P_{0,w}^{TEB}$ is defined as:

$$P_{0,w}^{TEB} = P_w + \frac{1}{2}\rho V_{w,TEB}^{2} \qquad (4.6)$$

It is apparent from Eqn. (4.6) and Eqn. (4.3) that the augmented wake flow velocity $V_{w,TEB}$ will be equal to the free stream velocity V_f. In consequence, complete wake re-energizing is achieved.

4.3   Proportional integral derivative feedback controller

The control scheme selected for this application is the feedback PID algorithm [56, 57]. Figure 4.5 shows a schematic of a PID controller in a typical feedback control block diagram which includes the plant, the sensor, and the reference input $r(t)$. The error signal $e(t)$ is defined as the difference between the reference signal $r(t)$ and the sensor

output. The output of the PID controller is usually called control signal $u(t)$ which drives the plant.
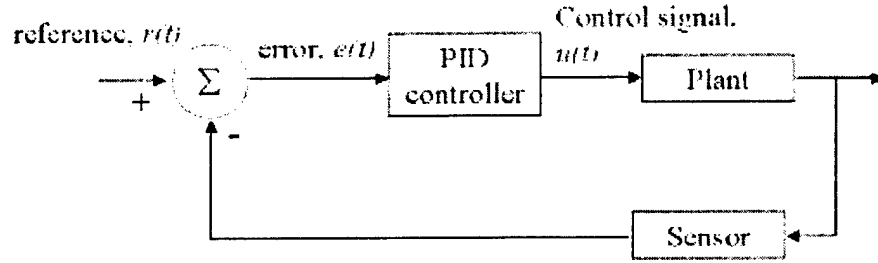
Figure 4.5: A typical feedback control system.

Feedback PID controllers are widely used in the process control industries. The control output $u(t)$ of a PID controller consists of the weighted contribution of three terms. These three control signal components are proportional to the error signal $e(t)$ and its integral and derivative as:

$$u(t) = k_p e(t) + k_i \int_0^t e(t)d\eta + k_d \frac{de(t)}{dt} \qquad (4.7)$$

where t denotes time; k_p, k_i and k_d represent the proportional, integral and derivative gains, respectively. Proportional control can lead to reduced errors to disturbance but it results in small steady-state errors. It can also increase the speed of response but typically at the cost of a larger transient overshoot. If the controller also includes a

term proportional to the integral of the error, the steady-state error can be eliminated. However, there tends to be a further deterioration of the dynamic response called windup that requires a long period of time after the error changes its sign to bring the system back to normal. This is the result of the integral term becoming extremely large, thus requiring a large number of samples (of opposite sign) to reduce the magnitude of the integral term. Finally, addition of a term proportional to the error derivative can add damping to the dynamic response to improve stability. A disadvantage of the derivative term is that it can amplify the high-frequency noise in the system. In practice, values of the PID parameters are mainly determined empirically. These three terms combined form the classical PID controller. Therefore, design of a PID controller involves the determination of the three gains. Figure 4.6a shows the structure of the analog PID controller while Figure 4.6b illustrates it in the s-domain obtained by the Laplace transform. The s domain expression for Eqn. (4.7) is given as:

$$U(s) = \left(k_p + \frac{k_I}{s} + k_d s \right) E(s) \tag{4.8}$$

where $U(s)$ and $E(s)$ represent in the s-domain the signals in the time domain, $u(t)$ and $e(t)$, respectively.

In recent years, digital signal processors (DSP) are usually used to implement PID controllers since DSPs become more affordable. This requires that the analog propor-
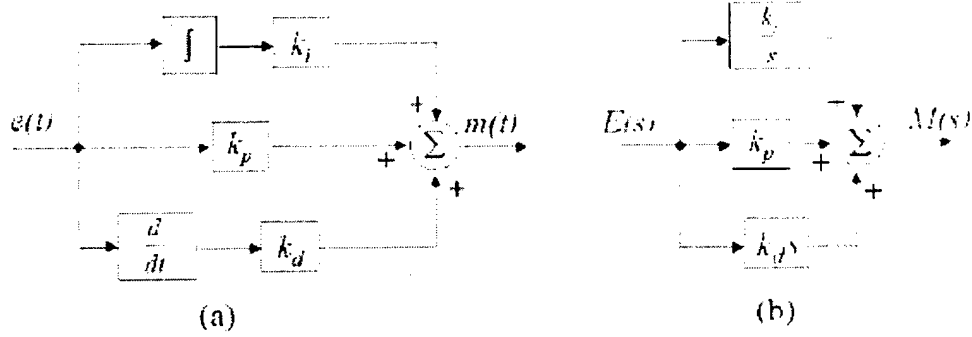
Figure 4.6: Block diagram of analog PID controller in (a) time domain and (b) s-domain froms.

tional, integral and differential terms in Eqn. (4.7) be approximated numerically in a discrete system. If the numerical approximation is performed accurately, there is little difference in the system response from the analog implementation. The Euler approximation method, or the right-side rectangular rule, which is the simplest widely used approach, results in the controller difference equation [57]:

$$u(k+1) = k_p e(k+1) + k_i u_I(k+1) + \frac{k_d[e(k+1) - e(k)]}{T} \qquad (4.9)$$

where k is the time index. i.e., t_k; T is the sampling period; and $u_I(k+1)$ is given by:

$$u_I(k+1) = u_I(k) + Te(k+1) \qquad (4.10)$$

Alike the analog PID algorithm which has the expression in the s-domain, the digital PID controller can be expressed in the discrete z-domain through the z-transform of

Eqn. (4.9). The z-domain expression is useful in the analysis of the control system performance such as stability, response time, etc. It is given as

$$U(z) = \left[k_p + \frac{k_I T z}{z - 1} + \frac{k_d(z - 1)}{Tz} \right] E(z) \tag{4.11}$$
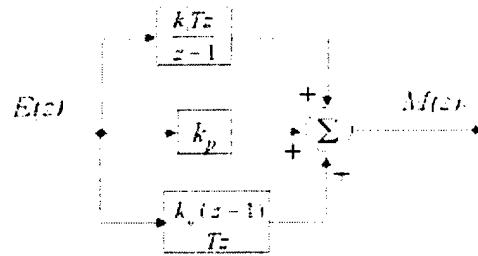
Figure 4.7: Digital PID controller.

A block diagram of the application of the PID controller to the TEB is shown in Figure 4.8. The control loop starts from the two Pitot probes. The pressure sensors are needed to convert the probe total pressures to voltage signals. Differential voltage amplifiers with a gain of 10 are implemented at the output of the pressure sensors (the probe sensitivity is about 20 mVolts/psi). Differential amplification is used since the signal from a Pitot probe sensor needs to be converted to a single ended ground referenced signal. This is necessary, since all other devices in the system are ground referenced.

Low pass filters (LPF) with a cut-off of 10 Hz are used to serve as anti-aliasing filters to remove the high frequency noise. The digital PID algorithm given in Eqn. (4.9) is implemented on a Texas Instrument DSP TMS320C30. The sampling frequency is chosen to be 30 Hz. This is the lowest sampling frequency which can be obtained using the on-board timer. However, this frequency is high enough as compared to the slow response of the mechanical components in the system such as the MEMS based microvalves, blowing air travelling in the tubing and the Pitot probes. Since the output voltage range of the DSP board, i.e., -8.2 — 8.2 volts does not match the operating range of the MEMS based microvalves as shown in Figure 2.10, a voltage offset circuit with 4.5 Volts are used for each microvalve to shift the range of -8.2 — 8.2 volts to -3.7 — 12.7 Volts. In practice, this range are further limited so that it only covers the effective working range of the microvavles, which is 3 — 9 Volts. Since six microvalves are used in the experiments to control independently the six blowing holes in each of the four IGVs, 24 channels of the offset circuits are required.

The blowing air controlled by the microvalves mixes with the flow in the wake which is sensed again by the flow sensor. Therefore, a single-input-single-output (SISO) control loop is formed. In the experiments, all six microvalves connected to a particular IGV are driven by the same SISO controller. Since there are four IGVs in the simulator inlet, four identical SISO PID controllers are required which hence forms a 4I4O controller.
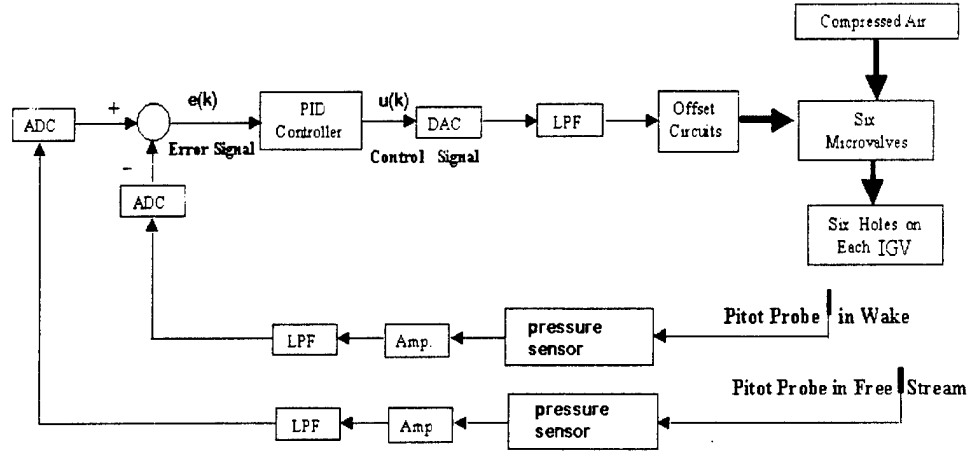
Figure 4.8: Block diagram of the PID controller in anechoic chamber setup.

Before testing the 4I4O controller on the simulator in the anechoic chamber, preliminary tests of the SISO system are conducted in a bench setup. The purpose of the bench tests is to determine the appropriate values for k_p, k_i and k_d of the controller. These values are difficult to predict for two reasons. The first reason is that the exact model for MEMS based microvalve in terms of blowing air total pressure versus control voltage is not available. As discussed in section 2.5.2, the pneumatic microvalve exhibits a nonlinear and time-varying characteristics. The second difficulty lies in that the transfer function from the blowing air total pressure to the total pressure sensed by the flow sensor is also difficult to obtain. This is because jet mixing in the wake is a very complicated process [58]. As in many applications, these three parameters are

selected experimentally [57].
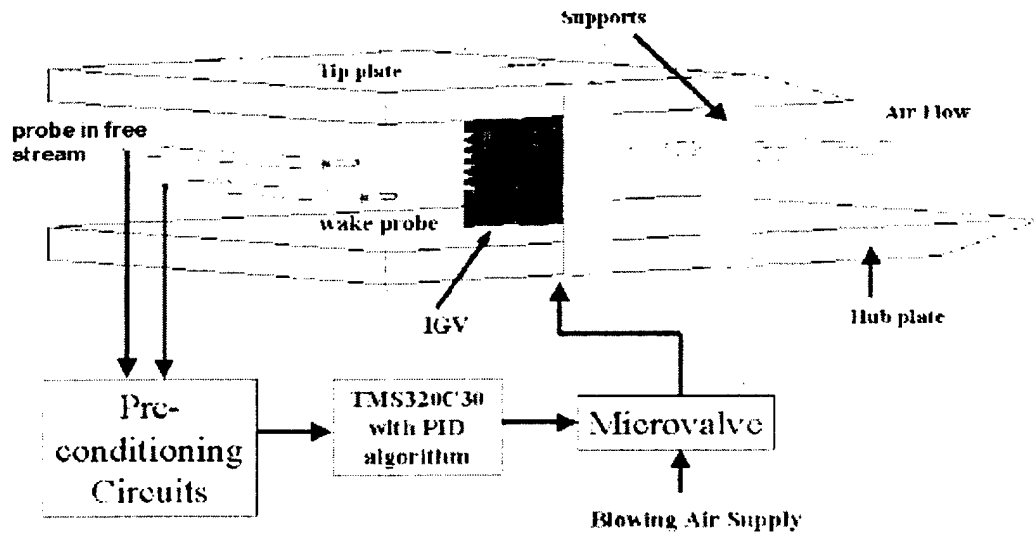
Figure 4.9: Bench setup for PID TEB control.

The bench setup is shown in Figure 4.9. It consists of two parallel Plexiglas plates with

the IGV mounted between the plates. This assembly is completed by side supports

that are fastened onto the plates by bolts. The bench is then mounted on a wooden

test stand, and the assembly is placed at the exit of a 4" × 4" nozzle that is connected

to the discharge of a centrifugal blower. The bench is aligned so that the midspan of

the IGV lines up with the midspan of the nozzle cross section. One Pitot static probe

is placed in the free stream to serve as the reference signal. Another probe is placed

so that its center collinear with the center of a blowing hole. In addition, the probe is

located 0.5 chord downstream IGV so that it measures the fully mixed flow as shown in Figure 2.7. Free stream velocity can be varied by putting a blockage at the inlet of the blower.

Figure 4.10 and Figure 4.11 present the performance of the proportional part of the PID controller, i.e., P controller with a gain of $k_p = 0.6$ and 2, respectively. The free stream flow velocity is changed abruptly to test the step response of the system. The long convergence time is due to the response time of the MEMS based microvalve and the traveling time of blowing air in the tube. The steady state error is nonzero which decreases as k_p increases at the price of the greater control signal variation.

Figure 4.12 and Figure 4.13 demonstrate the system performance when PI controllers are used. With the introduction of the integral term, the steady state error is removed. As k_i increases, the control signal reaches the steady state more quickly, however, usually at the cost of overshooting. The overshoot is not seen in the figures because the pressure of the blowing supply air is not high enough. Similarly, the effect of the derivative term is also tested which however does not cause obvious difference in the system step response since the actuation part has a very long response time.
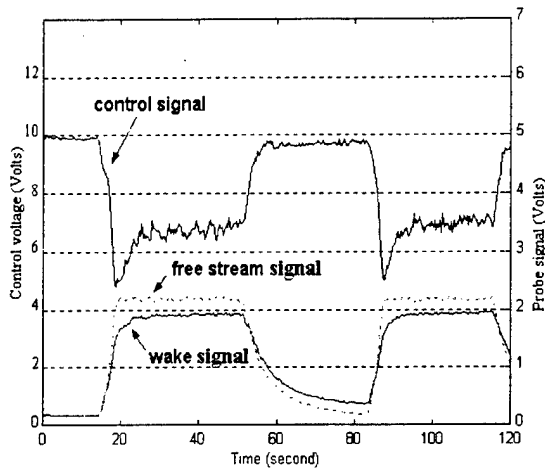
Figure 4.10: PID controller bench test with $k_p = 0.6$, $k_i = 0$, $k_c = 0$.
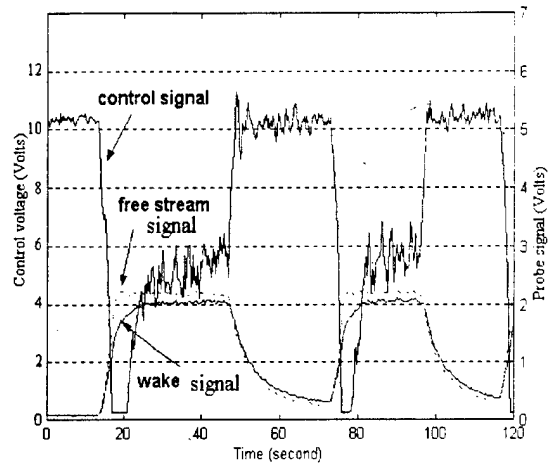
Figure 4.11: PID controller bench test with $k_p = 2$, $k_i = 0$, $k_d = 0$.
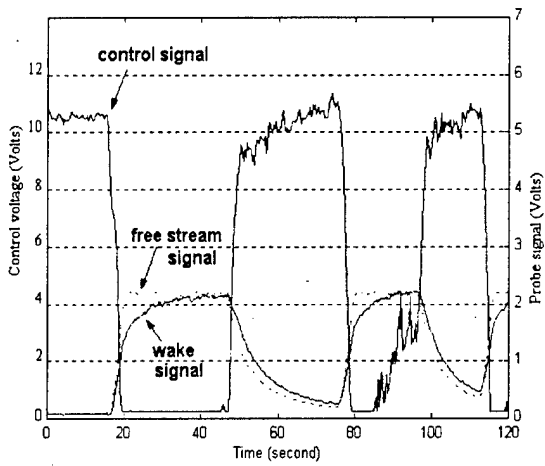
Figure 4.12: PID controller bench test with $k_p = 2$, $k_i = 0.01$, $k_d = 0$.
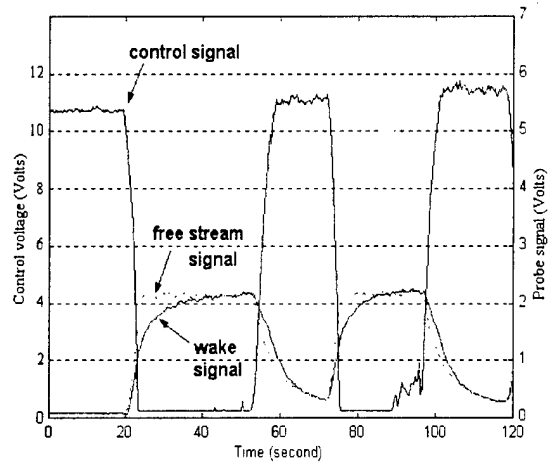
Figure 4.13: PID controller bench test with $k_p = 2$, $k_i = 0.02$, $k_d = 0$.

As a final note, unstability can be caused in the controller system if the gains are not chosen properly. Figure 4.14 shows that the system is at the edge of going unstable for the gains of $k_p = 1.0$, $k_i = 0.2$ and $k_d = 0.0$. As can be seen in the figure, the control signal oscillates with a large amplitude which leads to the oscillation in the wake signal as well. Therefore, such values for gains should be avoided.
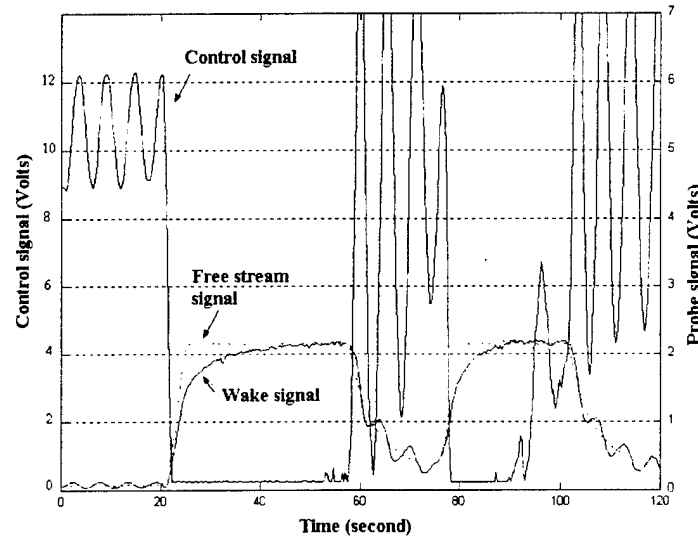
Figure 4.14: PID controller bench test with $k_p = 1$, $k_i = 0.2$, $k_d = 0$.

Through extensive testing on the bench, the gain values in the PID controller of $k_p = 2.0$, $k_p = 0.02$ and $k_d = 0.0$ are selected for the simulator testing in the anechoic chamber to achieve "satisfactory" performance in terms of both transient response and

convergence rate. It is noted that the chamber test uses an 4I4O controller instead of the SISO used in the bench test. Another difference is that the free stream probe in the simulator would always measure a constant as of the ambient pressure according to the Bernoulli's law described in section 4.2, even though the inlet flow Mach number may change with time.

4.4 Active TEB system performance

The active flow control experimental results presented in this section are obtained on the simulator as shown in Figure 4.1, using the PID controller shown in Figure 4.8. As mentioned early, the purpose of the PID feedback controller is to use the error signal to control the microvalves so that, as the flow condition changes in an engine the amount of wake-filling can be optimized by adjusting the microvalves.

The first test performed is to demonstrate the effectiveness of the active control system to adjust to varying flow conditions as the simulator speed is varied. The total pressure of the four wake probes, free stream probe and four control signals are recorded. Figure 4.15 shows the time histories of these signals for IGV A (IGV's A, B, C, D are defined

in Figure 4.1). The lower two traces in this figure are the pressures measured in the free stream and in the wake of IGV A. The difference between these signals is the error signal to be minimized. Figure 4.15 clearly shows that the controller is successful in adaptively driving the microvalves so that the wake and free stream essentially have the same velocity, thus ensuring optimal wake-filling. The dynamics of the controlled system is revealed only if a drastic change in the simulator speed is produced, e.g. speed changes at t=150 and 200 seconds. For example, the simulator speed is decreased from 40,000 rpm down to 20,000 rpm in about 9 seconds at t=150 seconds. From the free stream and wake traces, the control system requires about 12 seconds to optimize the wake filling, i.e. minimize the error signal. Similar behavior is observed at t=200 seconds where the simulator speed is ramped up from 20,000 to 40,000 rpm. These results demonstrate that the active flow control of wakes is feasible under realistic changes in flow conditions.

The total pressure signals of the four wake probes are compared in Figure 4.16 for the time range of 140 – 220 seconds. It indicates that the wake dynamics behave differently when the simulator speed changes at t=150 and 200 seconds. The wake of IGV A shows the largest peak among the four while the wake of IGV C is the smallest. The trace for IGV B has the longest re-convergence time while the one for IGV D has the shortest.
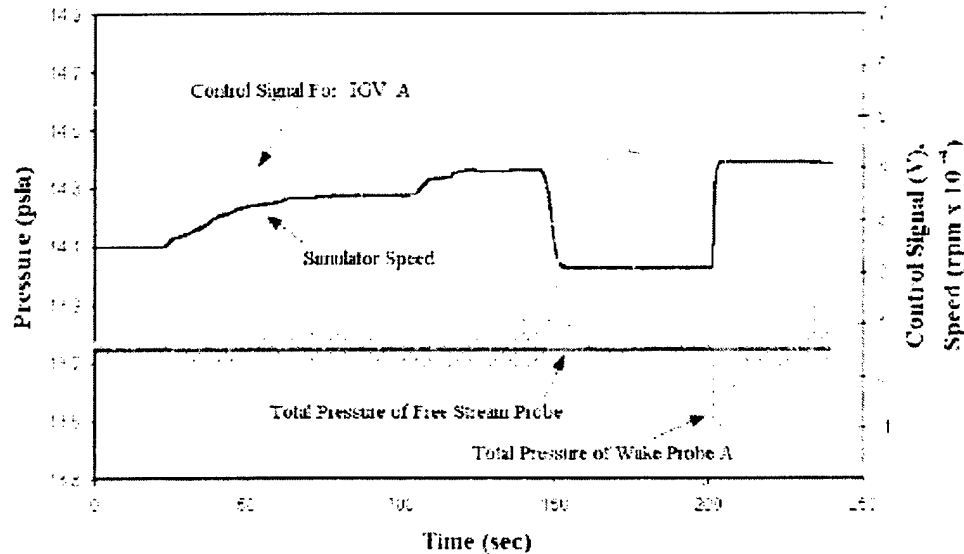
Figure 4.15: The time histories of the signals on IGV A.

The control signals for the four IGVs are illustrated in Figure 4.17. The control signal for IGV A has the largest variation at t=150 seconds which corresponds to the fully open condition in MEMS based microvalves according to the performance curve shown in Figure 2.10. The fully-open condition "holds" there since the system response is fast enough when the simulator speed decreases abruptly, which leads to the largest peak at t=150 seconds in IGV A wake total pressure as seen in Figure 4.16. Similarly, the control signal for IGV C has the smallest variation which corresponds to the smallest peak in the wake total pressure of IGV C. In addition, Figure 4.17 indicates that the control signals for the four IGVs are not identical when the four wakes are completely
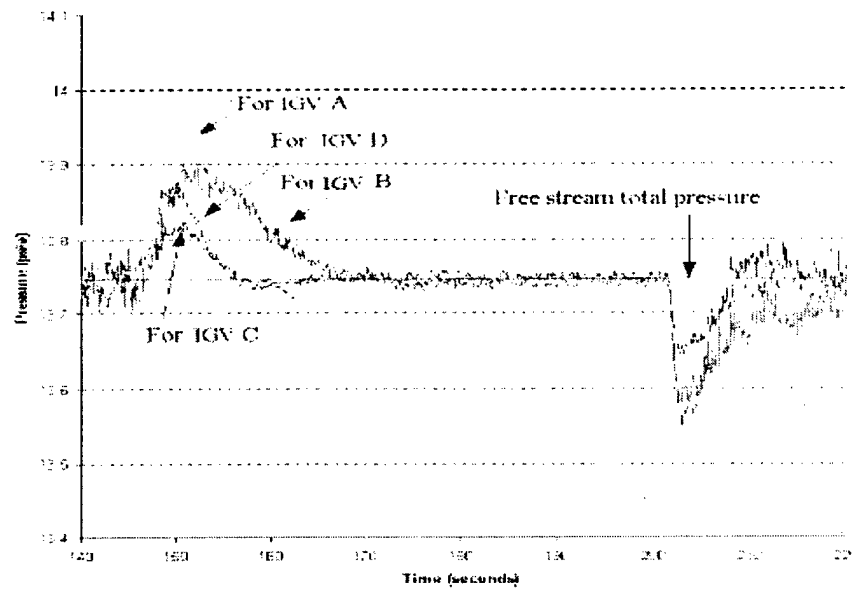
Figure 4.16: The total pressure of the four wake probes.
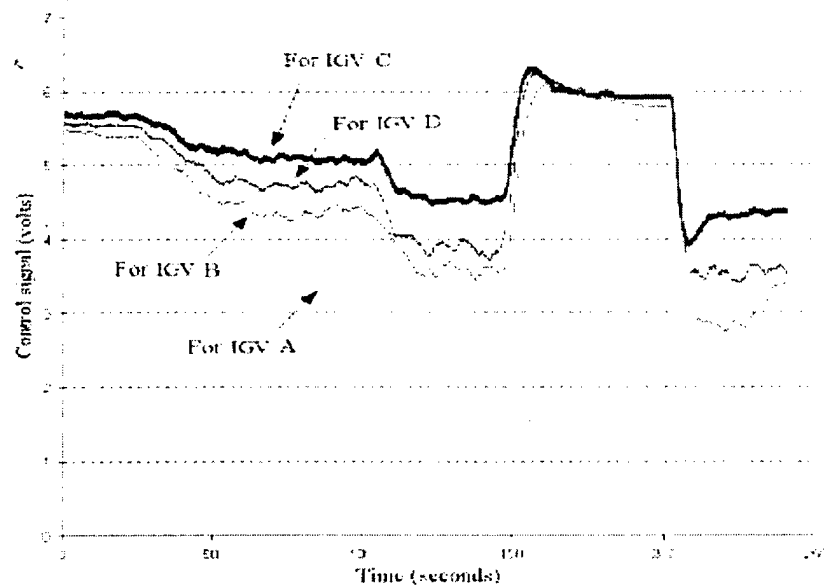
Figure 4.17: The control signals for the four IGVs.

filled.

These variability in the results between IGVs is probably due to the physical geometry in the IGVs and in the response time of the MEMS based microvalves and the Pitot probes. Thus, these results suggest that an independent control system for each IGV could be important to compensate for the variabilities between them.

4.5   Acoustic Results

The successful wake-filling leads to the reduction of the tonal noise components due to the suppression of the interaction of the IGVs and the rotor blades. Thus, the attenuation of the noise at BPF and its harmonics is an indication of the reduction of blade vibration and the HCF damage [1, 3]. Therefore, the sound field with and without TEB is monitored at far-field locations.

The monitored far-field microphone locations are depicted in Figure 4.18. In total, twelve positions are measured in the horizontal plane, from 0° to 110°, every 10°. Since the inlet used is symmetric, the measured directivity holds for corresponding positions

in the vertical plane, and also in the mirrored horizontal plane. The 0° position lines up with the axis of the simulator. Since acoustic data are inherently unsteady due to the unsteady IGV-rotor interaction, the sound pressure level results at each position are obtained by taking an average of 50 spectra.
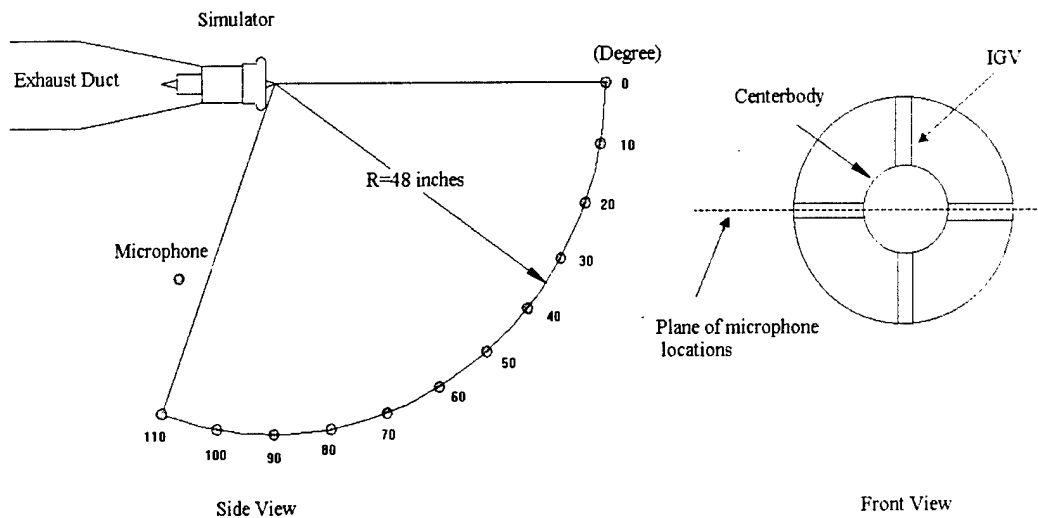
Figure 4.18: Position of far-field monitoring microphones.

Figure 4.19 shows the sample far-field acoustic spectra acquired at the 20° microphone location at a simulator speed of 30,000 rpm. The corresponding BPF tone is at 9,000 Hz. These spectra demonstrate a reduction of about 8.2 dB at the BPF tone and reduction between 6 to 3 dB at the first four harmonics. The wake filling does not lead

to reduction of the broadband noise. This is because the broadband noise is generated by the interaction of random disturbance while the tonal noise is caused by the IGV mean wakes [24]. These tonal noise reductions again clearly indicate the successful wake filling as well as the reduction of the blade forcing function and vibration. It is interesting to point out that the most objectionable noise is from the tones and the tonal reductions are clearly perceived by the human ear.
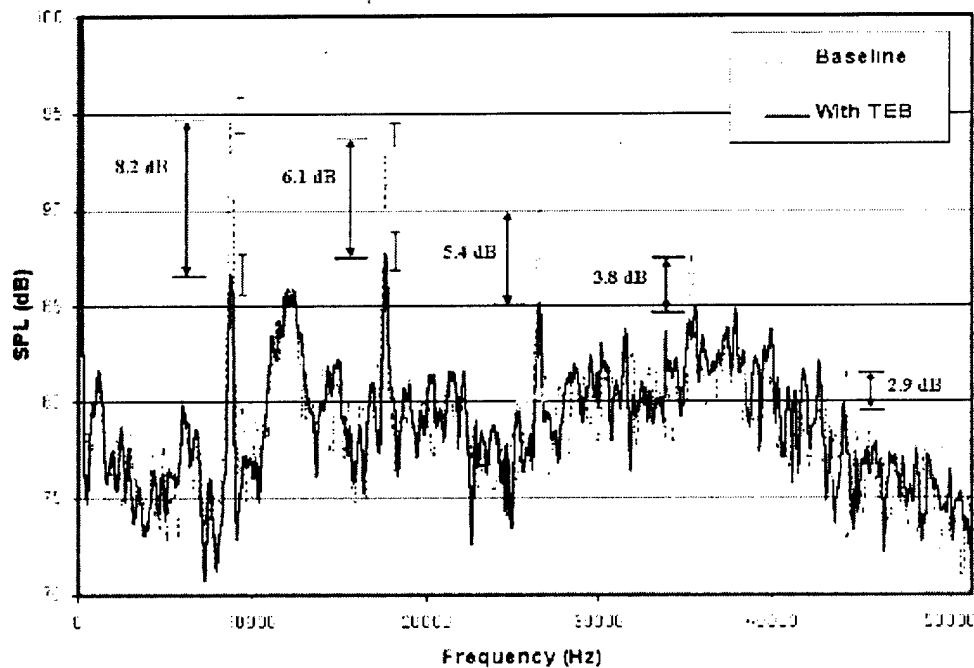
Figure 4.19: Far-field acoustic spectrum at $20°$ with and without active control.

Table 4.1: Confidence interval analysis at 20° ($\bar{\mu}$=mean, τ=standard deviation).

SPL (dB)	BPF tone		2BPF tone	
	Without TEB	With TEB	Without TEB	With TEB
$\mu + 2\tau$	95.6	87.6	94.3	88.4
μ	94.8	86.6	93.7	87.6
$\mu - 2\tau$	94.0	85.5	93.0	86.8

An uncertainty study was performed to determine the confidence in the experimental results. The mean value $\bar{\mu}$ and standard deviation τ for the measurements at the BPF and 2BPF tones were computed without and with active flow control. Using these values, the confidence analysis is presented in Table 4.1 as well as shown in Figure 4.19. It is noted that the confidence level of this range from $\bar{\mu} - 2\tau$ to $\bar{\mu} + 2\tau$ is 94% if the probability density of measurement data follows the Gaussian distribution, which is the case for many engineering applications [59]. Therefore, it can be concluded that the amount of noise reductions at BPF and harmonics is very reliable.

4.5.1 Sound radiation pattern at 30,000 rpm

The radiating directivities are also recorded for the purpose of estimating the sound power level. Figure 4.20 compares the directivity plots at a simulator speed of 30.000 rpm without and with trailing edge blowing. The data presented consists of the sound pressure levels at the blade passing frequency and the first harmonic, and overall sound pressure level. Figure 4.20(a) shows the directivity pattern at BPF. The confidence interval, i.e., mean $\pm$ standard deviation, is also shown as dotted lines. As observed, the BPF tone is reduced at all recorded positions except at 0°, which lines up with the axis of the simulator. Significant reductions, greater than 3 dB, are obtained at most positions. The maximum reduction is 8.2 dB at the 20° position which agrees well with the 7 dB reduction obtained in the work by Leitch [25. 30]. Note that aerodynamic measurements by Leitch showed nearly full filling of the wake in his experiments. Since the same setup is used, it is quite reasonable to conclude that nearly complete filling of the wake is also achieved here. At this speed, the principal radiation angles of the modes cut-on at the BPF due to IGV-rotor interaction are also calculated according to Eqn. (3.26). The rotor-EGV interaction does not have any cut-on modes at BPF. From Table 3.6, the cut-on modes due to IGV-rotor interaction at the speed of 30,000 rpm are $(\pm 2, 0)$, $(\pm 2, 1)$ and $(\pm 6, 0)$ whose principal radiation angles are computed to be $\pm 19^o$, $\pm 48^o$ and $\pm 61^o$, respectively. The maximum reduction angle observed in the

(a). Sound pressure level at BPF (dB)

(b). Sound pressure level at 2BPF
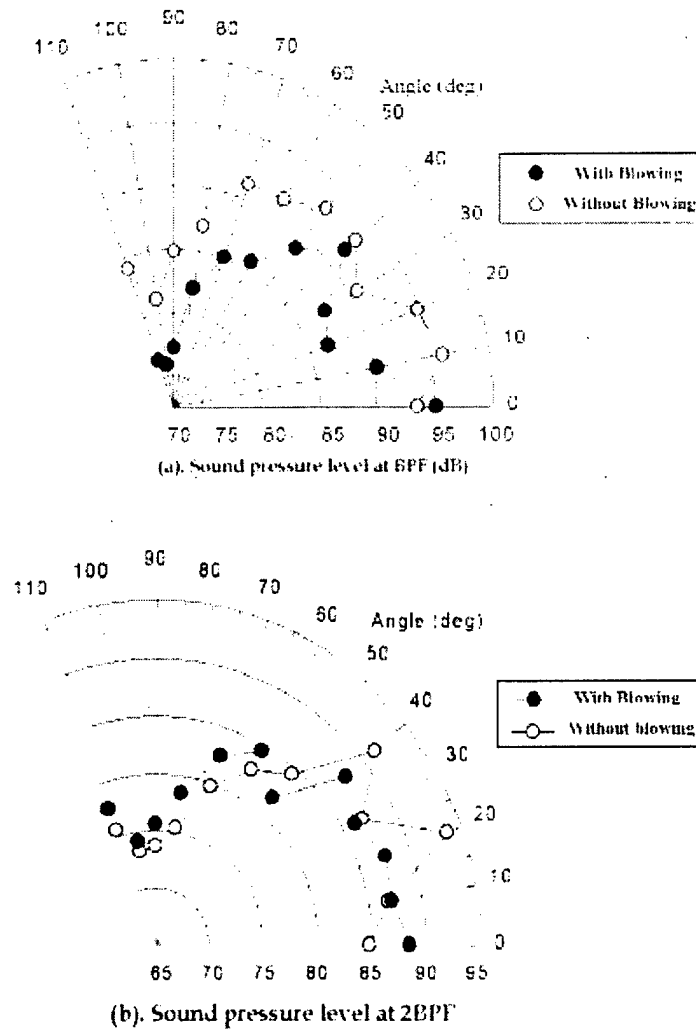
Figure 4.20: Directivity of BPF tone at 30,000 rpm.

experiments is 20° which agrees very well with the predicted 19° for mode (2.0). This implies that mode (2.0) is greatly reduced due to the trailing edge blowing.

Figure 4.20(b) shows the radiation directivity at the first harmonic, i.e., 2BPF. In this case the reductions are confined to the sector from 20° to 50°, inclusive. The maximum reduction of 6.1 dB also occurs at the 20° position. The pressure levels observed outside of this sector are increased. As predicted in Table 3.6, there are much more propagating modes present in the inlet. The far-field directivity depends on the combined radiation of all the generated modes, including interference effects. Trailing edge blowing reduces the amplitude of modes propagating due to IGV-rotor interaction. The destructive interference of these modes with modes generated by other mechanisms is affected by this amplitude reduction. This would cause the sound pressure level to increase along certain directions.

4.5.2   Sound radiation pattern at 40,000 rpm

Figure 4.21 presents the acoustic data recorded at a simulator speed of 40,000 rpm. As shown in Figure 4.21(a), the BPF tone shows reduction in the sector 0° to 50° which

agree with the calculated principal lobe angles due IGV-rotor interaction of 14°, 35°, 40°, 51° and 78°. It implies that the far-field sound level at BPF is mainly contributed by IGV-interaction as compared to other interactions. The average reduction over all measured positions is 2.7 dB, with a maximum of 7.3 dB at 20°. In the sector 60° to 110° it can be observed that the sound pressure level with and without trailing edge blowing remains the same.

The first harmonic levels exhibit reductions at most positions, as shown in Figure 4.21(b). The sound pressure level at 20° increases by 3.2 dB after trailing edge blowing. This could be due to unmasking of modes due to other interaction mechanisms such as core flow distortion in the inlet. The peak reduction is 3.1 dB at 30°.

Trailing edge blowing to re-energize the wakes from the IGVs results in the suppression of the IGV-rotor interaction effect. However, the far-field radiation is due to the contribution of several noise sources, in particular the IGV-rotor, rotor-rotor, rotor-EGV interactions and inlet flow distortions as a result of the lack of an inlet flow control device. Thus, the maximum allowed reduction in the radiation directivity from re-energizing the IGV wakes is limited by the presence of the rotor-rotor, rotor-EGV interaction and inlet flow distortion. In the experiments performed to obtain the radiation directivities, the wakes were effectively re-energized. i.e., the wake total

(a). Sound Pressure Level at BPF (dB)

(b). Sound pressure level at 2BPF (dB)
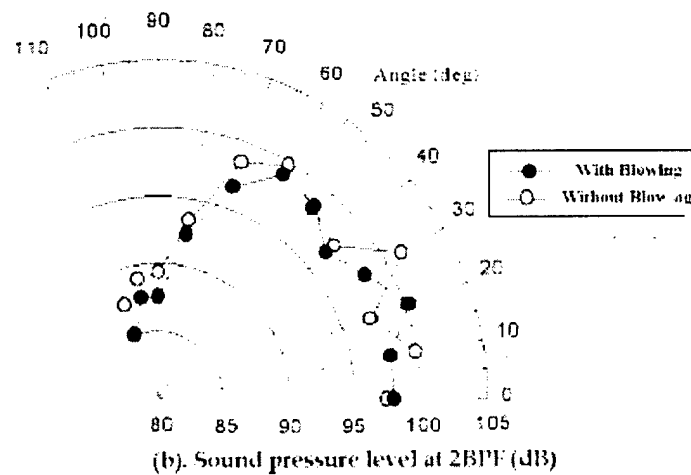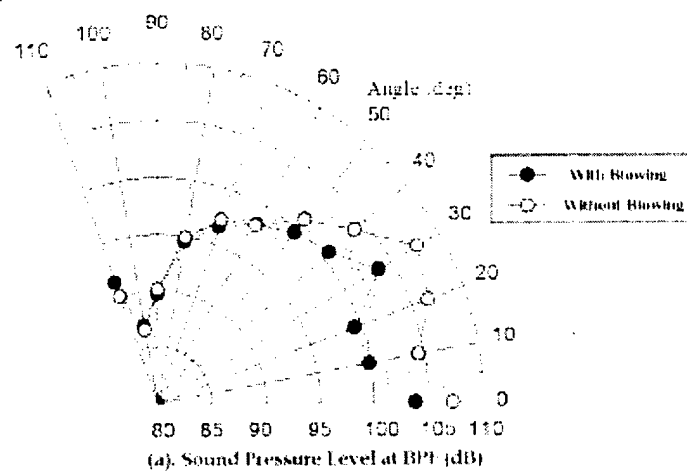
Figure 4.21: Directivity of BPF tone at 40,000 rpm.

pressure was equal to the free stream total pressure (see Figure 4.15). Because of this, it is believed that the radiation directivities with trailing edge blowing shown in Figure 4.21 are due from both the rotor-rotor and rotor-EGV interactions, and inlet flow distortion. In addition, since all the modes excited by the rotor-EGV interaction are cut-off at a simulator speed of 30.000 rpm as indicated in Table 3.6, the radiation directivities with trailing edge blowing shown in Figure 4.20 are due only from the rotor-rotor interaction and inlet flow distortion.

4.5.3   Sound power level reductions at 30,000 rpm and 40,000 rpm

Determining the sound power has the advantage that it describes the sound energy output of the source, without regard to the directivity. Therefore, the sound power reduction may provide a better indication of the effect of trailing edge blowing on reducing the sound source strength. This analysis provides an estimate of the change in sound power level with trailing edge blowing helps better understand the effect trailing edge blowing has on the unsteady interaction. The radiated sound power, W, is computed from the radiation directivities by integrating the far-field acoustic

intensity

$$W = \sum_{i=0}^{11} \frac{p_{i,rms}^2}{\rho c} A_i \qquad (4.12)$$

where $p_{i,rms}$ is the effective sound pressure measured at the i_{th} microphone location: A_i a surface area where the sound pressure is assumed to be uniform and represented by the measurement at the i_{th} microphone location. In the calculation. a surface area $A_i = 2\pi R^2 sin\theta \cdot \pi/18$ is used where the radius R is shown in Figure 4.18 [40].

The BPF power reduction is significant at both test speeds as shown in Table 4.2. At 30,000 rpm, the power in the BPF tone was reduced by 4.4 dB. At 40,000 rpm the reduction in the BPF tone power was 2.9 dB. A reduction in far-field acoustic power can be directly interpreted as a reduction in the source power. Trailing edge blowing reduces the magnitude of the velocity defect seen by the rotor and also smooths the velocity profile. In doing so, this decreases the unsteady loading experienced by the blade as it passes through the wake, and hence the reduction in source strength.

At the same speed the blade passing tone power is reduced more than the first harmonic tone. This is probably because the wake-filling is not perfect, i.e.. "jet-like" or "double-humped" which will be discussed in next chapter. The "jet-like" wake-filling does not lead to much reduction in the harmonics because the harmonic loading on rotor blades,

Table 4.2: Sound power level reduction.

	30.000 rpm		40.000 rpm	
	BPF	First Harmonic	BPF	First harmonic
Before active control	101.4 dB	96.2 dB	111.6 dB	108.0 dB
After active control	97.0 dB	94.2 dB	108.7 dB	107.0 dB
Power level reduction	4.4 dB	2.0 dB	2.9 dB	1.0 dB

obtained through transforming the jet-like forcing function into the frequency domain using FFT, do not alter much as compared to pure wake forcing function. The lesser power reduction at the higher speed is probably because with an increase in speed the acoustic power generated by the rotor-EGV interaction increases as well as inlet flow distortions.

4.6 Summary

An active flow control system with the Pitot probes as the wake sensors is successfully developed to obtain effective wake management through trailing edge blowing in a rotating environment. Although Pitot probes are intrusive sensors which are not

appropriate for realistic engine systems, use of pitot probes is a preliminary step toward more in-depth for TEB control research. More importantly, results obtained from this system can serve as the baseline in evaluations of other possible control systems indirect wake sensing.

A 4-channel PID controller generates the signal voltage that controls the flow rate through each microvalve. The inputs to the PID controller are the total pressures in the free stream and wakes behind each IGV. The error signal is computed as the difference between these signals, with the free stream total pressure as the reference. Pitot probes immersed in the flow measure the wake total pressures that are used as inputs to the controller. The advantages of this Pitot-probe based system are that effective wake-filling is achieved and changes in operating condition can be tracked for effective wake management with changing conditions.

From the results presented it can be concluded that the Pitot-probe based active TEB control system produces a very uniform flow field downstream of the IGV. This is because a Pitot probe measures the direct wake signal which is exactly what the controller seeks to minimize. The ability of the system to achieve optimum wake filling when subjected to a change in inlet flow conditions demonstrates the feasibility and advantage of active flow control. It was also demonstrated that far-field sound pressure

levels at the relevant discrete frequencies are reduced by trailing edge blowing. Furthermore, the reduction in sound source strength supports the effectiveness of trailing edge blowing in reducing unsteady IGV-rotor interaction. The maximum sound level reduction is observed at the blade passing frequency of each tested speed. The maximum tone reductions obtained are around 8.2 dB at 30.000 rpm and 7.3 dB at 40.000 rpm. Sound power level at the BPF tone, calculated from the measured directivity, is reduced by 4.4 dB at 30.000 rpm and 2.9 dB at 40,000 rpm.

However, as mentioned early in this chapter, the drawbacks of using Pitot probes are obvious. This is mainly because Pitot-probe based TEB control is not appropriate for the real engine environments. Therefore, there exists a demand to develop an advanced TEB control system which does not require Pitot probes. In the next chapter, a nonintrusive control system based on microphones is introduced.

Chapter 5

Microphone-based Flow Control

Systems

New flow control systems based on the microphone sensors will be described in this chapter. The non-intrusive wake sensing approach enables the active flow control system to eliminate the need of intrusive Pitot probes as presented in Chapter 4. The significance of using acoustic sensing lies in that it provides a more feasible approach toward the realistic engine TEB control applications.

106

In section 5.1, the motivation of the acoustic sensing approach will be briefly described. The experimental setup using the microphone sensors follows. A unique signal processing device will be discussed in section 5.3. Two control schemes will be developed in section 5.4 and 5.5, respectively as well as the results obtained from both control schemes.

5.1　Introduction

The experimental tests in Chapter 4 demonstrated the potential of using Pitot probes as the wake sensors for optimum re-energizing of the wakes. However, there exist several drawbacks of using Pitot probes. First, such probe is not practical to be used in the true engine environments. Extreme care needs to be taken for the sensor to be mounted into the right position and angle. Secondly, Pitot probes are intrusive sensors which themselves can create the wakes. Lastly, the Pitot probes can only be used to sense the wake of non-turning IGVs. This is because Pitot probe can only sense correctly the flow velocity at a fixed angle (i.e., pointing along a streamline). However, the wake region of a curved IGV turns pitchwise as the engine operating condition changes. i.e. when inlet Mach number changes. Curved IGVs are widely

used in aircraft engines. Thus, there is a need to develop non-intrusive wake sensing strategies to infer the filling of the wakes.

In this chapter, an acoustic sensing approach using microphones is proposed to indirectly sense the wake-filling. The basic idea can be obtained from Figure 3.1. The figure shows that the upstream IGV wake is a common forcing function to tonal fan noise and blade vibrations. Therefore, when the wake is fully re-energized by TEB, both blade vibration and tonal fan noise are minimized. It follows logically that a reduction of tonal fan noise by TEB implies a reduction of fan blade vibrations as well. From this point of view, microphones used for acoustic sensing can be viewed as the indirect "wake sensors" or "vibration sensors" and thus offers the potential to be integrated with the other elements of TEB control system.

Two TEB control schemes in conjunction with the microphone sensing approach will be presented in this chapter. In the first control scheme only the magnitude of the BPF tone is used to generate the error signal for the controller. In this case, an optimal controller is implemented. The second control scheme consisted of using both the magnitude and phase of the BPF tone sensed by the microphones. In this second approach, a PID feedback controller is implemented. These control approaches are next described and their performance were tested.

5.2 Experimental Setup

Figure 5.1 shows a schematic of the experimental setup with the microphones as the indirect wake sensors. Compared to Figure 4.1, its shows that the Pitot probes are removed while the microphones are flush mounted on the inlet wall. The basic control idea is that the microphones sense the noise induced by the IGV-rotor interaction. This information is then provided to a digital controller that generates the control signals for the MEMS based microvalves to reduce the noise from this interaction. The reduction of the noise signature results in effective wake-filling.
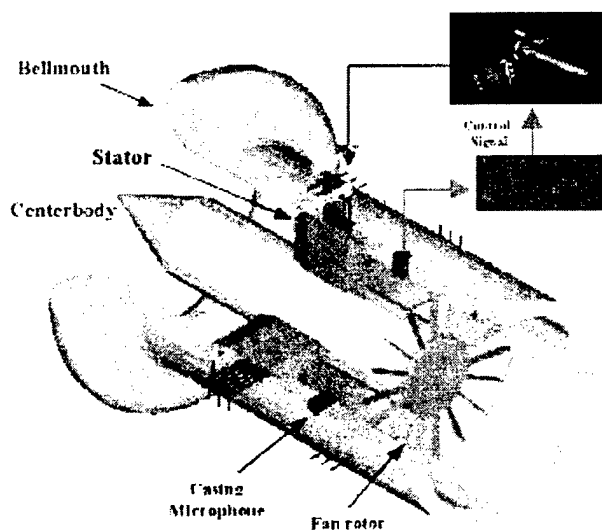
Figure 5.1: Microphone-based experimental setup.

The microphones used in the experiments are high-intensity microphones (model 106B) from PCB Electronics, as shown in Figure 5.2(a). This microphone is specially designed to measure pressure perturbations in air or in fluids in severe environments. They can also be used to measure very small pressure disturbances on a much higher static head, with certain precautions. Such microphone features high-sensitivity. acceleration-compensated quartz pressure elements coupled to built-in integrated circuit impedance converting amplifier. The quartz elements in model 106B microphone utilizes a special cut in quartz to produce a proportionately higher output voltage than the standard X-cut compression crystal normally used. A built-in seismic mass acting on another quartz crystal effectively cancels the spurious signal produced by the mass of the diagram and end piece acting upon the very sensitive crystals in the presence of axial vibration inputs. This design produces an extremely high level output signal with good resolution, relatively free from unwanted vibration effects. Figure 5.2(b) shows the cross section of 106B microphone elements. As with all quartz sensors, the high rigidity results in negligible diaphragm producing excellent linearity from the threshold pressure to full-scale pressure as seen in Figure 5.2(c). The high rigidity of quartz also results in sensors with high natural frequency, giving a very wide useful frequency range. The built-in electronics consists of a voltage follower with unity gain. A single wire feeds constant current power to the voltage follower and also carries the dynamic signal. Caution needs to be taken never to apply power directly to the microphone

(a)

Connector

Integrated
Circuit
Amplifier

Potting

Mounting
Clamp Nut

Acceleration
Compensation
Mass and Plate

Seal Ring
Preload Sleeve
Electrodes
Housing

Quartz Plates

Diaphragm
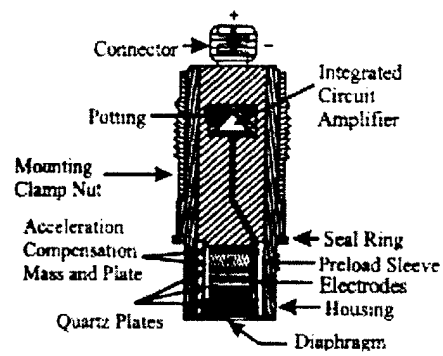
(b)
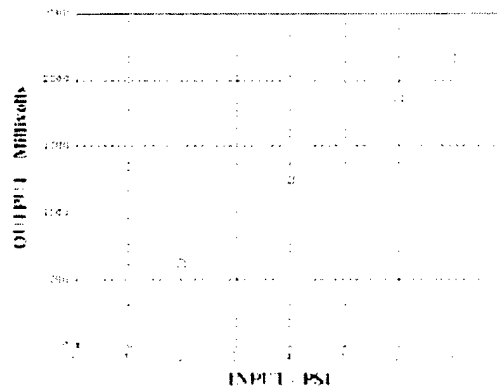
(c)

Figure 5.2: The model 106B microphone from PCB Electronics. (a) microphone view; (b) microphone cross-section; and (c) performance curve.

without the current-limiting protection (2 mA maximum). as to do so will destroy the built-in amplifier.

In the experimental setup, four high intensity microphones are flush mounted on the inlet wall right behind the four IGVs, named IGV A, B, C and D, respectively as shown in Figure 5.3. Accordingly, the four microphones behind IGV A, B, C, and D are referred to as microphone 1, 2, 3, and 4, respectively for convenience. The microphone 3 can be seen to be flush mounted behind IGV C. As stated before. the four wakes behind the IGVs become the four noise sources at the fan face when they are chopped through the rotor. Placing the microphones in between the IGVs and the rotor makes them to sense these noise sources effectively at BPF and its harmonics. In the experiments here, the simulator is operated at a speed of 30,000 rpm, which leads to a BPF tone frequency of 9,000 Hz.

5.3 Adaptive Extraction of BPF Tone

The implementation of the acoustic sensing strategy requires some unique signal processing. The simulator radiated noise spectrum consists of a set of dominant tones and
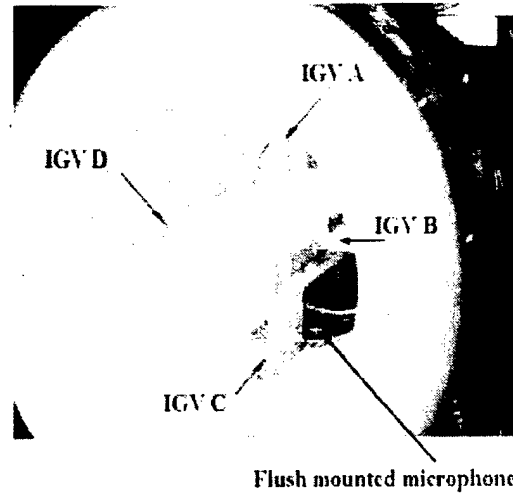
Figure 5.3: Simulator inlet with four casing microphones behind four IGV's.

a broadband component as can be seen in Figure 4.19. One of the sources of the tonal components at the BPF and harmonics are due to the IGV-rotor interaction, i.e., noise due to the wakes Thus, the tonal component information instead of broadband noise needs to be extracted out for use in the active flow control system.

Furthermore, the BPF tone is selected to construct the error signal for the control system. This is primarily because BPF tone is expected to dominate the tonal component according to the fan noise generation mechanism. (The fan noise generation will be discussed in detail in Appendix C). The basic concept of the mechanism is given briefly here as follows. Since the fan noise is generated as the rotor blades chop through the

upstream IGV wakes, the upstream wake can be viewed as the forcing function applied to the rotor. A possible shape of the forcing function, $f(t)$, can be illustrated in Figure 5.4 with a period of $1/f_{BPF}$ since the blades chop through the wake at the frequency of BPF. The variation of the trace is due to the flow variation in the wake. The generated sound energy distribution at BPF and its harmonics is determined by the frequency distribution of the forcing function, which can be computed by using Fourier series expansion with the fundamental frequency of f_{BPF}. The regular Fourier series expansion is expressed as:

$$f(t) = \sum_{n=-\infty}^{\infty} F(nf_{BPF}) \cdot e^{inf_{BPF}t} \qquad (5.1)$$

where $F(nf_{BPF})$ is the complex Fourier coefficient; n denotes the harmonics index. According to the periodical shape shown in Figure 5.4, the largest Fourier coefficient would occur at the fundamental frequency, f_{BPF}. Therefore, the generated noise at BPF is dominant. Another reason of choosing BPF tone, instead of its harmonics, to construct the error signal is because high order harmonics would not be expected to be reduced if a momentumless wake is filled "jet-like" or called double-hump as shown in Figure 5.5. "Jet-like" wake-filling can occur easily in practice since the TEB jet can not be spread out adequately downstream IGV.

The most challenging part in obtaining BPF tone from the broadband spectrum is the
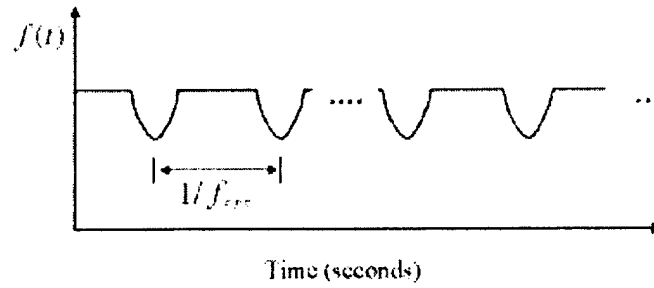
Figure 5.4: The shape of the forcing function applied to the rotor.
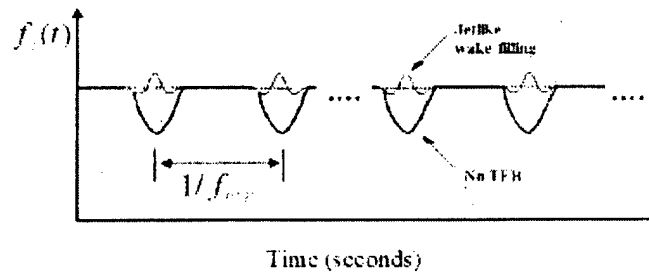
Figure 5.5: The shape of the forcing function with TEB.

requirement of adaptivity. This is because as the engine speed changes, the BPF will also vary, which makes a conventional bandpass filter with a fixed center frequency insufficient. Other requirements includes the reliability, insensitivity to temperature, precision and so forth. The conventional approach is using DSP-based algorithm, i.e. the adaptive filter with LMS (least mean square) algorithm [60]. This method requires a complicated hardware system which includes ADCs to convert the continuous signals into digital signals, a DSP with adaptive filters, and DACs to convert the digital signals

back to the continuous domain.

To this end, a novel adaptive bandpass filter device is developed and tested to capture the BPF tone component from the acoustic signatures of the simulator. Compared to the conventional DSP-based methods [60], this extractor pertains some attractive properties which includes the high performance in terms of reliability, steady-state error, respond time, precision and sensitivity to temperature. In addition, it is easy to implement since there is no need for DSP and their programming.
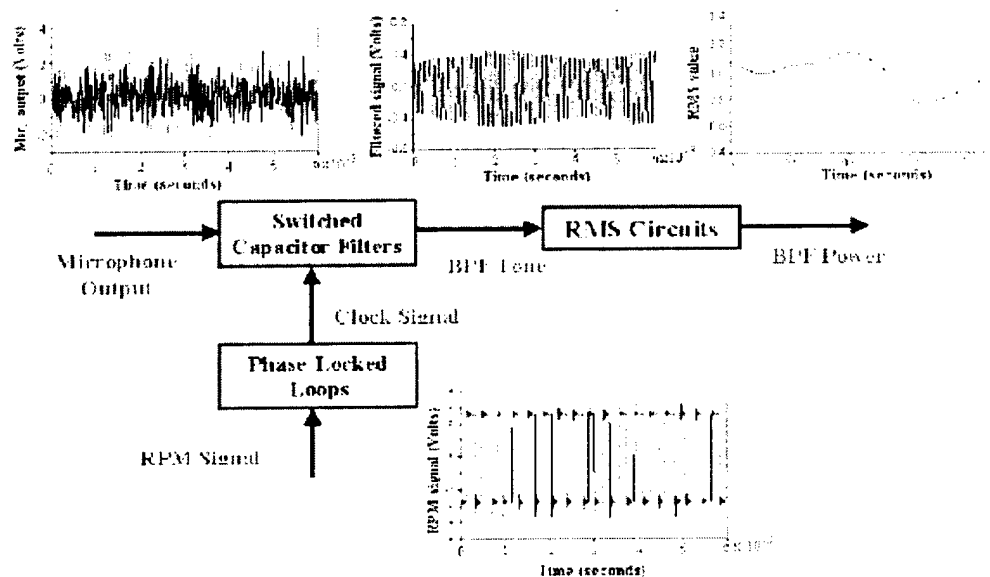
Figure 5.6: The block diagram for the adaptive BPF tone extractor.

Figure 5.6 shows the block diagram of the device which consists of two important components. The BPF tone is obtained by using an analog, high-Q bandpass switched-capacitor filter (SCF) whose center frequency adjusted using the simulator shaft signal. i.e. referred here as the reference signal or RPM signal. Another component is the phase-locked-loop (PLL) which is used to condition the rpm signal. The idea is that the reference signal, after conditioning, is input into a PLL circuit. This PLL circuit is designed to generate the clock signal for the SCF. The clock signal changes with the reference signal, i.e. the clock signal tracks the reference signal. The center frequency of the bandpass SCF is determined by the clock signal which in turn is controlled by the reference signal through the PLL circuit. Thus the filter center frequency "adapts" or "tracks" the reference signal. The RMS (root mean square) circuit follows the SCF to compute the BPF tone power or magnitude. The various time domain signal in the device are also shown in Figure 5.6. As can be seen, the BPF tone embedded in the microphone output signal is converted by the device to a DC value which will be input to a digital controller.

Figure 5.7 shows its excellent static performance in frequency domain (Figure 5.7a) and in time domain (Figure 5.7a) using the experimental data obtained from simulator testing. The unfiltered signal which consists of tonal component and broadband background noise is from one of the casing microphones when the simulator is running at
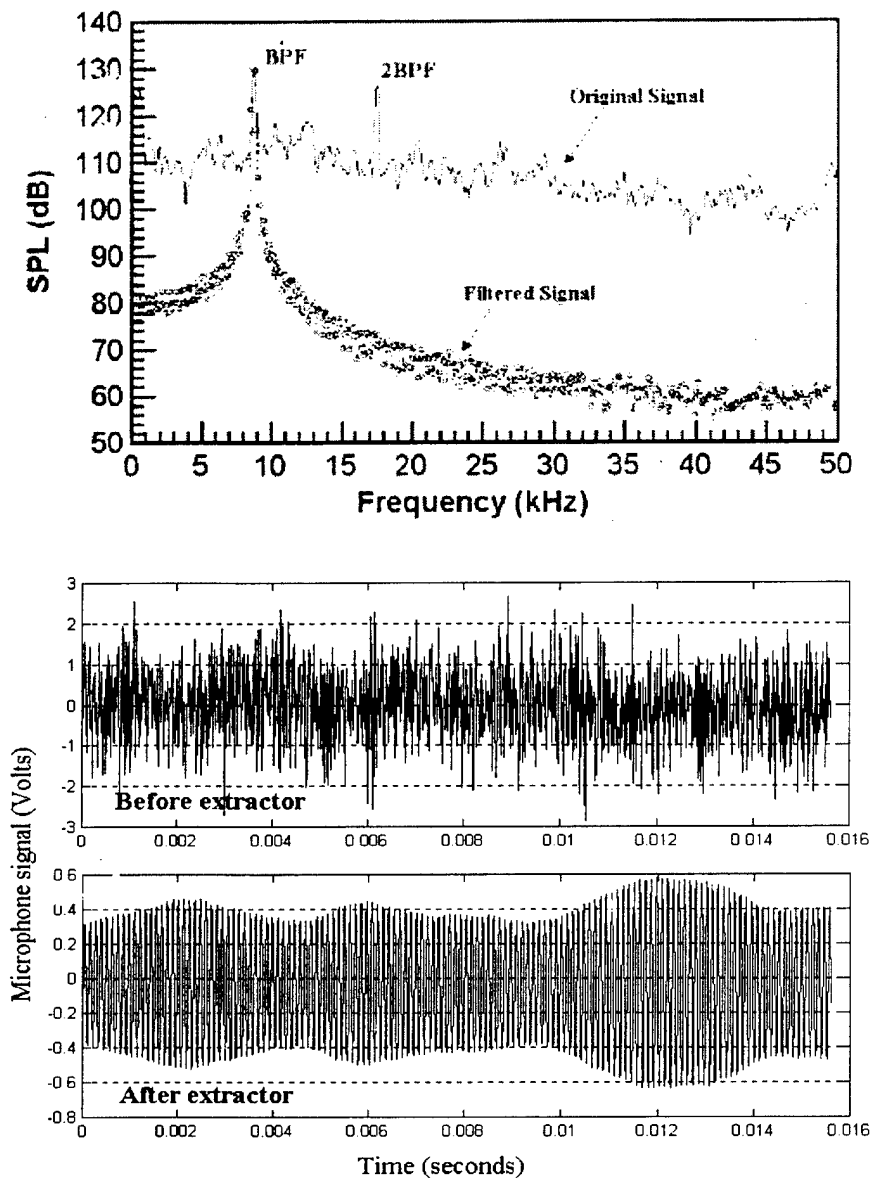
Figure 5.7: The static performance of the adaptive BPF extractor (a) in frequency

domain; (b) in time domain.

around 30,000 rpm. Figure 5.7a indicates that only the BPF signal is filtered out while the higher harmonics and broadband background noise are rejected. This comparison can also be seen in time domain in Figure 5.7b which shows a clean sinusoidal wave and original microphone output signal. It is worth to point out that no low pass filters are needed for the original microphone signal in order to prevent frequency aliasing before it is fed to the SCF. This is because the clock frequency for the SCF is much higher than the upper-limit frequency in the frequency response of a casing microphone. Low pass filters are often required in a conventional data acquisition system. In addition, higher Q-factor for this adaptive filter can be obtained through a serial connection of multiple SCFs. Four SCFs are cascaded in the device for each microphone output signal.

The dynamic performance of the device mainly depends on the dynamic performance of the PLL. The major performance parameters of a PLL includes the tracking speed, hold-on range, lock-in range and pull-in range. Appendix A has more details about these parameters and how to obtain them. In this case, the two most important parameters are hold-on range and tracking speed. The hold-on range Ω, which is the range of frequency over a loop will *remain* locked, is evaluated for this extractor to be 20,000 rpm — 81,000 rpm in terms of simulator speed. Note this range is broad enough to cover the operating range of the simulator which is 20,000 rpm — 40,000 rpm. The

tracking speed. when evaluated in terms of setting time t_s in the step response. is about 1 μSecond. This means the center frequency of the adaptive filter can adapt to the input signal in 1 μSecond in response to a unit step in the simulator speed. It is noted that this setting time is short enough for our application case.

5.4 Acoustic Sensing Approach Using BPF Magnitude

5.4.1 Control algorithm

As mentioned earlier, the IGV wake - rotor interaction effect results in strong tones at BPF and harmonics. The re-energizing of the wake by TEB leads to noise attenuation due to the reduction of IGV-rotor interaction. In addition, the optimum wake-filling minimizes the BPF tone acoustic signal. Thus, the power of the BPF tone sensed by the casing microphones as a function of the trailing edge blowing rate will have a minimum at the optimum blowing as shown in Figure 5.8. It is important to reiterate that the acoustic signal will not be driven to zero because of two factors. The first

factor is that the IGV-rotor interaction is not the only noise source at the BPF tone and harmonics. The other noise sources are the rotor-rotor. rotor-EGV interactions as well as flow distortions ingested into the inlet due to the lack of a flow inlet control device (ICD). Though the acoustic modes induced by the rotor-rotor and the rotor-EGV interactions are cut-off at the simulator speeds tested, ingested distortions will not be eliminated by the TEB. The second factor that the BPF tone is not completely eliminated is simply because the wake re-energizing process is not perfect. i.e. there is some wake deficit left after TEB.
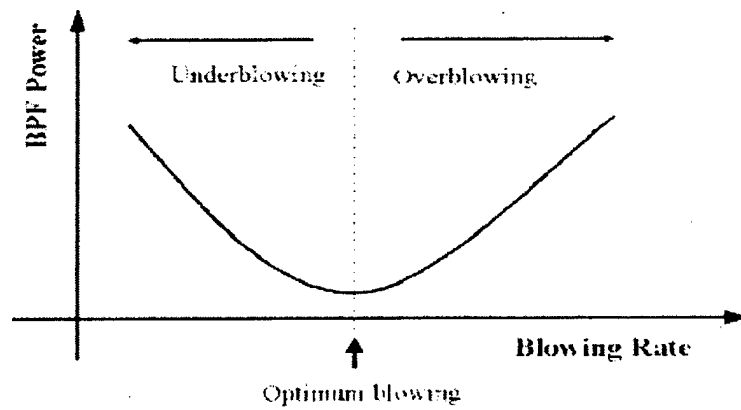
Figure 5.8: The BPF power in casing microphones as a function of TEB rate.

An experiment is performed on the simulator in the anechoic chamber to verify this

behavior in the inlet microphones before the active control scheme is developed and tested. This is conducted by measuring the SPL of the BPF tone in both far-field and inlet microphones as a function of TEB rate. The results for the simulator speed of 30,000 rpm are shown in Figure 5.9 where the blowing rate sweeps from no-blowing to over-blowing. The dashline represents SPL of the BPF tone sensed in the far-field microphone at 20° of the simulator axis. The solid line is the SPL of the BPF tone measured by the casing microphone behind IGV A (see Figure 5.3, Page 113). It can be found from the figure that the maximum noise reduction in both of the casing and far-field microphones occurs at the same blowing rate. This indicates that the maximum BPF tone reduction in the casing microphones, which will be achieved after the non-intrusive controller has converged, can also infer the best wake-filling, just as the maximum BPF tone reduction in the far-field microphones infers the best wake-filling. The significance of this conclusion lies in that it provides the justification for the TEB control using acoustic sensing approach.

Therefore, the first control scheme is to implement a simple optimal controller that determines the optimum blowing rate by searching for the minimum of the BPF power curve in Figure 5.8. Figure 5.10 shows the block diagram for the control system. The feedback loop starts from the four microphones signals, which are pre-conditioned before they are used by the adaptive BPF extractor. The simulator RPM signal, which
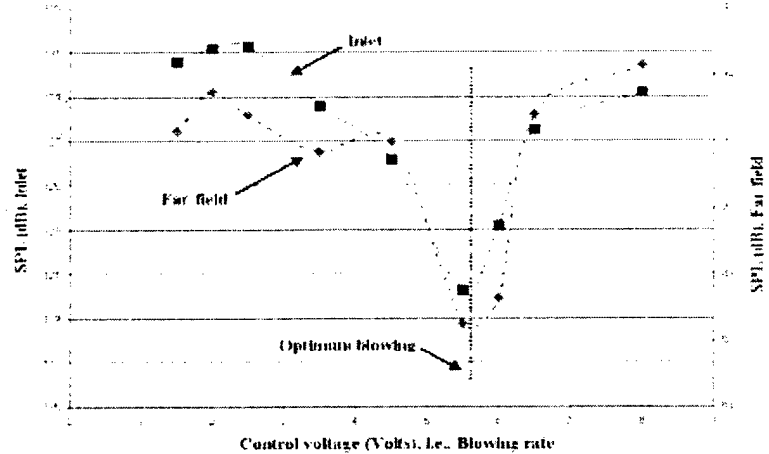
Figure 5.9: Sound pressure level at BPF tone in the far-field and casing microphones.

is obtained from a magnetic pickup built in the simulator, is used to synchronize the

BPF extractor so that its center frequency can track the BPF signal with simulator

rotating speed. The output of BPF extractor, which is a DC value, serves as the

error signal for the digital controller. The controller generates the control signal for

the MEMS based microvalves. It is important to point out here that different offset

voltages should be used in the microvalve offset circuits to compensate for the variations

between the four IGVs. According to the results shown in Figure 4.17 where Pitot

probes were used as flow sensors, the offset voltages of 4.5, 4.0, 3.5, 3.0 Volts are

applied to IGV C, D, B and A, respectively. Hence, the same control signal can be

used to drive all the microvalves of the four IGVs, i.e., SISO controller. The control

algorithm used here aims to locating the minimum of the curve shown in Figure 5.8. In

the context of control theory, this is a typical one-dimensional optimal control problem: A gradient method is utilized to search for the minimum moving along the opposite of the function gradient. That is,

$$U_{k+1} = U_k + D_k \cdot S \tag{5.2}$$

where U_k is the control signal at time t_k, S is the step size, and D_k is the search direction with the initial value of 1 which is updated as:

$$D_{k+1} = \begin{cases} D_k & \text{if } \bar{e}_{k+1} > \bar{e}_k \\ -D_k & \text{if } \bar{e}_{k+1} \leq \bar{e}_k \end{cases} \tag{5.3}$$

where $\bar{e}_k$ denotes the time-averaged BPF power from all the four casing microphones, at time t_k.

Time-averaging is needed because the BPF tone signal fluctuates severely due to the unsteady behavior of the rotor interacting with the distorted incoming flow. The upstream incoming flow distortion is probably mainly due to the lack of an ICD which is commonly used to make the inlet flow uniform [61]. Another source is from the unsteady nature of the IGV wakes such as vortex shedding, etc. A typical BPF tone waveform is shown in Figure 5.11 when the simulator runs at a constant speed. It can be found from the figure that the maximum amplitude of BPF is about 9 times the minimum amplitude, i.e. the maximum variance of BPF signal is about 19.1 dB. In
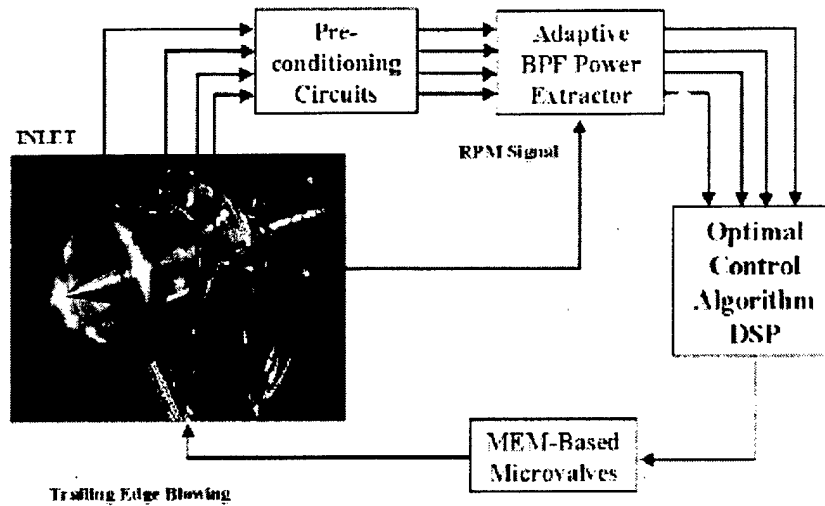
Figure 5.10: The block diagram for the control system using casing microphones.

the experiments, an averaging time of 4 seconds is required to get a steady value for BPF power. The long averaging time of 4 seconds would lead to a slow response in the TEB control system which is a clear drawback. However, this control approaches is still pursued since one of the objectives in this chapter is to demonstrate the concept of TEB control using acoustic signature.

Another note on Eqn. (5.2) is that the step size, S, needs to be relatively large, which is again required because of the fluctuation of BPF tone. This is because it would be difficult to detect the trivial change in the BPF power if the blowing rate varies insignificantly as a result of the use of a small step size. In technical words,
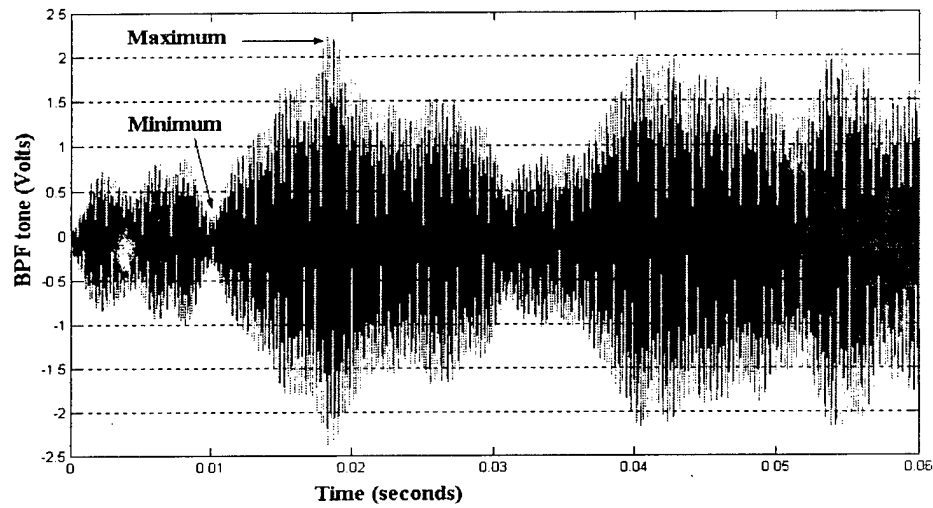
Figure 5.11: A typical time history of the BPF tone in casing microphone.

the fluctuation of BPF tone may lead to some local minima as well on the curve in Figure 5.8 in addition to the global minimum, which may prevent the controller from converging to the global minimum if a small step size is used. In the experiments, a step size of 0.2 volts is used.

5.4.2   Results and discussions

This section describes the experimental results obtained from the tests conducted in the anechoic chamber. These results include the TEB controller performance, and the noise reduction in the far-field and inlet microphones.

Controller performance

As mentioned earlier, the purpose of the optimal feedback control system is to achieve the optimum blowing rate by searching for the minimum point of the curve shown in Figure 5.8 according to the control algorithm described.

Figure 5.12 the RMS signal time history of the BPF tone, i.e. error signal, during the adaptation process as well as the control signal driving the microvalves. The simulator is running at the speed of 30,000 rpm. The air source pressure for TEB is 80 psi in the plenum. The initial conditions of the MEMS based microvalves are fully open. It is clear that the control system is effective in reducing the BPF tone in the casing microphones to the minimum. The control signal. which was updated every 4 seconds, is able to converge to the optimum solution, i.e. the optimum blowing rate in Figure 5.8, in about 40 seconds. It is interesting to note that the control signal oscillates around

the optimum steady-state value that also results in a very low frequency oscillation of

the error signal, i.e. the control system meanders around the optimum blowing.
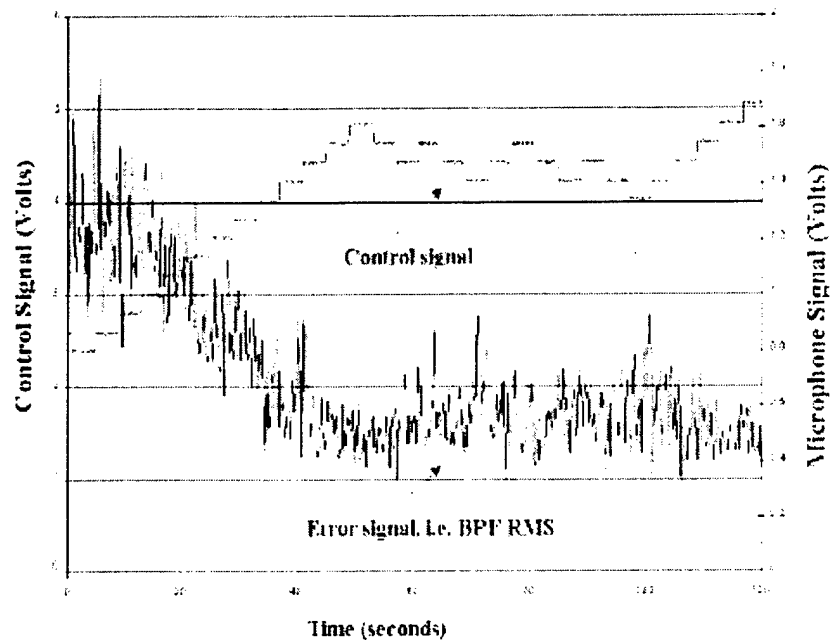
Figure 5.12: The convergence process of the optimal controller.

Acoustic results

Similarly as in Chapter 4, the sound field is monitored at far-field locations in the anechoic chamber. It is known that the successful wake-filling leads to the reduction of the tonal noise components due to the suppression of the interaction between the IGV wakes and the fan blades. Thus, the amount of the noise reduction at the tonal noise can serve as an indication of the successful re-energizing of the wakes. Figure 5.13 shows the noise spectra in the far-field at 20° of the simulator axis with and without active TEB control. For the purpose of comparison with the results obtained in last chapter. the BPF tone occurs at 9,000 Hz and corresponds to a simulator speed of 30.000 rpm. These spectra demonstrate a reduction of 7.9 dB at the BPF tone and reduction of 5.2 dB at the first harmonic (2BPF). These results agree very well with those obtained using Pitot probes as sensors presented in Chapter 4 with reductions of 8.2 and 6.1 dB at the BPF and 2BPF tones, respectively. Figure 5.14 shows the radiating directivities at the BPF tone of 9,000 Hz without and with TEB control system. As observed. the BPF tone is reduced over the 10° to 80° sector. The sound power level is reduced by 4.9 dB. Again. the reduction is very close to the 4.4 dB obtained using Pitot probe as error sensors in last chapter. It is worth to point out that the difference in the far-field acoustic results obtained from the Pitot-probe-based and microphone-based sensing approaches might be from the intrusive Pitot-probe flow sensors themselves. That is, the Pitot probes can create their own wakes. These acoustic results demonstrate the effectiveness and potential of this non-intrusive acoustic sensing strategy for active
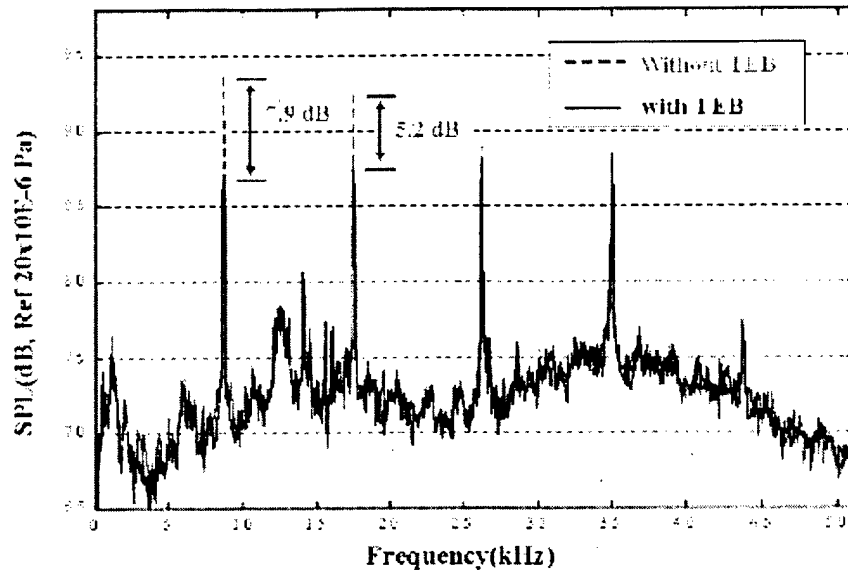
Figure 5.13: Noise spectra at the 20 degree with and without the TEB controller.
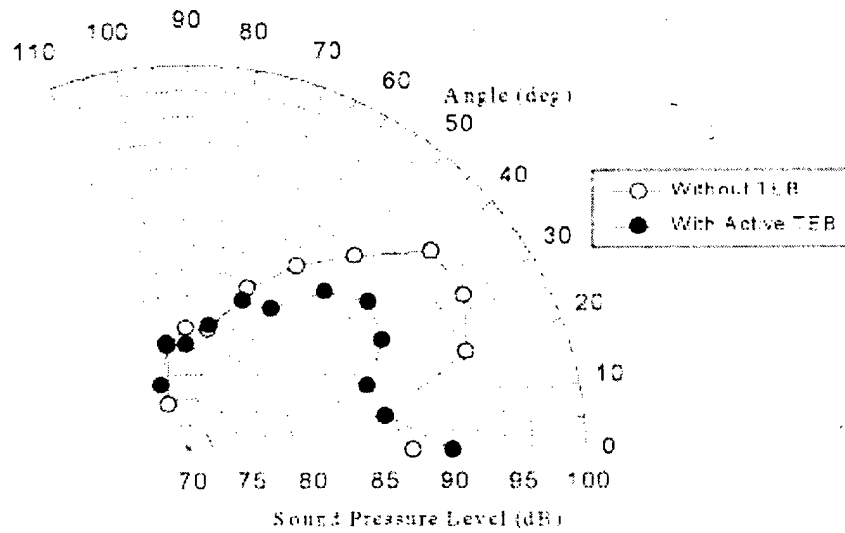
Figure 5.14: Directivity plot with and without the TEB controller.

TEB.

The casing microphone output with and without active TEB is also recorded after the controller has converged. The results in frequency domain and time domain for the casing microphone behind IGV A are shown in Figures 5.16a and 5.16b, respectively. As seen in Figure 5.16a, a reduction 6 dB is achieved at the BPF tone. This result can also be seen in Figure 5.16b where the root-mean-square (RMS) signal of the BPF tone is reduced by a factor of 2. As explained above, the significant variability of the power of the tone is due to the upstream flow distortion. In addition, similarly as in the far-field acoustic spectrum, the wake-filling does not lead to the reduction in the broadband noise.

Discussions and conclusions

Based on the comparison of the results using Pitot probes and the microphone sensors, it demonstrates the feasibility of the acoustic sensing approach to eliminate the need for intrusive flow sensors to successfully fill the wakes and, thus, reduce the unsteady loading experienced by the blades. However, the approach has a main drawback, which is the slow system response as shown in Figure 5.12. This is because the BPF power signal fluctuates severely due to the unsteady behavior of the IGV-rotor interaction. Thus, the controller has to take 4 seconds to obtain a steady time-averaged value
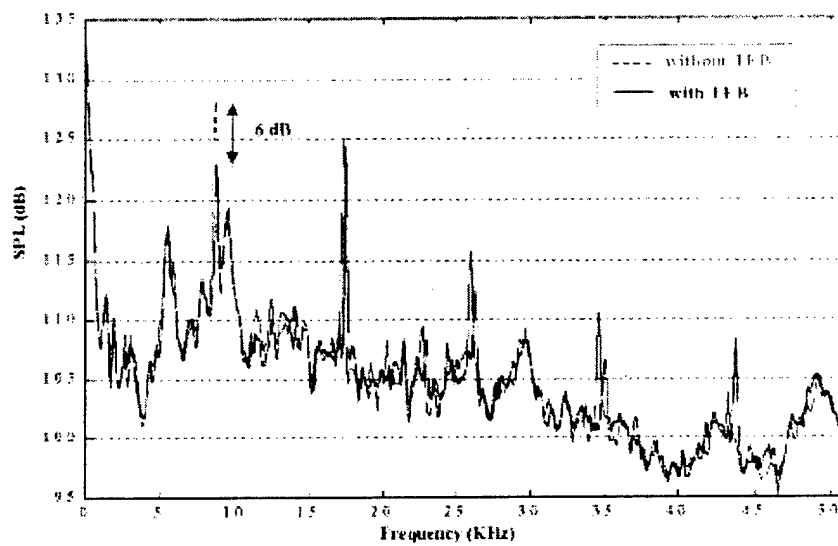
Figure 5.15: The frequency spectrum of the casing microphone signal.
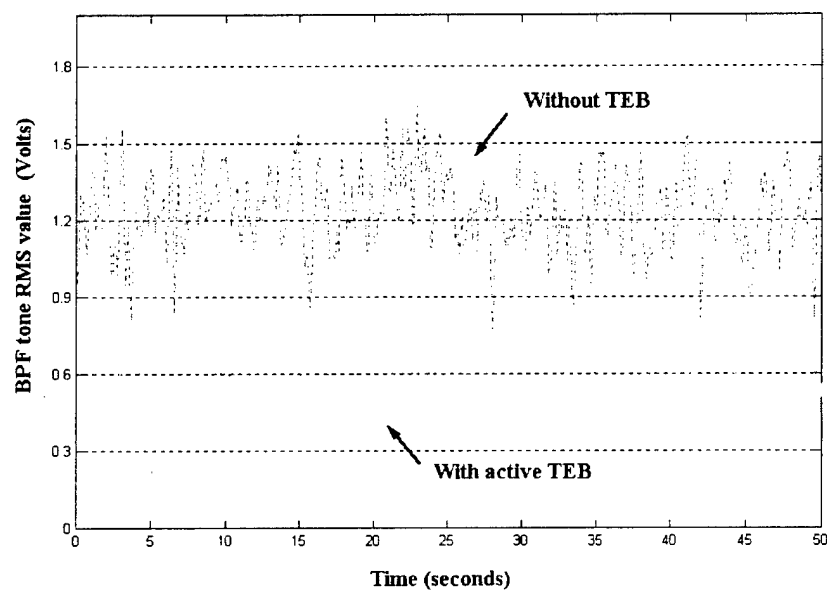
Figure 5.16: The time history of the casing microphone signal.

of the BPF tone power. It is important to remark that the optimal controller had difficulties converging to the minimum if the starting point was not relatively close to the minimum. This slow response ($\sim$ 40 seconds) and the poor reliability makes the control system not practical for real applications where the system has to track sudden changes in engine speeds. This limitation led to the development of the second control scheme investigated in this work.

5.5 Acoustic Sensing Approach Using BPF Magnitude and Phase

5.5.1 Control algorithm

The slow time response of the microphone-based control system can be accomplished by once again implementing a PID controller. To this end, the error signal needs to be able to provide information that allows to distinguish the under and over blowing conditions through a change in the sign of the error signal. This can be accomplished by using both the magnitude and phase information from the BPF tone, instead of
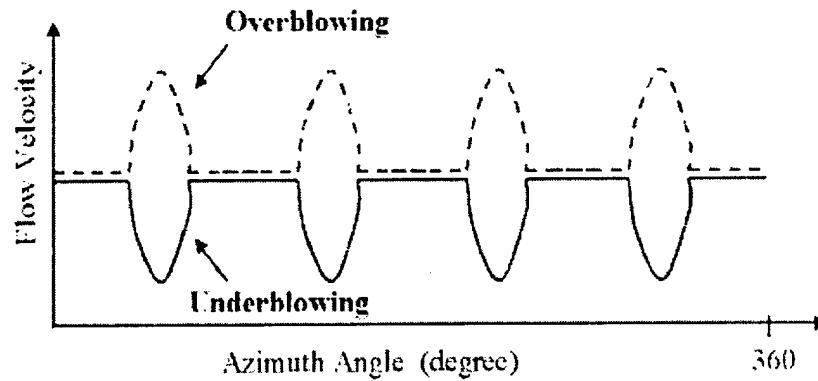
Figure 5.17: The wake profiles in underblowing and overblowing cases.

only the BPF magnitude information used in the first control scheme.

Plotting the circumferential flow velocity profile on the face of the fan for both under and over blowing, as shown in Figure 5.17, clearly indicates that the two conditions are characterized by being out-of-phase. It follows that the phase of the casing microphone signals will also show a 180 phase change between the two blowing cases. Thus, the phase change information in the casing microphone signals in conjunction with the BPF tone magnitude can be used by a PID controller as error signal.

Preliminary experimental investigation at the simulator speed of 30,000 rpm verifies

the above idea. The rpm signal from the magnetic pickup of the simulator serves as the phase reference for measuring the casing microphone phases. Figure 5.18 illustrates that the time-averaged BPF tone phase in casing microphone 2 changes by 180 degree as we keep increasing the TEB air source pressure (0 degree is defined at no TEB). The measurement results for all the four microphones are tabulated in Table 5.1 when the simulator runs at 30,000 rpm. It indicates that the BPF tone phase of all the microphone signals change by about 180 degree from underblowing to overblowing case. A perfect 180° change is not achieved because the BPF tone is generated not only by IGV-rotor interaction but rotor-rotor, rotor-EGV and inlet flow distortion as well. Note that the phase measurement exhibits a large variation at the blowing rate of 40 psi and 50 psi as compared to the other blowing rates. This is probably because the actual supply air pressure has some variation and 40 psi or 50 psi is very close to the optimum blowing. Therefore, the actual pressure at the measurement 40 psi or 50 psi meanders around the optimum blowing. i.e., alternating between overblowing and underblowing which thus leads to the large phase variation. Finally, it should be noted that Table 5.1 shows the result of 180° phase change only at one simulator speed. The results for other speeds will be addressed in the latter part of this chapter.

The formation of the error signal is depicted in the schematic of Figure 5.19. The magnitude of the BPF tone as a function of the blowing rate is shown in Figure 5.19a
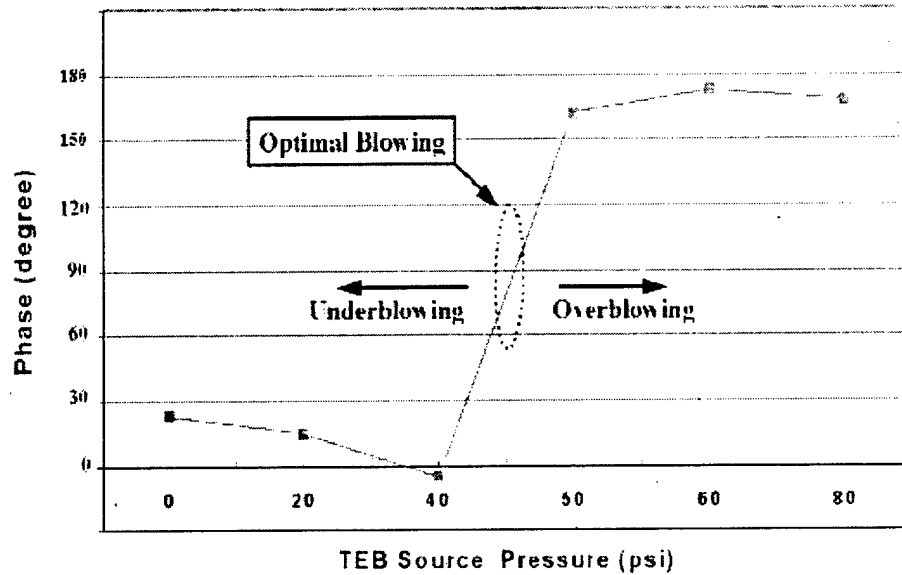
Figure 5.18: The relationship between BPF phase and TEB air source pressure.

Table 5.1: BPF tone phase as a function of blowing rate.

Mic. \ TEB	0 psi	20 psi	40 psi	50 psi	60 psi	80 psi
No. 1	206°	211°	$209^o - 224^o$	$44^o - -13^o$	$3^o - -36^o$	-12°
No. 2	23°	25°	$20^o - -30^o$	$147^o - 177^o$	$162^o - 183^o$	168°
No. 3	182°	165°	$102^o - 133^o$	$20^o - 0^o$	$-2^o - -19^o$	2°
No. 4	-5°	3°	$29^o - 81^o$	$130^o - 160^o$	$183^o - 191^o$	180°

while the phase is plotted in Figure 5.19b. It is important to note that the phase of a signal is always measured relative to another coherent reference signal. The RPM signal from the magnetic speed pickup sensor was used as the reference signal for measuring the casing microphone phases. The error signal for the PID controller can be constructed by first assigning a value from -1 to 1 for the BPF phase of 0 to π. The phase, now in the form of a function ranging from -1 to 1, and the magnitude of the BPF tone are multiplied to yield the error signal in terms of the blowing rate as shown in Figure 5.19c. Thus, a negative error signal will be obtained for under blowing while a positive error signal will be obtained for the over blowing case. In addition, the error signal will vanish at the optimum blowing. Hence, a typical PID algorithm can be used.

In order to implement this control scheme, a real time phase detector is designed. A phase detector converts the relative phase between two signals, the microphone and RPM signals, to a voltage signal so that it is then input into the digital controller. A phase detector with the characteristics shown in Figure 5.20 is proposed for our application [62]. For the phase detector to be insensitive to the amplitude of the input signals. the BPF tone from the casing microphones and the RPM signals are first converted to TTL (transistor to transistor logic) signals. This is important since the BPF tone from the turbofan engine is fluctuating severely in amplitude. The kernel
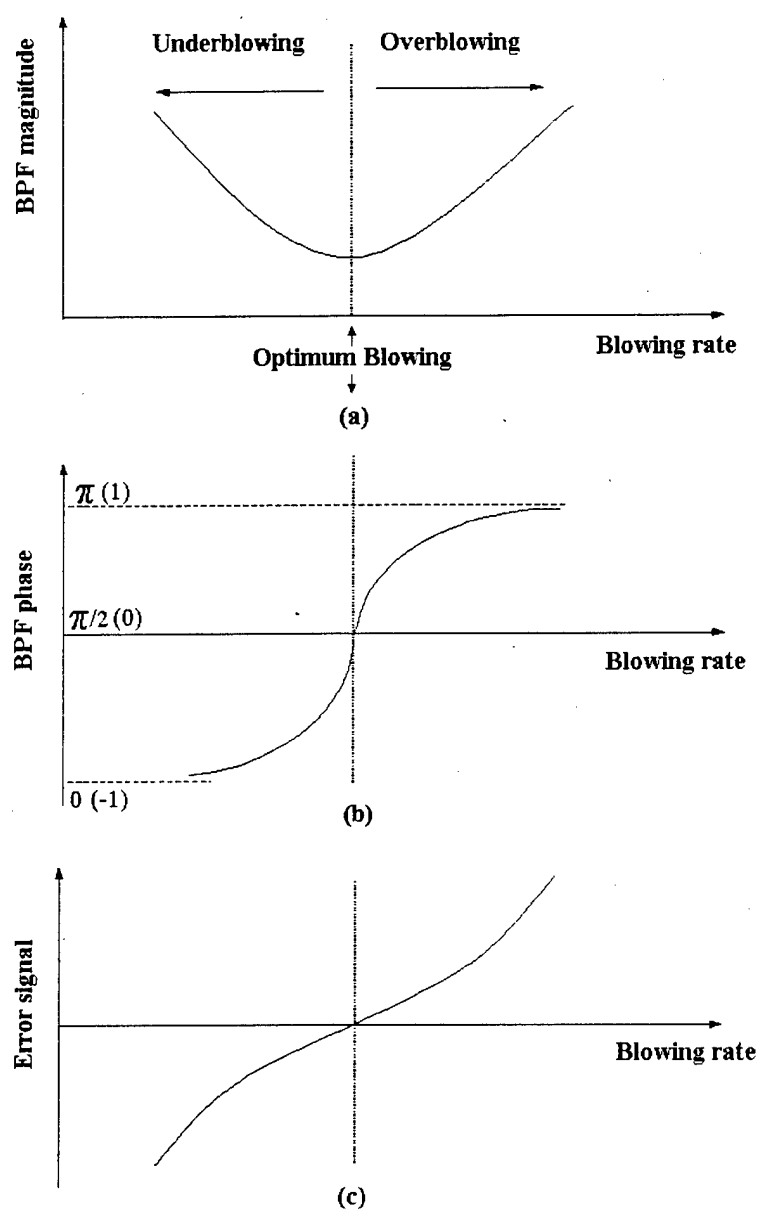
Figure 5.19: Schematic of (a) BPF tone magnitude, (b) BPF tone phase, and (c) PID error signal.
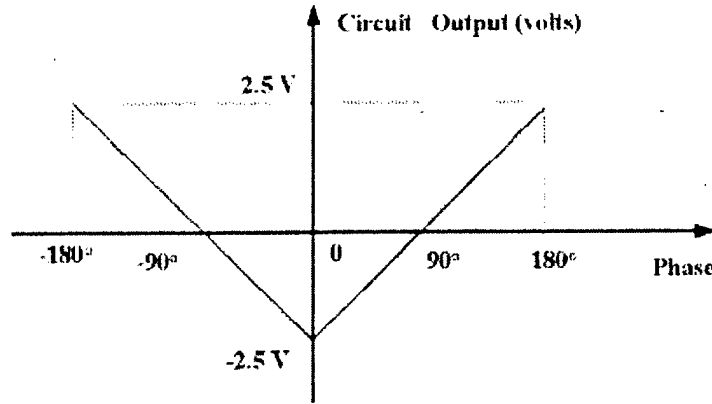
Figure 5.20: The characteristics of the phase detector.

part in this phase detector is an Exclusive-OR gate with the two TTL signals as inputs.

It is known that the output of an Exclusive-OR gate goes high when only one input

goes high, and the gate output remains at a logic low for all other inputs. Thus, it can

be shown that the mean value of the gate output, which can be obtained by a low pass

filter, exhibits a triangular function with respect to the phase difference between the

two TTL input signals. Appendix B has the details for the implementation of a phase

detector.

Both the magnitude and phase information for the BPF tone for each microphone is

input into the digital controller. The error signal for the PID controller is then obtained

as:

$$e_k = \sum_{i=1}^{4} b_i(k) * p_{(i)}(k)(-1)^i \qquad (5.4)$$

where $b_i(k)$ and $p_i(k)$ are the magnitude (RMS signal from the adaptive tone extractor device) and the relative phase (from the phase detector circuit) of the ith microphone ($i = 1,2,3,4$ in the azimuth order behind IGV A, B, C, D, respectively) at time t_k, respectively. It is important to mention that, in order for the control system to operate in the linear region of the curve shown in Figure 5.20, a phase shifter should be used for RPM signal so that the relative BPF tone phase in microphone 1 is set to zero for the no-blowing case. The term $(-1)^i$ in Eqn. (5.4) is included to account for the relative phase between microphone signals due to the acoustic modes generated by the IGV-rotor interaction. Since the 4 IGVs and the 18 fan blades excites the $m = 2$, -2, 6 and 10 circumferential propagating acoustic modes as shown in Table 3.6, adjacent microphones are out-of-phase. Thus without the term $(-1)^i$ in Eqn. (5.4), the error signal will vanish. Note that the error signal as obtained in Eqn. (5.4) serves the purpose of averaging the effect of the four wakes. This is convenient to account for variability in the trailing edge blowing between the IGVs. Another possible advantage of combining the error signals from the casing microphone as in Eqn. (5.4) is that the IGV-rotor interaction can be separated from the rotor-rotor and rotor-EGV interactions if they generate different m order circumferential acoustic modes. This will be further discussed in future work.
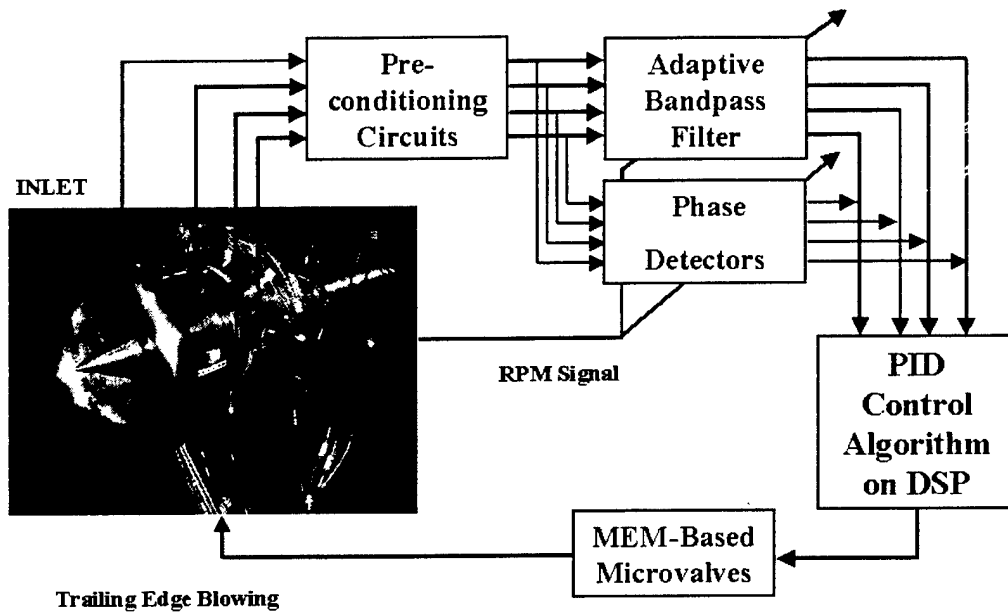
Figure 5.21: The block diagram for the control system using both BPF power and phase information.

Figure 5.21 shows the block diagram of the control system. Compared to the setup in the previous scheme, the phase detector has been added and the control algorithm is a feedback PID system. The inlet setup with four microphones flush mounted on the inlet casing remains unchanged.

Controller performance

This second control scheme was also tested in the anechoic chamber setup. The time
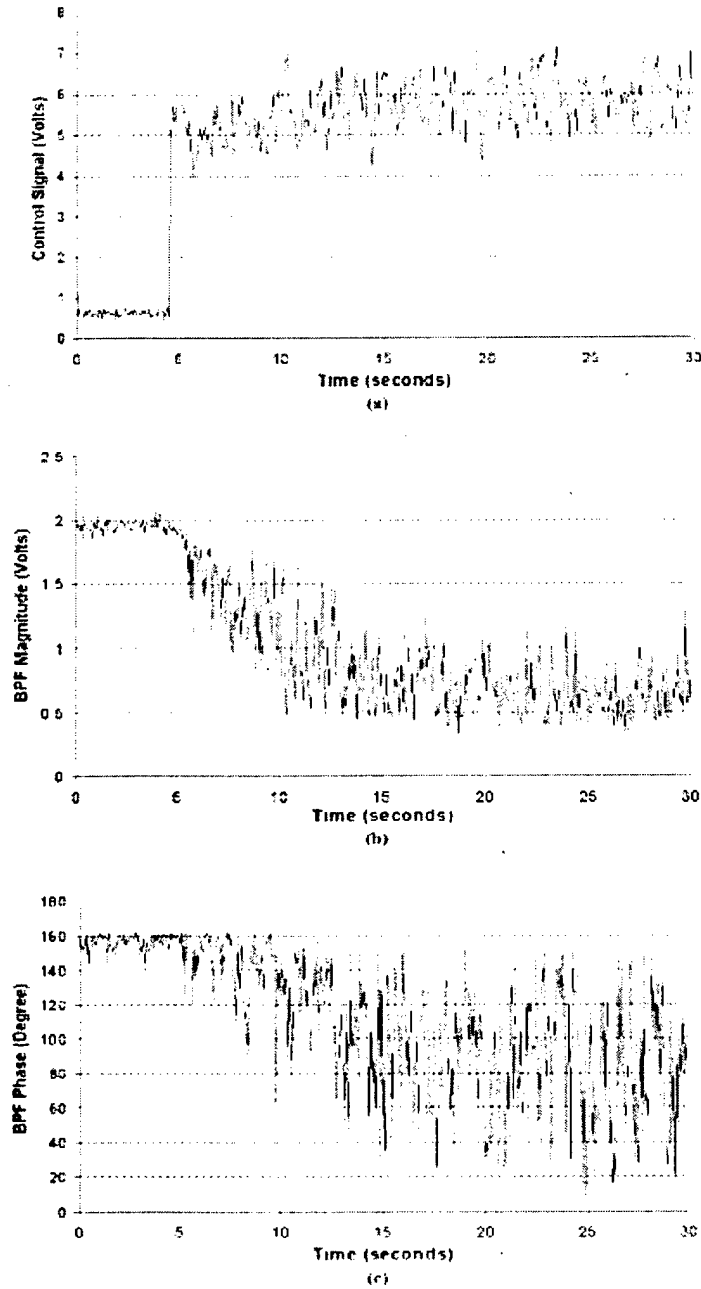
Figure 5.22: The time histories of (a) control, (b) BPF tone RMS, and (c) BPF tone

phase signals.

histories of the control, and the magnitude and phase of the error signals are recorded and they are shown in Figure 5.22. This figure shows the convergence process after the system is turned on at about 5 second. It can be found that the control signal converges to the steady state of 5.5 Volts in about 4 - 5 seconds. The BPF power is significantly reduced in about 4 seconds. Completed minimization is achieved in about 10 seconds. This result should be compared to about 40 seconds shown in Figure 5.12. It is also interesting to observe the real time error phase information from the output of the phase detector circuit shown in Figure 5.22c. Before the controller is turned on, the phase time history is stable with minimum variability. After the controller is turned on, as the error signal is minimized the phase goes, in an average sense, through a change of nearly 90° as expected from Figure 5.19b. Moreover. the phase also shows a significant increase in the variability. This can be explained using Figure 5.18 which shows an abrupt phase change near the optimum blowing rate. This indicates that a small deviation from the optimum blowing rate can cause the large change in the phase. In the real system, small deviations from the optimum blowing rate can always exist even though the control system has converged. As a matter of fact, the converged value just wanders around the "true" optimum value. In addition to that, inlet flow distortion due to the lack of an ICD could also be a cause since it is an unsteady process. These results clearly show that the main drawback, i.e. the slow time response, of the first control scheme was overcome in this new implementation.

The converged value of the control signal is compared to that obtained using the first controller developed above. Figure 5.12a shows the steady state value of 4.5 Volts of the control signal obtained by the first controller while the converged control signal from the second controller is about 5.5 Volts in Figure 5.22a. The 1-volt difference should be due to the flow condition changes as a result of slight physical difference in mounting the experimental setup for the two testing. The difference may come from the slight changes in the inlet duct axial and exhaust duct axial direction. Hence, for comparison purpose, the first controller is also tested on the same experimental setup here. The result for the converged control signal of about 5.5 Volts is illustrated in Figure 5.23. Therefore, it can be confirmed that the second controller does converge to the steady state value as the first controller did, leading to the optimum TEB blowing rate as well. The control signal in Figure 5.23 is not so "noisy" as compared to that in Figure 5.22a. This is because the control signal from the first controller is the time-averaged value with a period of 4 seconds. It can be expected that the control signal in Figure 5.22a would be similar to that in Figure 5.23 if it was also time-averaged with the same period of 4 seconds.

Acoustic Results

The acoustic data in the far-field and in the casing microphones are also recorded. The figures are not presented here since they are very similar to those obtained using the
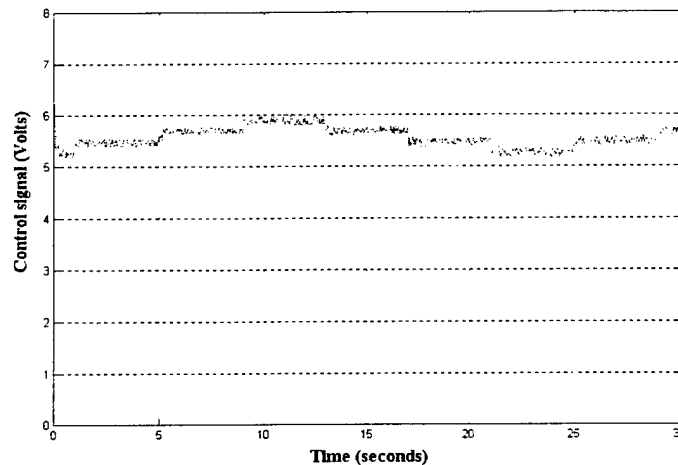
Figure 5.23: The steady-state control signal from the controller only using BPF magnitude.

first control scheme. The measured far field pressure at 20° after convergence shows a reduction of the BPF and 2BPF tones of 7.5 and 3 6 dB, respectively. In addition, about 7.0 dB noise reduction is observed at BPF in all the four casing microphones. These results again agree very well with the attenuation obtained using the Pitot probes.

Discussions and conclusions

The control scheme has demonstrated the much faster convergence rate as compared to the first controller due to the use of the PID controller. The error signal for the PID

controller can be formed because the additional information of BPF phase is utilized

besides the BPF magnitude. As a matter of fact, signal phase in many engineering

cases contains abundant information which can be employed in one way or another.

This is another excellent application case of making use of phase for a TEB control

system.

In addition to the much faster convergence rate, the control system can always converge

to the global optimum in the cost function shown in Figure 5.8. As mentioned earlier,

the BPF tone is usually so fluctuating that it can lead to some local minima in the cost

function. The worst case may cause the first controller converge to a local minimum

rather than the global minimum if the time-average period and step size in Equ. (5.2)

are not big enough. However, the local minimum in the cost function can does not

affect the convergence of the PID controller since the use of the BPF phase allows to

distinguish underblowing and overblowing conditions.

It is important to remark that this control approach works only at one engine speed.

The reason is because the phase reference signal, which is the rpm signal from the

magnetic pickup, varies in phase with the simulator speed. It follows that the BPF

tone phase relative to the rpm signal cannot be set to zero for all speeds in the noblow-

ing case once it is initialized to zero at one specific speed by the phase shifter. In

consequence, the phase detector cannot work in the linear region shown in Figure 5.20. One possible way to solve this problem is to conduct a phase survey in advance for all speeds providing the phase detector with a prior information. Apparently, this method is not practical. In the following, a new scheme is proposed and some preliminary experimental testing are conducted to attempt to resolve this problem.

The novelty of the proposed control scheme is to use the casing microphone signal, instead of the rpm signal, to serve as the phase reference, i.e., phase difference between adjacent casing microphones as depicted in Figure 5.24. The phase difference between
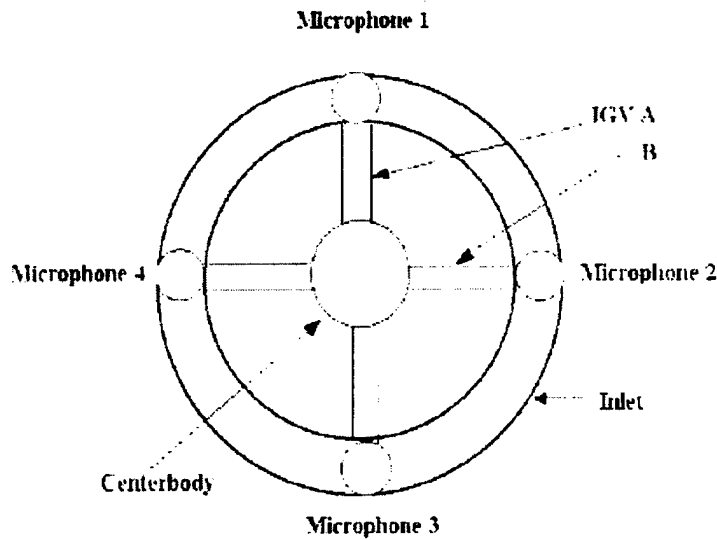
Figure 5.24: The casing microphones mounted on the inlet.

two adjacent microphones, $\Delta\Theta = \Theta(\frac{\pi}{2}) - \Theta(0)$ can be calculated out according to Eqn. (3.12) to be:

$$\Delta\Theta = [m\theta - 2\pi n N_B \Omega t/60 + \phi_{m\mu}]_{\theta=\frac{\pi}{2}} - [m\theta - 2\pi n N_B \Omega t/60 + \phi_{m\mu}]_{\theta=0} \quad (5.5)$$

$$= \pi \quad \text{for } m = \pm 2, \pm 6, \pm 10 \quad (5.6)$$

Note that the phase difference of π is obtained for all the circumferential modes $m = \pm 2, \pm 6$ and ± 10. Equation (5.6) clearly indicates that two adjacent microphone signals are out-of-phase. It is important to note that Eqn. (5.6) is independent of the simulator speed, Ω. It is this conclusion that provides the possibility to develop a new acoustic sensing approach which can work for a broad range of simulator speeds.

It is known from Figure 5.25a (the re-illustration of Figure 5.18), the BPF tone phase in microphone 2 changes from 180° to 0° as the TEB rate increase from underblowing to overblowing. Since microphone 1 is adjacent to microphone 2, the BPF Tone phase in microphone 1, as illustrated in Figure 5.25b, would change from 0° to 180° as TEB rate increases. This was also verified by the measurement results for microphone 1 as found in Table 5.1. Figure 5.25c is the differential of Figure 5.25a and Figure 5.25b. It is important to note that Figure 5.25c is independent of the simulator speed Ω, as evident in Eqn. (5.6). (The phase values in Figure 5.25a and Figure 5.25b were obtained using magnetic pickup signal as phase reference which would change with speed.) It follows
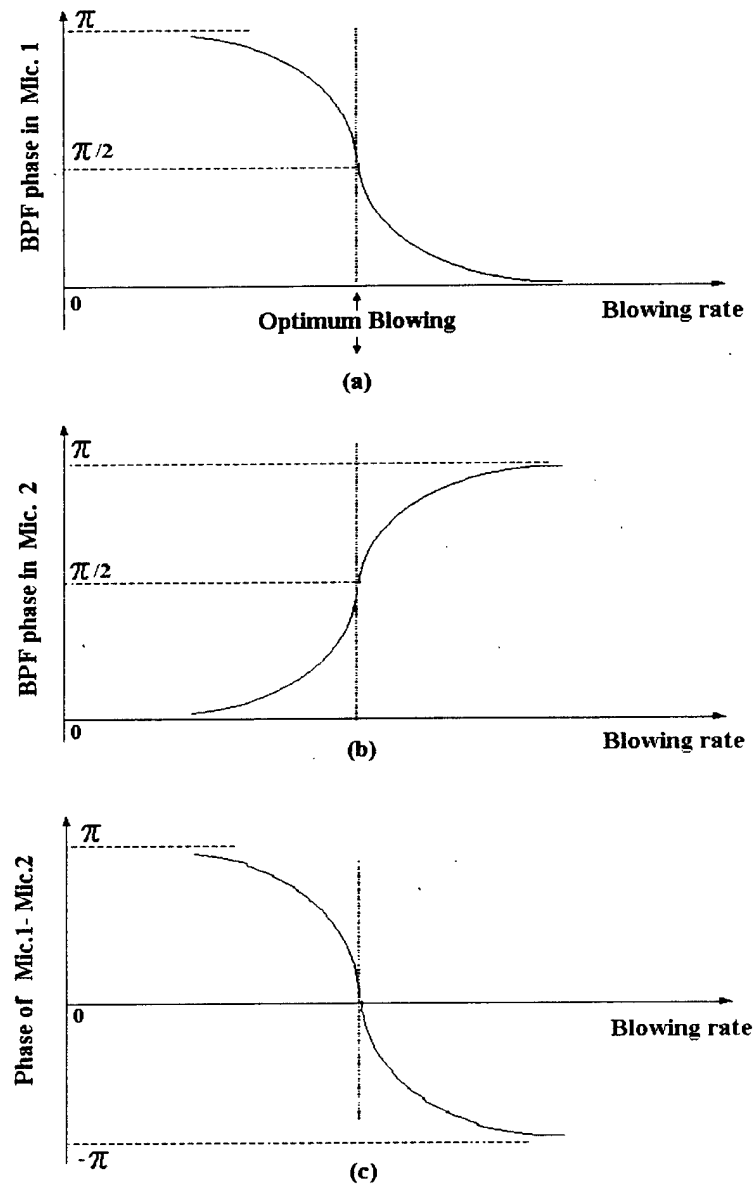
Figure 5.25: The BPF tone phase in (a) Microphone 1 referenced by rpm signal. (b) Microphone 2 reference by rpm signal and (c) Microphone 1 referenced by Microphone 2.

that Figure 5.25c can be used to replace Figure 5.19c in constructing a new error signal for the PID controller which now, however, could work for all simulator speeds.

Preliminary testing are performed to attempt to confirm the proposed idea. Tables 5.2 and 5.3 list the 10 measurements on the BPF tone phase of microphone 1 with microphone 2 signal as the reference without blowing and with overblowing, respectively. The overblowing is obtained by setting the blowing air pressure to 80 psi. The simulator speeds ranging from $20,000$ to $35,000$ rpm are tested. According to Eqn. (5.6) or Figure 5.25c, all the measurements are supposed to be around 180°. However, as shown in Tables 5.2 and 5.3, only the measurement results in the case of $30,000$ rpm are expected since they have a mean value of $\bar{\mu} = 166^o$ with a small standard deviation of $\tau = 8$ at no blowing, and $\bar{\mu} = 174$ with $\tau = 11$ at overblowing. The measurement results at the other speeds are not consistent. The phase differences between the adjacent microphones are not out-of-phase or / and exhibiting very large variances. The measurements on other two microphones, i.e., microphone 3 and microphone 4 demonstrate similar results as well.

These unexpected results are mainly due to the flow distortions ingested to the inlet because of the lack of an ICD. When interacted with the rotor blades, the flow distortion can also generate other circumferential acoustic modes in the inlet in addition to the

Table 5.2: Phase difference between two adjacent microphones without blowing.

RPM	Without Blowing						
	10 measurements					$\bar{\mu}$	τ
20,000	44	45	58	65	94		
	111	131	122	139	147	96	38
23,000	36	2	14	25	2		
	-73	103	-46	-77	-151	-17	68
25,000	29	15	-18	18	10		
	12	6	14	22	4	11	12
27,500	132	117	117	119	131		
	122	125	108	136	115	122	8
30,000	165	166	165	147	171		
	152	137	141	155	159	166	8
32,500	-42	40	-4	-15	-43		
	-81	-49	-52	-51	-51	-35	32
35,000	-16	-35	-5	-35	1.8		
	-15	0	-32	-35	-33	-20	15

Table 5.3: Phase difference between two adjacent microphones with overblowing.

RPM	With Overblowing						
	10 measurements					$\bar{\mu}$	τ
20,000	99	105	106	112	120		
	121	128	138	150	179	125	23
23,000	167	168	170	169	171		
	174	169	171	165	-170	171	7
25,000	-60	-64	-70	-79	-87		
	-114	-120	-110	-150	-164	-101	34
27,500	-128	-130	-131	-135	-136		
	-143	-155	-157	-161	-163	-143	13
30,000	144	166	-171	178	179		
	-177	179	176	173	175	174	11
32,500	158	-174	-168	-113	-136		
	-92	-92	-89	-76	-64	-120	45
35,000	99	110	110	110	114		
	125	127	129	134	128	118	11

modes induced by IGV-rotor interaction. This explains the deviations of the mean values from 180° in Tables 5.2 and 5.3. In addition, the flow distortion is an unsteady process which thus results in the large variance in the phase measurements. Another possible source for the unexpected results is IGV-rotor and rotor-EGV interactions. Although they are cut-off at the simulator speed tested, they can contribute to the output of near-field microphones as well. In Chapter 7, acoustic mode separation techniques will be proposed to filter out these disturbance modes so that only the modes induced by IGV-rotor interaction are extracted out. In addition, it is noted that the anticipated measurements obtained at 30,000 rpm in Tables 5.2 and 5.3 is probably because the IGV-rotor interaction happens to dominate among the other noise sources at this particular speed.

5.6 Summary

Two active TEB control systems with the non-intrusive acoustic sensing approach were successfully developed and tested on a turbofan simulator in the anechoic chamber. The non-intrusive casing microphones, which are compact and acceleration-compensated, proved to be performing very well in this application. The significance of using the

non-intrusive sensing technique in the control system lied in that it provided a more feasible way of wake-filling in the realistic engine environments.

The first control system used only the magnitude of the BPF tone to generate the error signal for the optimal controller. The system did converge to the optimum blowing, however, with a slow response of about 40 seconds. The slow response made the control system not practical for real applications. The second control system was developed to solve this limitation. The novelty of the second control system was the formation of the error signal for a PID controller. The phase signal of BPF can be used to distinguish between the underblowing or overblowing cases. The magnitude information of BPF tone was used as a weight which represents how far away the current blowing rate is from the optimum blowing rate. In doing so, a PID control algorithm could be used again. The convergence rate was accelerated by about 10 times as compared to the first controller.

A novel analog adaptive BPF power extractor was proposed in this chapter and employed successfully in the control systems. This extractor, the key technology to success, had the capability to extract the BPF tone or its harmonics adaptively from the microphone output when the simulator speed changed.

The acoustic results obtained from both systems. including far-field directivity and sound power reduction, agreed with those obtained in the probe-based experiments. In the first control system. the noise reduction of 7.9 dB was achieved in the far field. which was comparable with the 8.2 dB reduction with Pitot-probe based control system. The sound power level was reduced by 4.9 dB, which was close to the power reduction of 4.4 dB using Pitot probe as error sensors. Similar results were also obtained in the second control system. These results demonstrated the effectiveness and potential of this non-intrusive acoustic sensing strategy for active TEB.

The limitation of the second controller was that it could only work at one engine speed. This was because the phase reference, i.e., rpm signal from the magnetic pickup changed with the simulator speed. The new concept, which involved using adjacent microphone signal as phase reference. was attempted to solve this problem. However. it turned out that further work is needed to accomplish the goal.

Chapter 6

Analytical Prediction of Inlet

Sound Field

In Chapter 5 and Chapter 4, experimental studies were conducted to investigate TEB control using a small scale engine simulator. This chapter aims to conducting analytical studies on the active TEB using an existing aeroacoustic code. Results obtained from the studies are expected to provide the theoretical guidance for the development of more advanced experimental TEB control systems. In section 6.1, the objective of this

analytical work is introduced. A TEB model is proposed in section 6.2. Using the TEB model, the sound field prediction in the simulator inlet is conducted in section 6.3 by adapting the existing aeroacoustic CUP2D code.

6.1   Introduction

In Chapter 5. a microphone-based TEB control system was presented that made use of the BPF tone magnitude and phase to infer the wake-filling. However. the system has some drawbacks in terms of the response time or the effective working range in terms of simulator speed. More advanced acoustic sensing approaches, which could involve using the amplitude and phase of specific acoustic modes contributing to the BPF tone. may solve this problem. To this end, a clear understanding of inlet sound field with respect to TEB management becomes critical.

Such understanding will include the quantitative relationship of inlet sound field with respect to wake management approaches. More specifically. the objective of this chapter is to establish a tool to answer questions such as:

- How many acoustic modes in the inlet are significantly excited by IGV-rotor interaction? Mode separation techniques may be used in advanced acoustic sensing approaches to extract out these acoustic modes from other noise sources such as the rotor-EGV interaction. This may be required since a TEB control system only seeks to reduce IGV-rotor interaction, thus other noise sources are viewed as "disturbances" by the sensors of a control system.

- What is the effect of the jet-like wake-filling, commonly encountered in practice, in the inlet sound field?

- What is the effect of axial spacing between IGVs and rotors on inlet sound field with and without TEB?

In the following sections, two steps are taken to achieve the above objectives. The first step is to develop an analytical TEB model. The second step is to introduce this model into an existing aeroacoustics code to conduct inlet sound prediction studies of active TEB approaches in turbofan engines.

6.2 TEB Model Development

To the author's knowledge, this is the first research on the modeling of TEB model. Thus, the model development in this section may appear crude at first. However, it is the key first step to provide preliminary results and serve as a stepping stone towards more in-depth research in this field.

Before the development of the TEB model, several IGV pure wake models are studied in terms of their mass flow deficit and momentum flux deficit downstream the IGV. As the name suggests, mass flow rate is defined to be the time rate of mass flow, i.e., the product of flow density, velocity and cross-section area. Momentum flux is defined as the time rate of flow momentum per cross-section area, i.e., mass flow rate times flow velocity [55]. It is known that complete wake-filling implies that the wake momentum flux deficit and wake mass flow rate deficit are eliminated (i.e., momentumless wake). Therefore, these pure wake deficits should be first defined so that the required amount of blowing air can be determined to achieve a momentumless wake.

The physical features of the time averaged non-turning IGV wakes are characterized by measuring the semi-wake width δ, and the wake centerline velocity defect W_{dc} as
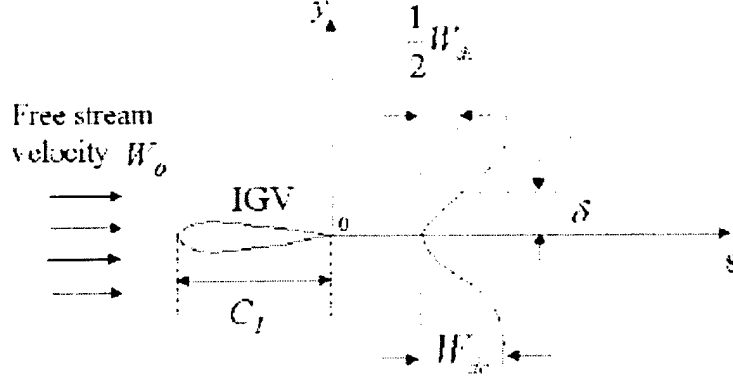
Figure 6.1: The parameters characterizing a pure wake velocity profile.

shown in Figure 6.1. Numerous empirical correlations have been developed for these

two quantities which quantify the physical nature of the wakes. Three models are

investigated here developed by Majjigi and Gliebe [63], Lakshminarayana and Davino

[64], and Silverstein, Katzoff and Bullivant [65], respectively. A pure wake model can

be expressed as:

$$W(y, s) = W_{dc}(s)e^{-0.693\left[\frac{y}{\delta(s)}\right]^2} \tag{6.1}$$

where $W(y, s)$ denotes the flow velocity in the IGV wake which is a function of pitchwise

distance y and streamwise distance from the IGV trailing edge, s.

The three models are now described in terms of the wake parameters $\delta(s)$ and $W_{dc}(s)$.

(a). <u>Majjigi-Gliebe pure wake model</u>:

For the Majjigi-Gliebe model, the wake parameters are defined by

$$\frac{\delta(s)}{C_I} = \frac{0.2375(s/C_I)C_D^{0.125} + 0.034125}{0.375(s/C_I)C_D^{0.125}} \tag{6.2}$$

$$\frac{W_{dc}(s)}{W_o} = C_D^{0.25}\frac{0.3675(s/C_I) + 1.95}{7.65(s/C_I) + 1.0} \tag{6.3}$$

where C_I is the IGV chord; C_D is the IGV drag coefficient; W_0 is the free stream velocity.

(b). Lakshminarayana-Davino pure wake model:

For the Lakshminarayana-Davino pure wake model, the wake parameters are given for two regions. For the near wake $(0.06 < s/C_I < 0.4)$, they are given by:

$$\frac{\delta(s)}{C_I} = \frac{0.695}{C_D^{0.5}}(s/C_I + 0.55)^{1.22} \tag{6.4}$$

$$\frac{W_{dc}(s)}{W_0} = \frac{0.168C_D^{0.5}}{(s/C_I + 0.12)^{0.22}} + \frac{0.353C_D^{0.5}}{(s/C_I + 0.12)^{0.22}} \tag{6.5}$$

and for the far wake $(s/C_I > 0.4)$, they are

$$\frac{\delta(s)}{C_I} = \frac{0.509(s/C_I)C_D^{0.5}}{s/C_I + 0.688} \tag{6.6}$$

$$\frac{W_{dc}(s)}{W_0} = \frac{0.9792C_D^{0.5}}{s/C_I + 0.688} \tag{6.7}$$

(c). Silverstein-Katzoff-Bullivant pure wake model

For the Silverstein-Katzoff-Bullivant model, the wake parameters are:

$$\frac{\delta(s)}{C_I} = \frac{1.21}{C_D^{0.5}}(s/C_I + 0.3) \tag{6.8}$$

$$\frac{W_{dc}(s)}{W_0} = 0.68 C_I \sqrt{C_D(s/C_I + 0.15)} \tag{6.9}$$

It is important to note that the three pure wake models above are developed in a 2-dimensional cascade model (i.e., y and s directions only). The normalized mass flow rate deficit, $\dot{m}_d$, and normalized momentum flux deficit, M_d, are computed and used to compare these models. The normalized mass flow rate deficit and normalized momentum flux deficit are defined as

$$\dot{m}_d = \int_{-\infty}^{\infty} \left[\frac{W_0 - W(y,s)}{W_0}\right] dy \tag{6.10}$$

$$M_d = \int_{-\infty}^{\infty} \left[\frac{W_0^2 - W^2(y,s)}{W_0^2}\right] dy \tag{6.11}$$

The computed mass flow rate and momentum flux deficits are presented in Figure 6.2 and 6.3, respectively. These results indicate that only the Lakshminarayana-Davino model conserve both the mass flow rate and momentum-flux deficits streamwise in the far wake downstream the IGV. The deficits for the Majjigi-Gliebe and Silverstein-Katzoff-Bullivant models are decaying streamwise. Therefore, the far wake Lakshminarayana-Davino model is used in developing the active TEB model in the following since it states unequivocally the required amount of blowing air to achieve a

momentumless wake.

A model for the TEB is now proposed. It is assumed here that the TEB velocity profile can be represented as

$$W^T(y, s) = -W_{dc}^T(s) \cdot e^{-0.693\left[\frac{y}{\delta^T(s)}\right]^2} \qquad (6.12)$$

where the parameters $\delta^T(s)$ and $W_{dc}^T(s)$ define the jet width and depth, respectively. It is further proposed that these parameters can be expressed as proportional to the pure wake width $\delta(s)$ and depth $W_{dc}(s)$. That is:

$$\delta^T(s) = a_0 \cdot \delta(s) \qquad (6.13)$$

$$W_{dc}^T(s) = b_0 \cdot W_{dc}(s) \qquad (6.14)$$

where $\delta(s)$ and $W_{dc}(s)$ can be found from Eqn. (6.6) and (6.7). The proportionality coefficients a_0 and b_0 are the width and depth scaling factors. It is noted that the TEB jet width and depth have the same decaying rate along s-direction as those of the Lakshminarayana-Davino far wake. Therefore, as in this Lakshminarayana-Davino far wake model, mass flow rate in the TEB jet model is also conserved downstream the IGV. This conservation of the model is important since the mass flow rate downstream should be constant in real cases. In practice, the value for the width scaling factor, a_0 should be determined by the TEB physical geometry such as hole diameter, number, location etc. The depth scaling factor, b_0 can be determined by the given TEB mass
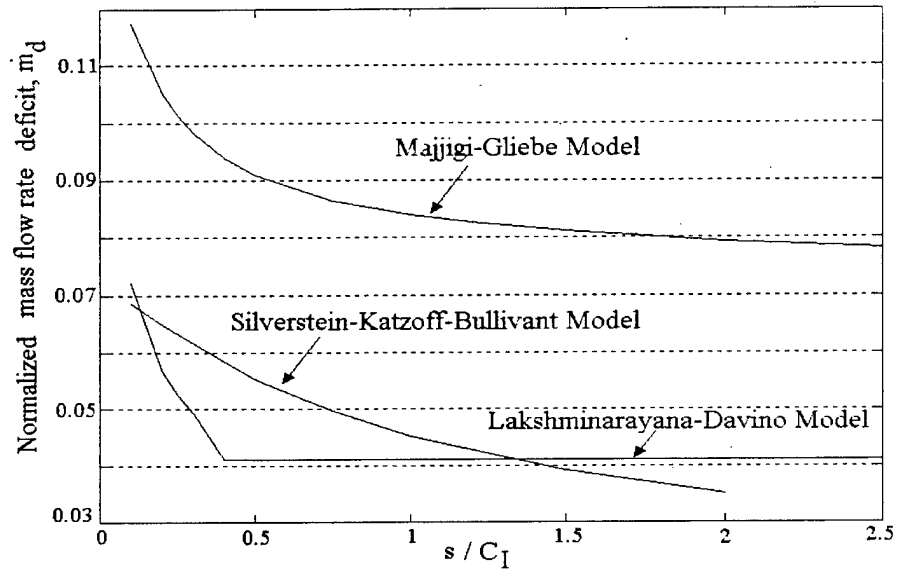
Figure 6.2: Normalized mass flow rate deficit of the pure wake models.
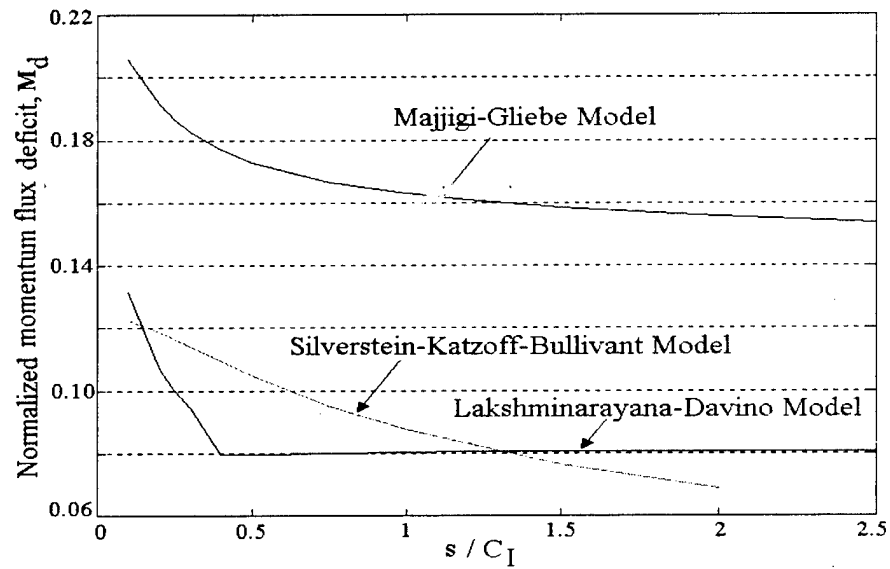
Figure 6.3: Normalized momentum flux deficit of the pure wake models.

flow rate, $\dot{m}^T$, once a_0 is known. This is because b_0 along with a_0 determines $\dot{m}^T$ as

$$\dot{m}^T = \rho \int_{-\infty}^{\infty} W^T(y,s)dy \tag{6.15}$$

$$= \rho \int_{-\infty}^{\infty} b_0 W_{dc}(s) e^{-\frac{0.693y^2}{a_0^2\delta^2(s)}} dy \tag{6.16}$$

where ρ is the fluid density. Equation (6.16) is obtained by substituting Eqn. (6.13) and (6.14) into Eqn. (6.12).

The mixed flow velocity, i.e., wake and TEB velocities, $W_{mix}(y,s)$ is then obtained through a linear summation of the pure wake flow and TEB jet velocities as

$$W_{mix}(y,s) = W(y,s) + W^T(y,s) \tag{6.17}$$

Although the actual jet mixing process is much more complicated than a linear summation [58], Eqn. (6.17) provides a simple model for analytical studies which, however, does not violate any fluid laws. It should be noted that the linear summation in Equation 6.17 satisfies mass flow rate conservation if incompressible flow (usually Mach number less than 0.65) is assumed. This condition holds in this research since the inlet flow Mach number in the tests is about 0.3. This is important since the aeroacoustics analysis to be conducted in the latter part of this chapter will focus on the studies of inlet sound pressure with relation to the TEB mass flow rate.

A comparison is made with reported experimental results to validate this model. According to the experimental work by Park, etc [22, 23], the mixed flow velocity in the momentumless wake case was found to be "self-similar" downstream the IGV, i.e., normalized velocity profiles for a momentumless wake at different streamwise distances collapsed into a single curve. The normalization factors, i.e., the overshoot H and the spread L which usually quantify a "jet-like" wake-filling profile, are described in Figure 6.4 which is an example of a momentumless wake velocity profile at 0.75 IGV chord downstream with $a_0 = 0.707$ and $b_0 = 1.414$ used in Eqn. (6.17). The pitchwise distance is normalized by the IGV thickness while the flow velocity is normalized by the free stream velocity. For comparison purposes, the pure wake velocity profile of the Lakshminarayana-Davino model is also shown in Figure 6.4. Using the normalization factors H's and L's as indicated in Figure 6.4, obtained from the momentumless wake profiles at each of the downstream locations of $s/C_I = 0.5$, 0.75, 1.0 and 1.5, the normalized momentumless wake profiles at these axial locations are shown in Figure 6.5. As seen, the mixed flow velocity in the momentumless wake case is exactly "self-similar" as expected. In addition, the decaying rate of H and L along streamwise is also computed to be $(s/C_I)^{-0.56}$ and $(s/C_I)^{0.56}$, respectively, which should be compared to $(s/C_I)^{-0.92}$ and $(s/C_I)^{0.3}$ reported in references [22, 23]. These results show that the model for TEB proposed here agrees well with the experimental results presented in the literature [22, 23]. Thus, this comparison provides some degree of confidence in

the model to conduct sound prediction in the next section.

6.3 Sound Field Prediction in Simulator Inlet

6.3.1 CUP2D with active TEB

The aeroacoustics code used in inlet sound pressure prediction is the code referred to as CUP2D developed by D. Hanson [48]. This code considers a typical 2D cascade model for stator/rotor interaction as sketched in Figure 6.6. Either blade row can rotate in either direction. As the free stream passes through the first row. the wake is generated which imposes on the second row blades leading to the unsteady loading. The unsteady loading on the blades, when coupled with the fluid, results in the sound generation. The CUP2D code is capable of predicting inlet sound field upstream the first row, in between two rows, and downstream row. Compared to the previously existing codes [66], CUP2D presents a more complete 2D cascade analysis in which flow tangency boundary conditions are satisfied on the two cascades in relative motion for several harmonics simultaneously. The new features of the code include unsteady coupling,
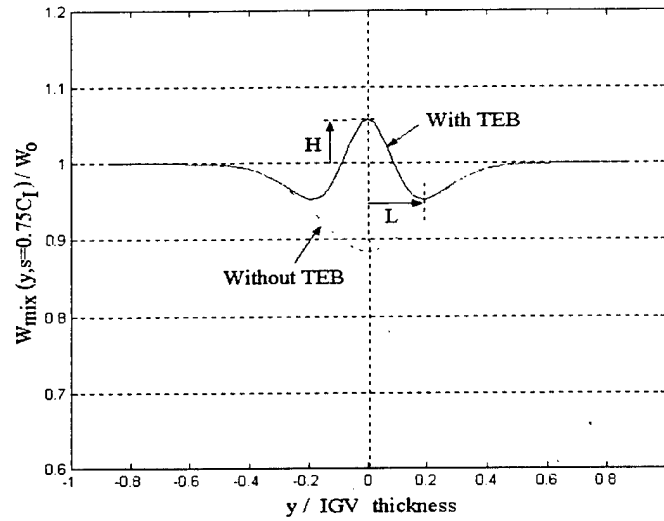
Figure 6.4: A momentumless wake velocity profile ($a_0=0.707$ and $b_0=1.414$).
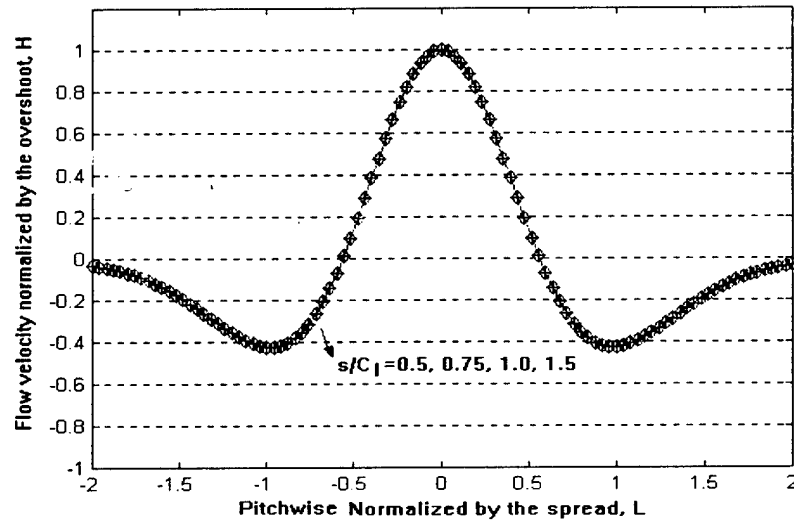
Figure 6.5: Normalized momentumless wake profile ($a_0=0.707$, $b_0=1.414$).
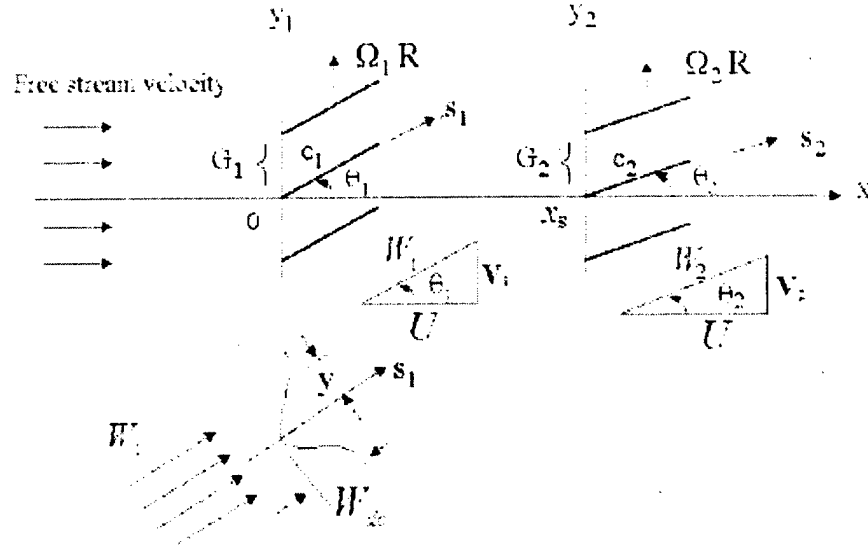
Figure 6.6: The 2D flat plate model.

frequency scattering, and flow turning between first and second row.

The physical parameters characterizing the 2D cascade model, which are required to input to CUP2D, are now described. The effective fan radius R, which is the important parameter in converting a real 3D stator-rotor configuration into a 2D cascade model, is assumed to be 85% the actual fan radius; B_1 is the blade number in the first row with a rotating speed of Ω_1 while the second row has B_2 blades rotating at speed Ω_2; the blade chords of the first and second row are defined by C_1 and C_2, respectively; y_1 and y_2 are the translational moving direction for the two rows; s_1 and s_2 are the

streamwise coordinates along the blades; U is the axial flow velocity; V_1 and V_2 are the swirl flow velocities while W_1 and W_2 represent the velocities along s_1 and s_2 direction, respectively; x_s is the axial spacing between the rows; θ_1 and θ_2 are the blade angles of the first and second row; and G_1 and G_2 are the blade gaps.

It is important to note that the code uses the Silverstein-Katzoff-Bullivant pure wake model for the first row [65]. In addition, the code utilizes the Fourier integral coefficients of the pure wake model rather than the model equation itself.

The existing CUP2D should be adapted so that it can be used in this research. First, the Silverstein-Katzoff-Bullivant pure wake model should be replaced by the Lakshminarayana-Davino model since the latter presents a more reasonable wake profile for TEB studies, i.e., mass flow rate conserved. It follows that the Fourier coefficients of the Lakshminarayana-Davino model should be the derived. The second adaptation is that the TEB model should be introduced into the CUP2D code. Similarly, the Fourier coefficients of TEB should be found. Appendix C has more details regarding the code adaptation. As a brief summary, the Fourier coefficients of the

Lakshminarayana-Davino pure wake model are found to be:

$$F_n(s_1) = \frac{2\sqrt{\pi}}{Q} \cdot \frac{W_{dc}(s_1)}{W_1} \exp\left[-\left(\frac{\pi n}{Q}\right)^2\right] \exp\left(\frac{inB_1[-s_2 sin(\theta_1 - \theta_2) + x_s sin\theta_1]}{cos\theta_1}\right)$$

(6.18)

where,

$$Q = \frac{\sqrt{\pi}G_1 cos\theta_1}{2.13\delta(s_1)}$$

(6.19)

In addition, the Fourier coefficients associated with the TEB jet are obtained as:

$$F_n^T(s_1) = \frac{2\sqrt{\pi}}{Q^T} \cdot \frac{W_{dc}^T(s_1)}{W_1} \cdot \exp\left[-\left(\frac{\pi n}{Q^T}\right)^2\right] \exp\left(\frac{inB_1[-s_2 sin(\theta_1 - \theta_2) + x_s sin\theta_1]}{cos\theta_1}\right)$$

(6.20)

where,

$$Q^T = \frac{\sqrt{\pi}G_1 cos\theta_1}{2.13a_0\delta(s_1)}$$

(6.21)

$$W_{dc}^T(s_1) = b_0 \cdot W_{dc}(s_1)$$

(6.22)

These Fourier coefficients in Eqn. (6.18) and Eqn. (6.20) need to be input to the subroutine GTWAKE in CUP2D.

6.3.2 Prediction results in simulator inlet

This section uses the adapted CUP2D code to analyze the simulator running at 30,000 rpm which was one of the test speeds in Chapters 4 and 5. As mentioned earlier, the

prediction results are expected to provide an insight on the quantitative relationship between the inlet sound field and TEB in terms of mass flow rate and wake-filling shape (i.e., jet-like shape), and on the effect of the axial IGV-rotor spacings. The acoustic information obtained would be helpful in developing more advanced microphone-based controllers. In addition, the results are also expected to provide some guidance to the design of TEB configurations like the number of holes, hole size, and so forth.

Figure 6.7 shows the schematic diagram of the 2D cascade model for the simulator. As compared to Figure 6.6, the first row here is the IGVs and the second row is the rotor. In addition, the swirl flow velocity in between IGVs and rotor is zero (i.e., $V_1 = 0$ and $\theta_1 = 0$ in Figure 6.6 or $M_{t_1} = 0$ in Figure 6.7) since the non-turning IGVs are used; M_{xa}, A_a and ρ_a represent the flow axial Mach number, sound speed and fluid density in the region upstream of the IGV; the subscripts a, b and c denote the region upstream IGV, in between IGV and rotor, and downstream rotor, respectively; M_{t_1} and M_{t_2} are the swirl Mach numbers. The values of these parameters at the simulator speed of 30,000 rpm are listed in Table 6.1. The detailed derivation of these values can be found in Appendix D. Using the information provided by the table, the inlet sound pressure level in the location of inlet microphones with and without TEB is then predicted using CUP2D.

Table 6.1: The input parameters for CUP2D when the simulator runs at 30k rpm.

number of IGV (B_1)	:	4
number of rotor blades (B_2)	:	18
Axial Mach number upstream IGV (M_{xa})	:	0.3
Axial Mach number between IGV and rotor (M_{xb})	:	0.3
Axial Mach number downstream rotor (M_{xc})	:	0.6
Swirl Mach number between IGV and rotor (M_{V_1})	:	0.0
Swirl Mach number downstream rotor (M_{V_2})	:	0.6
Translational Mach number of the 1st row (M_{y1})	:	0.0
Translational Mach number of the 2nd row (M_{y2})	:	0.405
IGV gap/chord ratio (G_1/C_1)	:	1.31
rotor gap/chord ratio (G_2/C_2)	:	0.74
normalized axial spacing between IGV and rotor (X_s/R)	:	2.395
sound speed upstream IGV (A_a)	:	1127.6 feet/second
sound speed between IGV and rotor (A_b)	:	1127.6 *feet/second*
sound speed downstream rotor (A_c)	:	1141.1 *feet/second*
density upstream IGV (ρ_a)	:	0.0702 *lbm/feet*^{3}
density between IGV and rotor (ρ_b)	:	0.0702 *lbm/feet*^{3}
density downstream rotor (ρ_c)	:	0.0674 *lbm/feet*^{3}
normalized axial location for SPL printout X_a/R	:	1.79
drag coefficient C_D	:	0.01

Figure 6.7: Schematic digram of the 2D cascade model for the simulator.

Baseline results
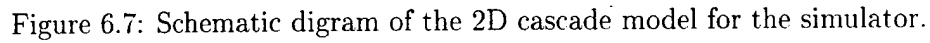
The baseline case (i.e. without TEB) is first calculated. The CUP2D output at BPF and 2BPF at the inlet microphone locations is shown in Table 6.2. Note that the code output does not contain any information of mode radial order since radial uniformity is assumed in the 2D-cascade model. The first observation from the table is that BPF tone dominates the inlet sound field. The BPF tone is about 50 dB louder than that at 2BPF tone. Furthermore, the circumferential mode $m = 2$ dominates the BPF tone. The second most significant mode at BPF is $m = 6$ which is 27 dB quieter as compared to that of $m = 2$. Therefore, the code predicts that IGV-rotor interaction primarily generates $m = 2$ modes. This information is very valuable when designing advanced microphone-based TEB control systems. As mentioned before, BPF tone sensed by inlet near-field microphones are due to IGV-rotor, rotor-rotor and rotor-EGV interactions, and inlet flow distortion. The sound prediction result here suggests

Table 6.2: The CUP2D output at BPF and 2BPF tones.

BPF		2BPF	
circumferential mode	SPL	circumferential mode	SPL
m=2	132.2 dB	m=8	82.6 dB
m=6	105.2 dB	m=4	43.3 dB
m=-10	82.2 dB		
m=-14	43.4 dB		
Total: 132.2 dB		Total: 82.6 dB	

that IGV-rotor interaction can be separated from other noise sources by extracting out only $m = 2$ modes. (assume that the other two noise sources generate different circumferential modes). Design of advanced microphone-based systems using mode separation technique will be discussed in the next chapter as a future work.

As an additional note. it is worth to point out that the absolute SPL (i.e., 133.2 dB) from the prediction is comparable to that obtained from the experimental simulator testing (i.e., 128 dB in Figure 5.15). which gives some degree of confidence of using CUP2D in the analytical studies of this chapter. However, it is important to note that the code greatly under-predicts the 2BPF tone level.
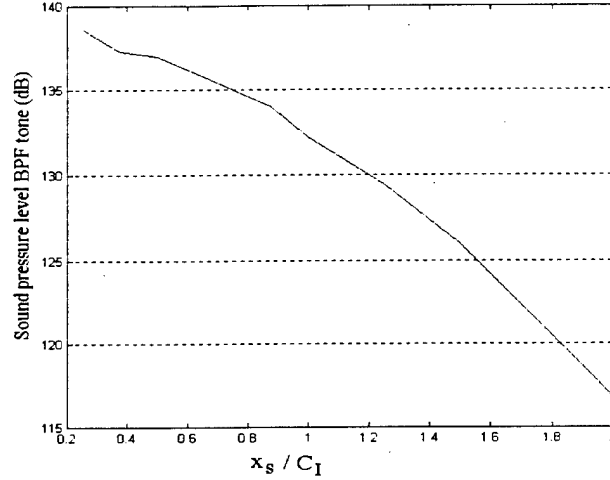
Figure 6.8: The inlet sound pressure level with respect to IGV-rotor axial spacing.

The effect of the axial spacing X_s on inlet sound field is also investigated here without TEB. The axial spacing is one of the major design specifications for modern turbofan engines. Therefore, it is important to take into account the axial spacing effect when designing acoustic sensing approach for TEB control. Figure 6.8 depicts the results. Note that the SPL value for mode $m = 2$ is used to represent the pressure level at BPF tone since $m = 2$ mode dominates all other modes. The y-axis is the pressure level at BPF in the inlet microphone locations; x-axis is the axial spacing between IGV and rotor normalized by IGV chord. The figure shows that the pressure level decreases as the axial spacing increases. This result agrees with those reported in the literature [15].

BPF tone reduction versus TEB mass flow rate and wake-filling shape

The wake-filling shapes studied here are obtained by varying a_0 in the active TEB model. According to Eqn. (6.13), a small value for a_0 would lead to a narrow TEB jet while a large value for a_0 means a wide jet. Figure 6.9 shows several wake-filling shapes at simulator fan face (i.e., one IGV chord downstream) in the cases of $a_0 = 0.3$, 0.5, 0.707 and 0.9.

Figure 6.10 illustrates the BPF tone reduction resulted from these wake-filling shapes shown in Figure 6.9. The horizontal axis is the TEB mass flow rate normalized by the pure wake mass flow rate deficit. So a value of 1.0 refers to the amount of mass flow rate which leads to the momentumless wake. As indicated, the maximum noise reductions (i.e., the peaks in Figure 6.10) do not occur at the momentumless wake if the wake-filling shape is "jet-like". The closer to the pure wake width the TEB jet width is, the closer to the momentumless wake the peak approaches. The importance of this conclusion lies in that it warns that the TEB hole size should be designed such that the jet width should be as close as possible to the pure wake width. In doing so, the maximum sound pressure reduction can serve as the exact acoustic indicator to a momentumless wake. Such design would also leads to the largest amount of sound pressure reduction (see the peaks in Figure 6.10, around 28 dB for the case of $a_0 = 0.9$ while only 15 dB for $a_0 = 0.3$). From another viewpoint, the conclusion warns that

more mass flow rate is actually needed to achieve a momentumless wake in a converged microphone-based TEB control system where the maximum sound pressure reduction is used to infer the jet-like wake-filling.

The effect of axial spacing on TEB

The effect of the IGV-rotor axial spacing on active TEB in terms of the inlet sound pressure is also examined. Three cases of $X_s = 0.5, 0.75$ and 1.0 IGV chord are studied. Figure 6.11 shows the results when the jet width is that of $a_0 = 0.5$. It indicates that sound pressure reduction increases with X_s, given the same amount of TEB mass flow rate(when < 0.6). For instance, if a limited amount of TEB mass flow rate is available. e.g. 0.5, a reduction of 15 dB is achieved in the case of $X_s = 1.0$ IGV chord while only about 8 dB is obtained in $X_s = 0.5$ IGV chord. The second observation from the figure is that the peak gets closer to the solid vertical line (i.e., the momentumless wake) as the axial spacing decreases. It implies that if the maximum sound reduction in the inlet is employed as an indicator to infer a momentumless wake as did in the optimal controller in Chapter 5, it would work better in the smaller spacing X_s.
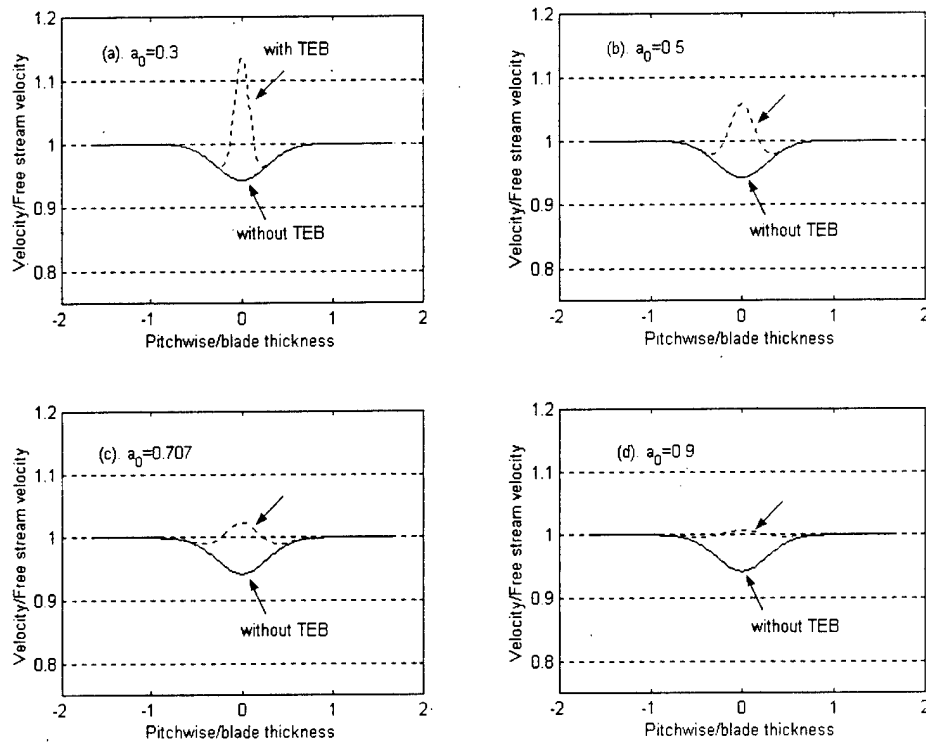
Figure 6.9: The four momentumless wake-filling shapes.
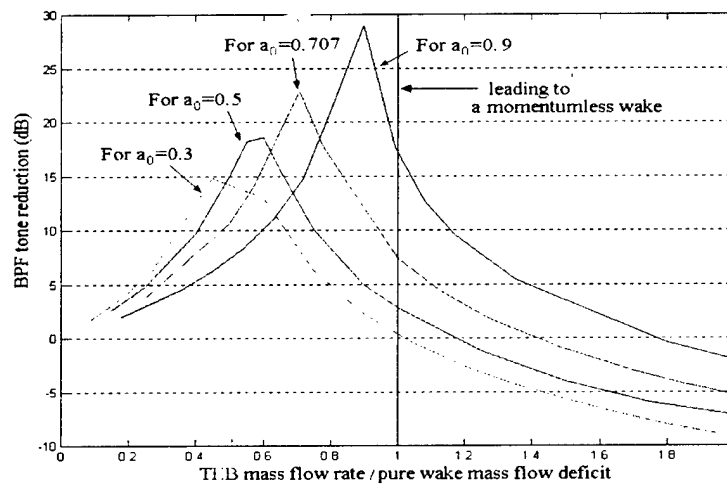
Figure 6.10: BPF tone reduction in the four wake-filling cases.
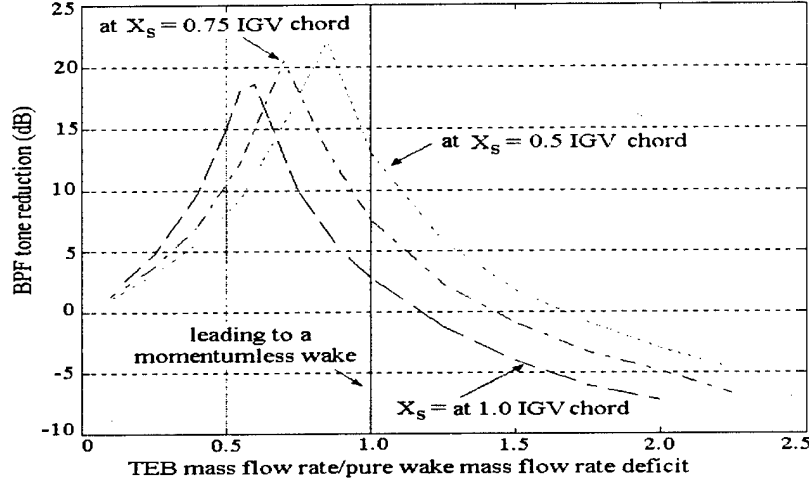
Figure 6.11: Noise Reduction with TEB mass flow rate.

6.4 Summary

This chapter conducted analytical studies on the active TEB and sound prediction
using CUP2D. In the first part of the chapter, an analytical model for TEB was pre-
sented which was based on Lakshminarayana-Davino pure wake model. The active
TEB model was mass flow rate conserved. In addition, the momentumless wake pro-
files were self-similar downstream of the IGV. This result agreed with the experimental
results obtained from Park[22, 23]. The second part of the chapter was devoted to
the analytical predictions of inlet sound pressure using an adapted CUP2D code. The
adaptation of the CUP2D code consisted of two steps. First, FFT coefficients for the

Lakshminarayana-Davino pure wake model were computed to replace the Silverstein model which was originally used in CUP2D. Second, the active TEB was introduced into the CUP2D code.

The simulator at a rotating speed of 30,000 rpm was analyzed. The effects of "jet-like" wake profiles on inlet sound field and IGV-rotor axial spacings on active TEB were examined. It was found that maximum sound pressure reductions do not occur at the momentumless wakes if the wake profiles are "jet-like". More blowing air than the amount which caused maximum sound reduction was needed to achieve a momentumless wake. The analysis also warned that TEB holes should be such designed that the jet width approaches the pure wake width as possible. The investigation on the IGV-rotor axial spacing effects on active TEB and inlet sound field demonstrated that a larger spacing would lead to a larger inlet sound reduction using a limited amount of blowing air.

Chapter 7

Conclusions and Future Work

The TEB control systems using different sensing approaches are summarized and main conclusions of the research are drawn in this chapter. Future work is also discussed. It includes improvements of the acoustic sensing approaches and development of other practical sensing techniques.

7.1 Conclusions

To the author's knowledge, this was the first research effort to conduct studies on the feasibility of employing active TEB control to reduce stator-rotor interaction and the associated HCF damage in blades. Active flow control systems with different wake sensing approaches had been successfully implemented in the simulated engine environment.

The Pitot-probe based flow control system was developed and implemented as a first step toward more in depth investigations of active TEB. A PID controller was used to generate control signal for MEMS-based microvalves to adjust the TEB rate. Results had shown that the control system produced a very uniform flow field downstream of the IGV in a rotating environment. The ability of the system to achieve effective wake filling when subjected to a change in inlet flow conditions demonstrated the feasibility and advantage of active flow control. It was also demonstrated that far-field sound pressure levels at BPF tone were reduced by TEB. The maximum tone reduction obtained was 8.2 dB at 30,000 rpm and 7.3 dB at 40,000 rpm. Sound power level at the BPF tone was reduced by 4.4 dB at 30.000 rpm and 2.9 dB at 40.000 rpm. respectively.

Another significant contribution of this dissertation lied in the microphone-based controller which provided a potential practical TEB approach for the implementation in realistic engines. Microphones were flush mounted near the rotor behind the IGV's to sense the tonal noise at BPF. In the first control scheme, optimum control algorithm was used to find the optimum blowing rate by searching for the minimum of the BPF magnitude. However, this approach had several drawbacks with the main one to be the slow time response of the system, i.e., about 40 seconds to converge to the optimum. The novelty of the second control scheme was using both the BPF tone magnitude and phase to form the error signal for a PID controller. The phase information of the BPF tone was used to distinguish between the underblowing or overblowing cases. The convergence rate was accelerated by about another order of magnitude as compared to the first controller. The acoustic results obtained from both schemes, including far-field directivity and sound power reduction, agreed well with those obtained in the Pitot-probe based experiments. The maximum noise reduction of 7.9 dB was achieved in the far field and the sound power level was reduced by 4.9 dB. These results demonstrated the effectiveness and potential of this non-intrusive acoustic sensing strategy for active TEB. It is also worth to mention that a novel analog adaptive BPF power extractor was proposed and employed successfully in the control systems.

Preliminary analytical studies were also conducted on the modeling of TEB. An ana-

lytical model for TEB was first proposed based on Lakshminarayana-Davino pure wake model. The momentumless wake profiles computed from this mass flow rate conserved model were self-similar downstream of the IGV. The TEB model was then introduced into a 2D aeroacoustic code to investigate effect of TEB in the tonal sound generation. The effects of double-hump wake profiles on the inlet sound field were then examined. A key result showed that more blowing air than the amount leading to maximum noise reduction was actually needed to achieve a momentumless wake in a converged microphone-based control system, if the filled wake profile had a double-hump shape.

7.2   Future Work

Since active TEB research is still in its first stage, it is far from being well-developed for practical implementations. It needs further investigations and analyses. In this section, a potential improvement on the TEB controller with acoustic sensing approach will be first discussed. Then, the future work including other sensing approaches will be addressed.

As the first recommendation, an inlet flow control device (ICD) should be used in the

experiments. The purpose of the ICD is to minimize the spurious effects of ground testing on acoustic measurements by breaking up incoming vortices and eliminating inlet flow distortions. As stated before, the lack of the ICD has the adverse effects on the acoustic sensing approaches developed in Chapter 5. These effects include the severe fluctuation in both BPF tone magnitude and phase. Use of the ICD would bring an immediate benefit to the TEB control systems developed in Chapter 5. i.e.. the system response of the first controller can speed up by reducing the average time while the BPF tone phase signal in the second controller would exhibit less variability.

The second recommendation involves using a mode extraction technique for advanced acoustic sensing approaches to separate IGV-rotor interaction from other noise sources. This mode separation technique would help improve the second controller in Chapter 5 so that it could work for all simulator speed. As described at the end of Chapter 5, a new control algorithm was attempted to improve the second controller. However, the preliminary testing results were not successful. This is because the sound field in the inlet is generated not only by IGV-rotor interaction but by other noise sources such as rotor-rotor, rotor-EGV interactions, and inlet flow distortion.

The basic idea of mode separation technique is to perform wavenumber transform using an array of casing microphones to extract out the *mode amplitude* and *phase* of the

significant acoustic modes induced by the IGV-rotor interaction. These significant acoustic modes induced by IGV-rotor interaction can be obtained from the analytical prediction of the aeroacoustic code CUP2D. An array of casing microphones provides the spatial information of the inlet sound field while the wavenumber transform can be viewed as a technique to design "a spatial-domain digital filter" as compared to the regular Fourier transform to design "a time-domain digital filter". In the following, use of a circular microphone array is briefly described. The purpose here is to introduce the mode separation concept instead of the implementation details, i.e., a stepping stone toward further investigation.

In order to extract out the circumferential mode m, a circular array of N_c microphones is placed circumferentially on the inlet case as shown in Figure 7.1. If the nth microphone signal is denoted as $r(n)$ $(n = 0, 1, 2, \cdots, N_c)$, the discrete wavenumber transform in the azimuth direction can be expressed as

$$e(\Delta\phi) = \sum_{n=0}^{N_c-1} r(n)e^{-jn\Delta\phi} \qquad (7.1)$$

where $j = \sqrt{-1}$; $\Delta\phi$, which is equal to $\frac{2\pi m}{N_c}$, is the phase delay applied to the microphones to extract the circumferential mode m; The complex wavenumber coefficient $e(\Delta\phi)$, which is referred as the error signal for control systems, can be written in the form of $e(\Delta\phi)=|e(\Delta\phi)|\angle e(\Delta\phi)$, where $|e(\Delta\phi)|$ is the mode amplitude and $\angle e(\Delta\phi)$ is

Bellmouth

Centerbody

Inlet wall

IGV

Circumferential Array of Microphones
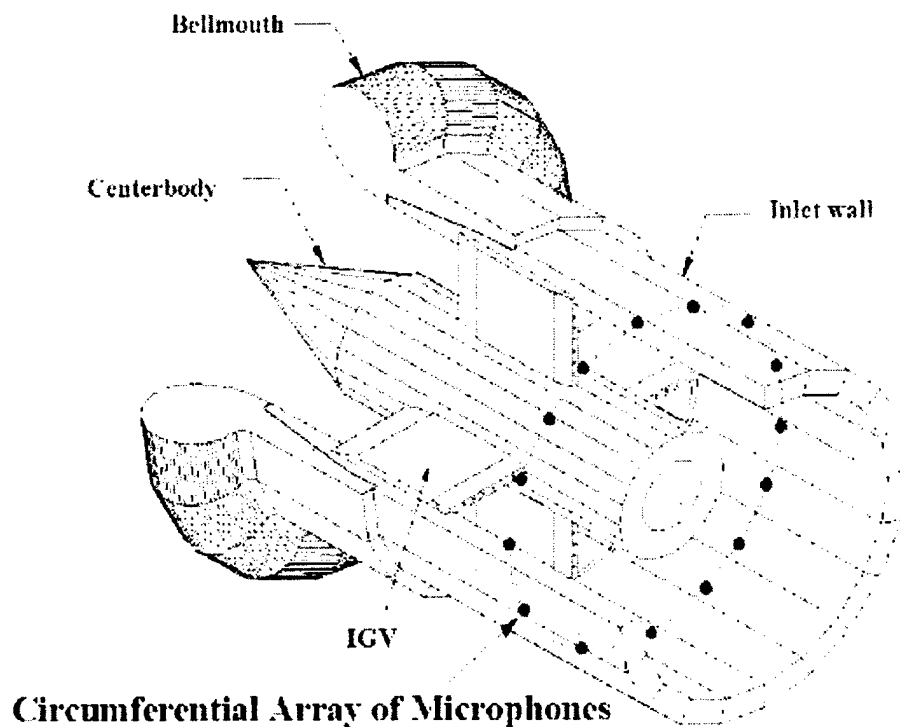
Figure 7.1: Mode magnitude and phase extraction using a circular microphone array.

the mode phase. Note that multiple circumferential modes can be extracted out by using different $\Delta\phi$ in Eqn. (7.1). Once the mode magnitude and phase of the significant acoustic modes are obtained, they can be carried over to Figure 5.19 to substitute the BPF tone magnitude and phase, respectively to implement the PID control algorithm.

In addition to the acoustic sensing approaches, other practical sensing techniques can be developed as well. These techniques may consist of mounting eddy current sensors

or light probes in the casing radially outside a blade row [67] to directly measure the blade vibrations. Eddy current sensors work in the principle of detecting magnetic flux changes caused by the spinning blades while light probes involve using a laser beam to detect blade vibration [68, 69]. Since the relatively small blade vibration is embedded in the large blade rigid-body motion as the rotor passes by the sensors, the most challenging part of the research may be the extraction of the rotor blade vibration information in the sensor output signal. In conjunction with these sensors, the appropriate TEB control algorithms should be also developed.

Other future work may include using a 3D aeroacoustic code to investigate TEB span-wise optimization to minimize the amount of blowing air. The use of the minimum amount of TEB air is very important since in real engines it needs to be bled from the compressor. Excessive use of bleeding air will impair the compressor efficiency. Minimization of TEB air may be obtained by blowing less air to the blade hub while more air to the blade tip since the blade tip exhibits relatively large vibrations. In addition, TEB control to re-energize the turning-IGV wakes should be also pursued since turning IGVs or stators are commonly used in real aircraft. The wake profile of the turning IGVs is not symmetrical and the axis of the wake profile may change with the inlet flow conditions.

Bibliography

[1] Air Force Office of Scientific Research. Basic research issues in aerodynamics, structural dynamics and control of high cycle fatigue. *Workshop Held at Gas Turbine Laboratory, MIT*, 1995.

[2] Workshop on Qualification of Life Extension Schemes for Engine Components. *Qualification of life extension schemes for engine components.* Neuilly-sur-Seine Cedex, France : North Atlantic Treaty, 1998.

[3] A. V. Srinivasan. Flutter and resonant vibration characteristics of the engine blades. *HCF Workshop, MIT*, 1995.

[4] K. R. V. Kaza and R. E. Kielb. Flutter of turbofan rotors with mistuned blades. *Journal of Electrochemical Society*, 22(11):1618 1625, 1984.

[5] Hsiao-Wei D. Chiang and Mark G. Turner. Compressor blade forced response due to downstream vane-strut potential interaction. *38th International Gas Turbine and Aeroengine Congress and Exposition, Cincinnati, Ohio, May 24-27*, 1993.

[6] Hsiao-Wei D. Chiang and Robert E. Kielb. An analysis system for blade forced response. *Proceedings of the 1998 International Gas Turbine & Aeroengine Congress and Exhibition. Stockholm, Sweden, May*, 1998.

[7] Robert T. Johnson and Sanford Fleeter. Inlet guide vane wakes, including rotor wakes. *40th International Gas Turbine and Aeroengine Congress and Exposition, Houston, Texas*, 1995.

[8] S. R. Manwarning and S. Fleeter. Rotor blade unsteady aerodynamic gust response to inlet guide vane wakes. *Journal of Turbomachinery*, 115:197–206, 1993.

[9] John M. Feiereisen Robert T. Johnson and Sanford Fleeter. Measured rotor wake and potential forcing functions, including blade row interactions. *Journal of Propulsion and Power*, 14(2):191-198, 1998.

[10] Robert Johnson and Sanford Fleeter. Three-dimensional time resolved measurements of igv-rotor potential interactions. *32nd AIAA/ASME/SAE/ASEE Joint Propulsion Conference, Lake Buena, Florida, AIAA-96-2670*, July 1996.

[11] Robert Johnson and Sanford Fleeter. Time resolved variations of an igv flow field in the presence of a rotor potential field. *34th AIAA/ASME/SAE/ASEE Joint Propulsion Conference & Exhibit, Cleveland, OHio, AIAA-98-3896*, July 1998.

[12] Donald W. Zabierek. Synopsis of passive damping active team activities. *3rd National Turbine Engine High Cycle Fatigue Conference*, Februrary 1998. San Antonio, Texas.

[13] Spiros Tatakis and Richard J. Stockton. Structural and aerodynamic influences to airfoil forced response. *38th International Gas Turbine and Aeroengine Congress and Exposition, Cincinnati, Ohio*, May 24-27, 1993.

[14] K. M. Spara and S. Fleeter. Aerodynamic detuning for control of supersonic rotor forced response. *Computational Mechanics*, 12:315-327, 1993.

[15] D. P. Probasco and J. M. Wolff. Axial spacing effects in a transonic compressor on the upstream vane loading. *34th AIAA/ASME/SAE/ASEE Joint Propulsion Conference, Cleveland, OHio, AIAA-98-3434*, July 1998.

[16] Albert J. Sanders and Sanford Fleeter. Vane row indexing for passive vibration control of axial-flow turbomachine rotors. *Journal of Propulsion and Power*, 15(5):650-657, 1999.

[17] Jeffrey D. Kozak. Investigation of inlet guide vane wakes in a f109 turbofan engine with and without flow control. *Ph.D. dissertation, Mechanical Engineering, Virginia Tech, VA*, 2000.

[18] C. J. Wood. The effect of base bleed on a periodic wake. *Journal of the Royal Aeronautical Society*, 68:477-482, 1964.

[19] J. Sell I. A. Waitz, J. M. Brookfield and B. J. Hayden. Preliminary assessment of wake management strategies for reduction of turbomachinery fan noise. *Journal of Propulsion and Power*, 12(5):958-966, 1996.

[20] R. G. Naumann. Control of the wake from a simulated blade by trailing edge blowing. *MS Thesis, Mechanical Engineering, Lehigh University, Bethlehem*, 1992.

[21] T. E. Corcoran. Control of the wake from a simulated blade by trailing edge blowing. *MS Thesis, Mechanical Engineering. Lehigh University, Bethlehem*, 1992.

[22] J. M. Cimbala and W. J. Park. An experimental investigation of the turbulent structure in a two-dimensional momentumless wake. *Journal of Fluid Mechanics*, 213:479–509, 1990.

[23] W. J. Park and J. M. Cimbala. The effect of jet geometry on two-dimensional momentumless wakes. *Journal of Fluid Mechanics*, 224:29–47, 1991.

[24] J. M. Brookfield and I. A. Waitz. Trailing-edge blowing for reduction of turbomachinery fan noise. *Journal of Propulsion and Power*, 16(1):57–64, 2000.

[25] T. Leitch. Reduction of unsteady stator-rotor interaction by trailing edge blowing. *MS Thesis, Mechanical Engineering, Virginia Tech, VA*, 1997.

[26] C. A. Sauders. Noise reduction in an axisymmetric supersonic inlet using trailing edge blowing. *MS Thesis, Mechanical Engineering, Virginia Tech, VA*, 1997.

[27] I. Day C. Freeman and M. Swinbanks. Experiments in active control of stall on an aeroengine gas turbine. *Journal of Turbomachinery-Transactions of the ASME*, 120(4):637–647, October, 1998.

[28] L. Harris and H. Spang. Compressor modeling and active control of stall/surge. *Proceedings of the 1991 American Control Conference. Boston, MA, USA*, 1991.

[29] R. R. Leitch and M. O. Tokhi. Active noise control systems. *Proc IEE*, 134:525–546, 1992.

[30] C. A. Sauders T. Leitch and W. F. Ng. Reductio of unsteady stator-rotor interaction using trailing edge blowing. *5th AIAA/CEAS Aeroacoustics Conference, Seattle, Washington, AIAA-99-1952*, May 1999.

[31] R. T. Howe and R. S. Muller. Polycrystalline silicon micromechanical beams. *Journal of Electrochemical Society*, 130:1420–1423, 1983.

[32] K. J. Gabriel R. T. Howe, R. S. Muller and W. S. N. Trimmer. *IEEE Spectrum*, pages 29–35, 1991.

[33] K. J. Gabriel. *Scientific American*, 260(9):118–121, 1995.

[34] C. M. Ho and L. S. Huang. Subharmonics and vortex merging in mixing layers. *Journal of Fluids Mechanics*, 119:443–473, 1982.

[35] C. M. Ho and P. Huerre. Perturbed free shear layers. *Ann. Rev. of Fluids Mechanics*, 16:365–424, 1984.

[36] James M. McMichael. Progress and prospects for active flow control using micro-fabricated electro-mechanical systems (mems). *34th Aerospace Sciences Meeting & Exhibit, Reno, NV, AIAA 96-0306*, January 1996.

[37] Chih-Ming Ho and Yu chong Tai. Review: Mems and its applications for flow control. *Journal of Fluids Engineering*, 118:437–447, 1996.

[38] Redwood Microsystems Inc. Operating principles-fluistor microvalve. *http://www.redwoodmicro.com/principles.html.*

[39] Redwood Microsystems Inc. Technical data/design specifications. 1997.

[40] N. M. Rao. Reduction of unsteady stator-rotor interaction by trailing edge blowing using mems based microvalves. *MS Thesis, Mechanical Engineering, Virginia Tech, VA*, 1999.

[41] R. Burdisso N. Rao, J. Feng and W. Ng. Active flow control reduce fan blade vibration and noise. *5th AIAA/CEAS Aeroacoustics Conference, Seattle, Washington, AIAA-99-1806*, May 1999.

[42] R. Burdisso N. Rao, J. Feng and W. Ng. Experimental demonstration of active trailing edge blowing control to reduce unsteady stator-rotor interaction. *Accepted by AIAA Journal.*

[43] Texas Instrument Incorporation. Tms320c3x user's guide. 1990.

[44] Toshiba Inc. Instruction manual, toshiba process loop controllers ec311 & ec321 (hardware and software). 1996.

[45] Peek Measurement Inc. User's manual, std 5000 & std 6000 i/p transducer. 1997.

[46] K. B. Washburn and G. C. Lauchle. Inlet flow conditions and tonal sound radiation from a subsonic fan. *Noise Control Engineering Journal*, 31(2):101–110, 1988.

[47] J. M. Tyler and T. G. Sofrin. Axial flow compressor noise studies. *J. Acoust. Soc. Am.*, 40(5):1248–1249, November 1966.

[48] Donald B. Hanson. Coupled 2-dimensional cascade theory for noise and unsteady aerodynamics of blade row interaction in turbofans. *NASA Contract Report No. 25952*, 1 and 2, 1994.

[49] P. M. Morse and K. U. Ingard. *Theoretical Acoustics*. Princeton University Press, 1968.

[50] A. B. Coppens L. E. Kinsler, A. R. Frey and J. V. Sanders. *Fundamentals of Acoustics*. New York: John Wiley & Sons, 1982.

[51] H. Levine and J. Schwinger. Radiation of sound from a circular pipe. *Physical Review*, 73:383–406, 1943.

[52] L. A. Weinstein. *The Theory of Diffraction and the Factorization Method*. Golem, 1969.

[53] G. F. Homicz and J. A. Lordi. A note on the radiative directivity patterns of duct acoustic modes. *Journal of Sound and Vibration*, 41:283–290, 1975.

[54] D. L. Lansing. Exact solution for radiation of sound from a semi-infinite circular duct with applicaition to fan and compressor noise, nasa sp-228. *Analytical Methods in Aircraft Aerodynamics*, pages 323–334, 1970.

[55] Donald F. Young Bruce R. Munson and Theodore H. Okiishi. *Fundamentals of Fluid Mechanics, 2nd Edition*. John Wiley & Sons, 1994.

[56] J. D. Powell G. F. Franklin and M. L. Workman. *Digital Control of Dynamic Systems*. Addison-Wesley, 1997.

[57] C. L. Phillips and R. D. Harbor. *Feedback Control Systems*. Prentice Hall, 1996.

[58] Joseph A. Schetz. *Injection a.id Mixing in Turbulent flow*. American Institute of Aeronautics and Astronautics, 1980.

[59] R. G. Staudte and S. J. Sheather. *Robust Estimation and Testing*. John Wiley, 1990.

[60] B. Widrow and S. D. Stearn. *Adaptive Signal Processing*. Englewood Cliffs, NJ: Prentice-Hall, 1985.

[61] C. R. Fuller R. A. Burdisso, R. H. Thomas and W. F. O'Brien. Active control of fan noise from a turbofan engine. *AIAA Journal*, 32(1):23–30, 1994.

[62] William F. Eagan. *phase-lock basics*. John Wiley & Sons, 1998.

[63] R. K. Majjigi and P. R. Gliebe. Development of a rotor wake/vortex model. *NASA Contract Report No. 174849*, 1:6–21, 1984.

[64] B. Lakshminarayana and R. Davino. Mean velocity and decay characteristics of the guidevane and stator blade wake of an axial flow compressor. *Journal of Engineering for Power*, 102:50 60, 1980.

[65] S. Katzoff A. Silverstein and W. K. Bullivant. Downwash and wake flow behind plain and flapped airfoils. *NCTA TP-651*, 1939.

[66] M. A. Theobald C. S. Ventres and W. D. Mark. Turbofan noise generation. *NASA Contract Report No. 167952*, 1, 1982.

[67] Ulrich Schaber. Non-contact vibration measurements of mistuned coupled blades. *42nd International Gas Turbine & Aeroengine Congress and Exposition. Orlando. FL, USA*, 1997.

[68] Henry Jones. Nonintrusive rotor blade vibration monitoring system. *41st International Gas Turbine & Aeroengine Congress and Exhibition. Burmingham, UK*, 1996.

[69] S. Heath. Improved single-parameter tip-timing method for turbomachinery blade vibration measurements using optical laser probes. *International Journal of Mechanical Sciences*, 38(10):1047–1058, October, 1996.

[70] Linear Technology Corporation. Datasheet for ltc1060. *http://www.linear-tech.com*.

[71] Michel A. SAAD. *Compressible Fluid Flow*. Prentice-Hall, Inc., 1985.

Appendix A

Adaptive BPF Tone Extractor

This appendix describes the two major components used in the adaptive BPF tone extractor in Chapter 5. In addition, some implementation issues of the extractor are discussed.

The proposed adaptive BPF tone extractor consists of two main electronic components which are switch-capacitor filter (SCF) and phase-locked loop (PLL) as shown in Figure 5.6. The SCF functions as a bandpass filter while the PLL provides adaptability in

the system. Besides functioning as a bandpass filter, an SCF can also be configured as a notch, low-pass or high-pass filter. They have been commercially available in the market in the recent years. The cost for each chip is around a couple of dollars which is much cheaper than a DSP which is required in the implementation of conventional adaptive filters. SCFs need no external capacitors or inductors, which allows consistent, repeatable filter designs. Furthermore, SCFs can have little sensitivity to temperature changes. This is because SCFs are clocked, sampled-data systems; the input is sampled at a high rate and is processed on a discrete-time, rather than continuous, basis. This is a fundamental difference between SCFs and conventional active and passive filters, which are also referred to as "continuous time" filters. The chips from Liner Technology Corporation implement the bandpass filters with the transfer functions in the s-domain as (take 2nd order as examples) [70]:

$$H_{bandpass} = H_{OBP}\frac{s\omega_n/Q}{s^2 + s(\omega_n/Q) + \omega_n^2} \tag{A.1}$$

$$\omega_n = \omega_c/M \tag{A.2}$$

where Q is the quality factor, H_{OBP} is the gain at the center frequency ω_n; ω_c is the clock frequency and M normally is equal to 100 or 20 which depends on the specific chips. It is noted from Equation A.1 that the phase shift is zero at the center frequency.

One the other hand, the PLL is used to increase the input signal frequency by M times

in this application to provide the clock signal for SCF. Phase locked loops are actually widely used in wireless communication. Basically, a PLL is a feedback system which synchronizes an oscillator in phase and frequency to an incoming signal. As can be seen in Figure A.1, a PLL has three main parts of a phase comparator, a low-pass filter and a voltage controlled oscillator (VCO). The phase comparator measures the phase difference between the input and output signals and produces an error signal proportional to the measured phase difference. If the low-pass filter is disregarded for the moment, the error signal will drive the VCO, changing its frequency so as to minimize the phase difference between the input and output signals. Ultimately, the frequency of the output signal will be identical to that of the input signal and will follow every change of the latter. Since the output signal is obtained by a frequency divider with a dividing factor of M, the frequency of the clock signal is M times of the input signal. To enable a PLL acquire lock in the first place, it should of course be designed so that the difference between the input and output frequencies is not so large that, after filtering, there is no control signal for the VCO.

The static performance of the extractor mainly depends on the SCF while the dynamic performance is primarily determined by the performance of PLL. The performance of SCFs varies from chips to chips. The most important parameter of our interests is the
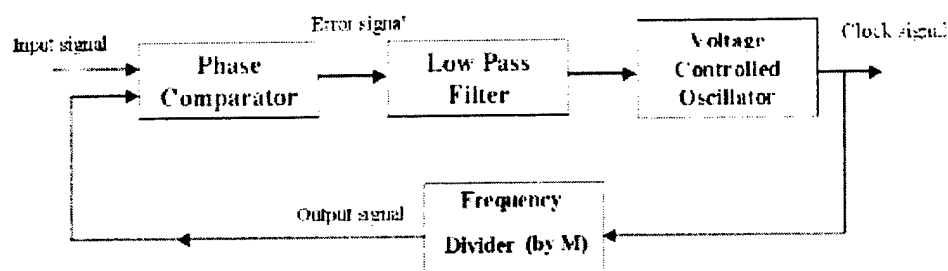
Figure A.1: The block diagram for a basic phase-locked loop.

maximum center frequency error, C_e, which is defined as:

$$C_e = \frac{f_0' - f_0}{f_0} \qquad (A.3)$$

where f_0' is the measured frequency in the output while f_0 is the ideal frequency of output signal. The SCF used here in the application is $LTC1264$ manufactured by Linear Technology Incorporatic. The center frequency error of this chip is 0.2%. This can be considered as a tiny error. The center frequency can be up to 250kHz. The performance of PLL is mainly governed by the loop components, i.e., the phase comparator, the loop filter, the voltage controlled oscillator used in the loop. Especially the loop filter plays the most important role among them. An active filter can be used as the loop filter to obtain a better loop performance. The PLL used here is 74HCT4046N from National Semiconductor Incorporation. It has three phase comparators which are exclusive-OR, edge-trigger JK flip-flop and edge trigger RS flip-flop. In addition, it has

a built-in VCO with an excellent frequency linearity.

The adaptive BPF power extractor is the key for the control system to success. As a matter of fact, there are several important implementation issues which need to be addressed here. The original rpm signal from the built-in magnetic pickup should be pre-conditioned before it can be used by the adaptive BPF extractor. There are several reasons for it. First, the original rpm signal is noise-contaminated. Especially, it is strongly disturbed by the line frequency, i.e., 50 Hz disturbance. Therefore, a high pass filter with the cut-on frequency of 100 Hz is used. Secondly, the amplitude of rpm signal is at a very low voltage level and varies with simulator speed as well. In the experiments, the rpm signal should be converted to a TTL (transistor to transistor logic) signal. Lastly, the rpm signal should be divided by six. Use of the undivided signal in frequency would lead the extractor to work only in several discrete narrow frequency ranges. This is because the six magnetic sensors are not mounted equally in space in the duct circumference. In consequence, the pulses in the rpm signal are not equally spaced in time leading to the broadband frequency content in the input signal. Experiments show that the pulses in the rpm signal is strictly equally spaced in time after the rpm signal is frequency-divided by six and then frequency-multiplied by six using PLL. Another issue is that enough gain should be provided to the microphone output signals before they are fed to SCFs. This helps to introduce less broadband

electronic noise to the circuits. As we does to a traditional ADC, the input signal range should be amplified or attenuated so that it matches the ADC range in order to make full use of the ADC resolution. The same rule applies to an SCF because an SCF, like an ADC, also works on the discrete signals.

Lastly, it is also worth to mention that the adaptive BPF tone extractor can find applications in the areas of active noise and vibration control, condition monitoring and fault detection system for rotatory machinery, and communication system, etc.

Appendix B

Phase-Voltage Converters

This appendix describes the working principles of the phase-voltage converter (PVC) used in Chapter 5. The block diagram of the PVC implementation is presented and the use of the kernel component of XOR is also introduced.

Phase-voltage converter (PVC) is an important component in the microphone-based TEB control system. The phase signal of BPF tone needs to be converted to a voltage signal so that it can be used by the digital signal processor. The basic requirement for

this conversion is that the controller should be able to determine whether it is under or over blowing by detecting the voltage signal.

Without loss of generality, negative voltages are specified to represent underblowing while positive voltages to represent overblowing. Therefore, in Table 5.1, 90° through 180° in microphone # 1 and # 3 should be converted to negative voltages since 90° through 180° are known for underblowing. Similarly, 0° through 90° in microphone # 1 and # 3 should be converted to positive voltages because they occur in overblowing case. On the other hand, 0° through 90° of microphone # 2 and # 4 should be converted to negative voltages while 90° through 180° of microphone #2 and # 4 should be converted to positive voltages for the same reason: 90° in all microphones should be converted to zero voltage. To avoid the ambiguity, in the real implementations the signals from microphone # 1 and # 3 are inverted (i.e., a phase change of π) so that the phase range of $180^o - 0^o$ is changed to $0^o - -180^o$. In consequence, 0° through $\pm90^o$ in all the microphones should be converted to negative voltages while 90° through 180° or -90° through -180° are to positive voltages.

The phase-voltage converter with the characteristics shown in Figure 5.20 can meet the above requirements. The implementation block diagram is shown in Figure B.1. It is important to remark that this application requires the PVC to be insensitive to the

amplitude of the input signal since the BPF tone fluctuates severely in the testing. As it can be seen. the BPF tone extracted from a casing microphone and the rpm signal are converted to the TTL signal (i.e., high-level of 5 volts and a low-level of 0 volts) before they are input to the exclusive-OR gate. The frequency multiplier is needed because the frequency of rpm signal from the magnetic pickup is only one third the blade passing frequency. The phase shifter is needed to set the relative phase to 0° at noblowing.

The exclusive OR gate is the kernel component in the PVC. Figure B.2 depicts the truth table that defines the gate operation. The output goes high when only one input goes high. and the gate output remains at a logic low for all other inputs. Also, note that the figure depicts v_i and v_o as having the same frequency. Thus, the mean value $\hat{v}_d$, obtained using a low pass filter (LPF) following XOR, displays a triangular function of the phase difference $\Delta\phi$. Finally, the exact plot shown in Figure 5.20 can be obtained if the LPF output is offset by a DC voltage.
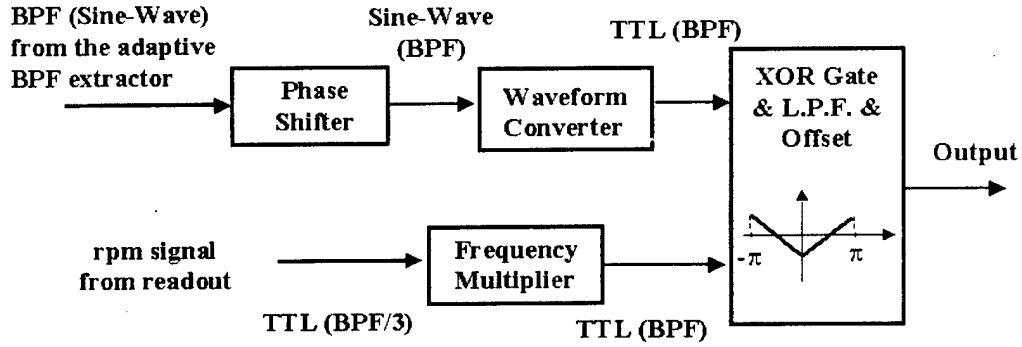
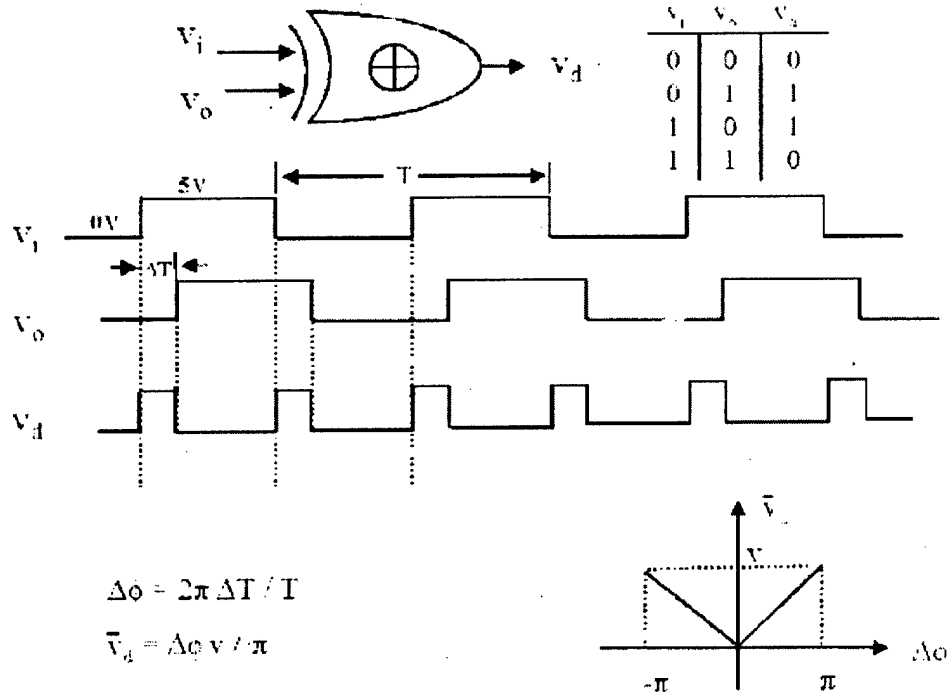Figure B.1: The block diagram for the PVC implementation.

$$\Delta\phi = 2\pi\,\Delta T\,/\,T$$

$$\bar{V}_d = \Delta\phi\,v\,/\,\pi$$

Figure B.2: The operation of the exclusive OR gate.

Appendix C

Introduction of TEB into CUP2D

Code

This appendix first describes the basic idea of introducing TEB into the CUP2D code. The FFT coefficients of the TEB model is then derived which are used in Chapter 6.

The basic idea behind the formulation of the aeroacoustic CUP2D code is to obtain the stator and rotor loadings first, then to compute the sound field according to them.

A summary of the theory is as follows. The stator loading, LS, and rotor loading, LR, are obtained by solving Eqn. (C.1). It should be pointed out that each variable in Eqn. (C.1) denotes a matrix. WR and WS mean the wash velocity on the rotor and stator. KRR (KSR, etc.) matrix is called influence coefficient matrix which relate upwash velocities at the stator and rotor control points as functions of the unknown loading on the rotor and stator panels. KRR denotes the effect of rotor on rotor, while KSR means the effect of stator on rotor, and so on.

$$\begin{bmatrix} KRR & KSR \\ KRS & KSS \end{bmatrix} \begin{bmatrix} LR \\ LS \end{bmatrix} = \begin{bmatrix} WR \\ WS \end{bmatrix} \tag{C.1}$$

In addition, two boundary conditions should be satisfied when solving Eqn.(C.1). The flow tangency requirement on the first row, say if it is stator, is shown in Eqn. (C.2).

$$WS(n,i) = WSS(n,i) + WRS(n,i) = 0 \quad \text{for all n, i} \tag{C.2}$$

where loading harmonics are counted by n and control points are counted by i. Eqn. (C.2) states that the sum of the upwash at the stator due to the stator and rotor, denoted by $WSS(n,i)$ and $WRS(n,i)$, respectively, is zero for all harmonics and at all control points. For the second row in the 2D model, say if it is rotor, the condition is different since it is excited by the viscous wake of the upstream stators, as indicated in Figure 6.6. If we call the wake upwash harmonics $WWS(n,i)$, then the rotor boundary

condition is:

$$WR(n,i) \;=\; WRR(n,i) + WSR(n,i) \;=\; -WWS(n,j) \quad \text{for all n, i} \quad (C.3)$$

It indicates that the net effect of the waves from the rotor, $WRR(n,i)$ and the waves

from the stator, $WSR(n,i)$ must be equal and opposite to the wake upwash for flow

tangency.

The active TEB model should be transformed into frequency domain using Fourier

integral as required by CUP2D. The analytical derivation to compute the Fourier co-

efficients conducted here is similar to the work by Hanson [48]. The pure wake profile

of upstream row is rewritten here according to Eqn. (6.1):

$$W(y, s_1) = W_{dc}(s_1) \cdot f(y, s_1) \tag{C.4}$$

where the streamwise and pitchwise coordinates s_1 and y are shown in Figure 6.6;

$f(y, s_1)$ is:

$$f(y, s_1) = e^{-0.693\left[\frac{y}{\delta(s_1)}\right]^2} \tag{C.5}$$

In Eqn. (C.4) and (C.5), $W_{dc}(s_1)$ and $\delta(s_1)$ are governed by the Lakshminarayana-

Davino model which is represented by Eqn. (6.6) and Eqn. (6.7). Reference [48] shows

that y can be expressed as:

$$y = y_2 cos\theta_1 - cos\theta_2 \cdot (\Omega_1 - \Omega_2)Rt - xsin\theta_1 \tag{C.6}$$

where t denotes time. With the use of Eqn. (C.6) and relations of $x = x_s + s_2 cos\theta_2$ and $y_2 = s_2 sin\theta_2$, Eqn. (C.5) can be expressed in terms of t as:

$$f(t, s_1) = \exp\left(-0.693\left[\frac{sin(\theta_2 - \theta_1)s_2 - x_s sin\theta_1 - cos\theta_1(\Omega_1 - \Omega_2)Rt}{\delta(s_1)}\right]^2\right) \quad (C.7)$$

Since it is recognized that this one pulse repeats itself at the blade passing period of $T = 2\pi/B_1(\Omega_1 - \Omega_2)$, we can express $f(t, s_1)$ in a Fourier series of the following form:

$$f(t, s_1) = \sum_{n=-\infty}^{\infty} F_n(s_1) \cdot e^{inB_1(\Omega_1 - \Omega_2)t} \quad (C.8)$$

The usual Fourier series formula leads to:

$$F_n(s_1) = \frac{2\sqrt{\pi}}{Q} \cdot \frac{W_{dc}(s_1)}{W_1} \exp\left[-(\frac{\pi n}{Q})^2\right] \exp\left(\frac{inB_1[-s_2 sin(\theta_1 - \theta_2) + x_s sin\theta_1]}{cos\theta_1}\right) \quad (C.9)$$

where,

$$Q = \frac{\sqrt{\pi}G_1 cos\theta_1}{2.13\delta(s_1)} \quad (C.10)$$

Similarly, the Fourier coefficients associated with the TEB jet can be obtained:

$$F_n^T(s_1) = \frac{2\sqrt{\pi}}{Q^T} \cdot \frac{W_{dc}^T(s_1)}{W_1} \cdot \exp\left[-(\frac{\pi n}{Q^T})^2\right] \exp\left(\frac{inB_1[-s_2 sin(\theta_1 - \theta_2) + x_s sin\theta_1]}{cos\theta_1}\right) \quad (C.11)$$

where,

$$Q^T = \frac{\sqrt{\pi}G_1 cos\theta_1}{2.13a_0\delta(s_1)} \quad (C.12)$$

$$W_{dc}^T(s_1) = b_0 \cdot W_{dc}(s_1) \quad (C.13)$$

Now, only the components of the wake and TEB jet normal to the stator chord are required. This is given by multiplying $sin(\theta_1 - \theta_2)$. Hence, the desired upwash harmonics to be used in the code can now be written as:

$$\left[\frac{W_{normal}}{W_2}\right]_n = \frac{W_{dc}(s_1)}{W_1}\frac{cos\theta_2}{cos\theta_1}sin(\theta_2 - \theta_1)(F_n(s_1) + F_n^T(s_1)) \cdot e^{inB_1(\Omega_1 - \Omega_2)t} \qquad (C.14)$$

where for convenience, the relation of $W_1/W_2 = cos\theta_2/cos\theta_1$ is used; W_{normal} is the component of the mixed flow normal to the stator chord. The role of TEB is reflected by $F_n^T(s_1)$; $F_n(s_1)$ is associated with the pure wake as shown in Eqn. (C.9) while F_n^T can be obtained from Eqn. (C.11). This equation should be input into the subroutine GETWAKE to compute $WWS(n, i)$ as needed for inversion of the matrix equation of (C.1).

Appendix D

Flow Condition Estimation for

Simulator Running at 30,000 rpm

This appendix derives the flow condition parameters for the simulator running at 30,000 rpm. These parameters including the axial flow velocity, sound speed and fluid density upstream IGV, in-between IGV and rotor and downstream rotor are required to input the CUP2D code to conduct analytical studies in Chapter 6.
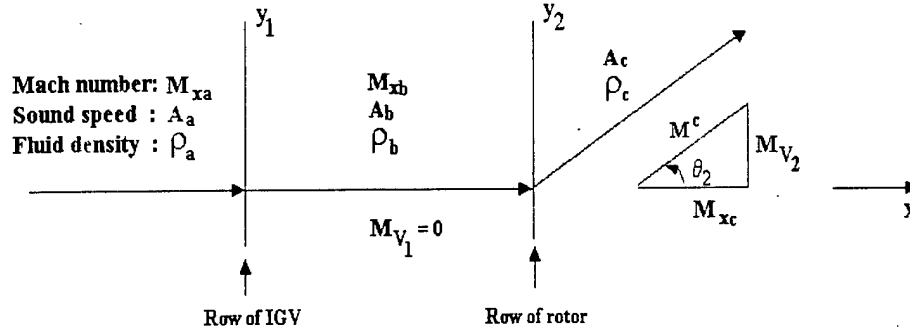
Figure D.1: Re-depict of the 2D cascade model of the simulator.

The 2D cascade model is re-depicted here as shown in Figure D.1 for convenience. Three regions in the model are defined which are upstream IGV (denoted by "a"), in-between IGV ("b") and downstream rotor ("c"). The axial flow mach number, sound speed and fluid density in region "a" are denoted as M_{xa}, A_a and ρ_a, respectively. Similarly, M_{xb}, A_b, ρ_b and M_{xc}, A_c, ρ_c represent those in region "b" and "c", respectively; M^c is the Mach number of absolute flow velocity in region "c". Since the non-turning IGVs are used in the first row, the flow conditions in the region "a" are identical to those in region "b" except that IGV wakes are present in region "b". The one-stage simulator is estimated to provide a pressure ratio of 1.5 with an efficiency of 80%; M_{xa} and M_{xc} are assumed to be 0.3 and 0.6, respectively. The stagger of rotor blades is assumed to be 45°. The ambient temperature is 300 Kelvin.

Since M_{xa} is known, the ratio of the static pressure P^a to the total pressure P_0^a and the ratio of the static temperature T^a to the total temperature T_0^a can be found in the well-established fluid property look-up table [71]:

$$\frac{P^a}{P_0^a} = 0.94 \tag{D.1}$$

$$\frac{T^a}{T_0^a} = 0.98 \tag{D.2}$$

where P_0^a is equal to the ambient pressure which is $101,000\ Pa$ and T_0^a is $300\ K$. It follows that $P^a = 94,940$ Pa according to Eqn. (D.1) and $T^a = 294$ K according to Eqn. (D.2). Using these results, the fluid density ρ_a can be obtained according to the ideal gas law:

$$\rho_a = \frac{P^a}{RT^a} \tag{D.3}$$

$$= 1.125\ kg/m^3 \tag{D.4}$$

where R is the gas constant which has the value of $287\ N \cdot m/kg \cdot K$. Similarly, the sound speed A_a can be found [71]:

$$A_a = \sqrt{\gamma RT^a} \tag{D.5}$$

$$= 343.7\ m/s \tag{D.6}$$

where γ is the specific heat capacity ratio, i.e., 1.4. Up to here, the flow conditions in region "a" and "b" have been obtained since both regions share the same flow parameters. They are

$$M_{xa} = M_{xb} = 0.3$$

$$A_a = A_b = 343.7 \ m/s$$

$$\rho_a = \rho_b = 1.125 \ kg/m^3$$

Since the pressure ratio, P_0^c/P_0^b, produced by the rotor is 1.5, the ideal total temperature in the region "c", $T_0^{c,i}$ can be obtained, if the process is isentropic and no efficiency is lost, by solving [71]

$$\left(\frac{P_0^c}{P_0^b}\right)^{\frac{\gamma-1}{\gamma}} = \frac{T_0^{c,i}}{T_0^b} \tag{D.7}$$

$T_0^{c,i}$ is computed to be 336.8 K. Since the efficiency is estimated to be 80%, the actual total temperature T_0^c should be calculated according to the following relation

$$(T_0^{c,i} - T_0^b) = (T_0^c - T_0^b) \cdot 80\% \tag{D.8}$$

It follows that $T_0^c = 346$ K. To get the static temperature T^c, the absolute flow velocity M^c should be obtained first. Since the rotor blade stagger θ_2 is assumed to be 45° and M_{xc} is assumed to be 0.6. M^c is calculated to be 0.84 according to the velocity triangle in Figure D.1. With the value of M^c, the following relations can be found again in the look-up table

$$\frac{P^c}{P_0^c} = 0.62 \tag{D.9}$$

$$\frac{T^c}{T_0^c} = 0.87 \tag{D.10}$$

where the total pressure P_0^c has a value of 152,000 Pa since the pressure ratio is 1.5:

the total temperature T_0^c is 346 K as found from Eqn. (D.7). It follows that P^c is then

computed to be 93,600 Pa according to Eqn. (D.9) and T^c is 301 K according to Eqn.

(D.10). The fluid density ρ_c is calculated by using the ideal gas law once again:

$$\rho_c = \frac{P^c}{RT^c} \tag{D.11}$$

$$= 1.08 \ kg/m^3 \tag{D.12}$$

Similarly, the sound speed A_c can be found:

$$A_c = \sqrt{\gamma RT^c} \tag{D.13}$$

$$= 347.8 \ m/s \tag{D.14}$$

Therefore, the flow conditions in region "c" have been obtained:

$$M_{xc} = 0.6$$

$$A_c = 347.8 \ m/s$$

$$\rho_c = 1.08 \ kg/m^3$$

As a final note, the drag coefficient of the IGV, C_D is selected as 0.01 in CUP2D code.

This value is obtained by using Figure 9.24, Page 600 of the reference [55] since the

Reynolds number calculated for the case is around $7.0 \cdot 10^5$.